


รายงานวิจัยฉบับสมบูรณ์

โครงการ การสังเคราะห์คอปเปอร์ออกไซด์-ซิงค์ออกไซด์-เซอร์โคเนียมไดออกไซด์ด้วยกระบวนการโซล-เจล สำหรับเร่งปฏิกิริยาในการเติมไฮโดรเจนของคาร์บอนไดออกไซด์เพื่อผลิตเมทานอล

โดย ผศ.ดร.ธงไทย วิฑูรย์

มิถุนายน 2556

สัญญาเลขที่ MRG5480196

รายงานวิจัยฉบับสมบูรณ์

โครงการ การสังเคราะห์คอปเปอร์ออกไซด์-ซิงค์ออกไซด์-เซอร์โคเนียมไดออกไซด์ด้วยกระบวนการโซล-เจล สำหรับเร่งปฏิกิริยาในการเติมไฮโดรเจนของคาร์บอนไดออกไซด์เพื่อผลิตเมทานอล

ผศ.ดร.ธงไทย วิฑูรย์
ภาควิชาวิศวกรรมเคมี คณะวิศวกรรมศาสตร์
มหาวิทยาลัยเกษตรศาสตร์

สนับสนุนโดยสำนักงานกองทุนสนับสนุนการวิจัย

บทคัดย่อ

ในงานวิจัยนี้แบ่งเป็น 2 หัวข้อหลักคือ 1) การสังเคราะห์เมทานอลจากปฏิกิริยาการเติมก๊าซไฮโดรเจนของก๊าซคาร์บอนไดออกไซด์โดยใช้คอปเปอร์ออกไซด์-ซิงค์ออกไซด์นาโนคอมโพซิท 2) การศึกษาผลของซิลิกาที่มีรูพรุนสองขนาดต่ออนุภาคและการรีดิวซ์ของโคบอลต์ออกไซด์

ในหัวข้อที่ 1 คอปเปอร์ออกไซด์-ซิงค์ออกไซด์นาโนคอมโพซิทจะถูกเตรียมด้วยวิธีการตกตะกอนร่วม หลังจากนั้นนำนาโนคอมโพซิทที่เตรียมได้ไปใช้เป็นตัวเร่งปฏิกิริยาในปฏิกิริยาการเติมก๊าซคาร์บอนไดออกไซด์ด้วยไฮโดรเจนเพื่อผลิตเมทานอล ผลของความเข้มข้นไคโตซานบนคุณลักษณะทางกายภาพและทางเคมีของนาโนคอมโพซิทและบนความว่องไวในการเกิดปฏิกิริยาถูกตรวจสอบอย่างละเอียด ตัวเร่งปฏิกิริยาที่ได้รับถูกวิเคราะห์ด้วยความเสถียรทางความร้อน การถ่ายภาพด้วยกล้องจุลทรรศน์อิเล็กตรอนแบบส่องกราด การวิเคราะห์องค์ประกอบและขนาดผลึก การวิเคราะห์การดูดซับการคายซับก๊าซไนโตรเจน การวิเคราะห์การดูดซับทางเคมี และการวิเคราะห์ความสามารถในการรีดิวซ์ ผลการทดลองแสดงให้เห็นว่าไคโตซานไม่เพียงแต่จะทำหน้าที่เป็นตัวช่วยตกตะกอนร่วมระหว่างคอปเปอร์ออกไซด์-ซิงค์ออกไซด์แต่ยังทำหน้าที่เป็นสารแม่แบบสำหรับการเกิดนาโนคอมโพซิททรงกลมกลวง ขนาดผลึกของคอปเปอร์ออกไซด์และซิงค์ออกไซด์ของนาโนคอมโพซิททรงกลมกลวง มีค่าเป็น 11.5 และ 18.8 นาโนเมตรตามลำดับ อย่างไรก็ตามการเพิ่มความเข้มข้นของไคโตซานทำให้พื้นที่ผิวรวมและพื้นที่ผิวของคอปเปอร์ลดลง ตัวเร่งปฏิกิริยาที่เตรียมโดยใช้ไคโตซานเป็นสารช่วยตกตะกอนร่วมให้อัตราการเกิดเมทานอลสูงกว่าตัวเร่งปฏิกิริยาที่ไม่ใช้สารตกตะกอน อย่างไรก็ตามเมื่ออุณหภูมิในการเกิดปฏิกิริยาสูงถึง 533 เคลวิน พบว่าอัตราการเกิดเมทานอลลดลงสำหรับตัวเร่งปฏิกิริยาที่เตรียมโดยใช้ปริมาณไคโตซานสูง

ในหัวข้อที่ 2 ผลของซิลิกาที่มีรุพรุนสองขนาดต่ออนุภาคและการรีดิวซ์ของโคบอลต์ออกไซด์จะถูกตรวจสอบ โดยซิลิกาที่มีรูพรุนหนึ่งขนาดจะถูกใช้เพื่อเป็นตัวเปรียบเทียบ โดยซิลิกาทั้งสองชนิดจะนำมาจุ่มชุบแบบแห้งด้วยสารละลายโคบอลต์ไนเตรต 10 เปอร์เซ็นต์ หลังจากนั้นนำไปวิเคราะห์ โครงสร้างรูพรุน พื้นที่ผิว ขนาดผลึกของโคบอลต์ออกไซด์ที่เตรียมได้ และศึกษาพฤติกรรมการรีดิวซ์ด้วยก๊าซไฮโดรเจน ผลการทดลองพบว่าขนาดผลึกเฉลี่ยของโคบอลต์ออกไซด์ที่เตรียมได้บนซิลิกาที่มีรูพรุนสองขนาดมีขนาดใหญ่กว่าขนาดผลึกเฉลี่ยของโคบอลต์ออกไซด์บนซิลิกาที่มีรูพรุนหนึ่งขนาดเล็กน้อย ซึ่งเป็นเนื่องจากโคบอลต์ออกไซด์กระจายตัวอยู่บนเมโซพอร์และมาโครพอร์ ในขณะที่โคบอลต์ออกไซด์ที่โหลดบนซิลิกาที่มีรูพรุนสองขนาดถูกรีดิวซ์เป็นโลหะโคบอลต์ได้ง่ายกว่าการใช้ซิลิกาที่มีรูพรุนเพียงแค่หนึ่งขนาดเป็นตัวรองรับ ทั้งนี้เนื่องจากรุพรุนขนาดมาโครพอร์สามารถช่วยในการแพร่ของทั้งก๊าซไฮโดรเจนและไอน้ำซึ่งเป็นผลิตภัณฑ์ ตัวรองรับซิลิกาที่มีรูพรุนสองขนาดถูกคาดหวังว่าจะช่วยเพิ่มประสิทธิภาพการเร่งปฏิกิริยาในปฏิกิริยาที่มีขั้นตอนการแพร่เป็นขั้นกำหนดอัตรา

Abstract

The present study focuses on two topics: 1) synthesis of methanol from CO_2 hydrogenation using CuO-ZnO nanocatalysts 2) investigation of effect of bimodal porous silica on particle sizes and reducibility of cobalt oxide.

In the first topic, CuO–ZnO nanocomposites were prepared by chitosan-assisted co-precipitation method and performed as catalyst for CO_2 hydrogenation to methanol. Effects of chitosan concentration on the physicochemical properties of the nanocomposites as well as the catalytic activity have been investigated. The obtained catalysts were characterized by means of thermal gravimetric-temperature difference analysis, scanning electron microscopy, X-ray diffraction, N_2 adsorption–desorption, N_2O chemisorption and temperature-programmed reduction. Chitosan was found to act not only as a coordination compound to produce a homogeneous combination of CuO–ZnO nanocomposite, but also as a soft template for the formation of hollow nanospheres. The CuO and ZnO crystallite sizes of the hollow nanospheres were found to be 11.5 and 18.8 nm, respectively, which were smaller than those of other catalysts. The increase of chitosan concentration caused a change in catalyst morphology and a reduction in BET surface area as well as metallic copper surface area, but still higher than those of the unmodified catalyst. The catalysts prepared by using chitosan as precipitating agent exhibited a higher space time yield of methanol than the unmodified catalyst, which was attributed to a synergetic effect of the CuO nanoparticle incorporated in the CuO–ZnO nanocatalyst. However, when the reaction temperature was increased up to 533 K, a decline in the space time yield of methanol was observed for the catalysts prepared at high chitosan concentration.

In the second topic, the effect of bimodal porous silica (BPS) on particle size and reducibility of cobalt oxide has been investigated. Unimodal porous silica (UPS) was used for comparison purposes. Both silica supports were impregnated with an aqueous solution of cobalt nitrate to obtain cobalt loadings of about 10 wt%. Specific surface area, morphology and cobalt oxide crystallite size of the cobalt oxide loaded on porous silicas were systematically characterized by means of N_2 sorption, X-ray diffraction, scanning electron microscopy and transmission electron microscopy. The reduction behavior profiles and the activation energy for the reducibility of the cobalt oxide were studied by dynamic thermal gravimetric under flow of H_2. The average particle size of cobalt oxide loaded on the BPS sample was revealed to be slightly larger than that loaded on the UPS sample, likely because cobalt oxide particles were distributed both on mesopores and macropores. The reduction temperatures of the cobalt oxide loaded on the BPS sample were found to be evidentially lower than those of the cobalt oxide loaded on the UPS sample.

Project Code : MRG5480196

Project Title : การสังเคราะห์คอปเปอร์ออกไซด์-ซิงค์ออกไซด์-เซอร์โคเนียมไดออกไซด์ ด้วยกระบวนการโซล-เจล สำหรับเร่งปฏิกิริยาในการเติมไฮโดรเจนของคาร์บอนไดออกไซด์เพื่อผลิตเมทานอล

Investigator : ผศ.ดร.ธงไทย วิฑูรย์

E-mail Address : fengttwi@ku.ac.th

Project Period : 2 ปี

หัวข้อที่ 1 การสังเคราะห์เมทานอลจากปฏิกิริยาการเติมก๊าซไฮโดรเจนของก๊าซคาร์บอนไดออกไซด์โดยใช้คอปเปอร์ออกไซด์-ซิงค์ออกไซด์นาโนคอมโพซิท

1. วัตถุประสงค์การทดลอง

1) เพื่อศึกษาการใช้ไคโตซานเป็นสารช่วยตกตะกอนร่วมในการเตรียมตัวเร่งปฏิกิริยา คอปเปอร์ออกไซด์-ซิงค์ออกไซด์
2) เพื่อศึกษาความว่องไวในการเกิดปฏิกิริยาการเติมก๊าซไฮโดรเจนของก๊าซคาร์บอนไดออกไซด์เพื่อผลิตเมทานอลที่อุณหภูมิในการเกิดปฏิกิริยาต่าง ๆ
3) เพื่อศึกษาเสถียรภาพในการเร่งปฏิกิริยาการเติมก๊าซไฮโดรเจนของก๊าซคาร์บอนไดออกไซด์เพื่อผลิตเมทานอล

2. วิธีการทดลอง

2.1 การเตรียมคอปเปอร์ออกไซด์-ซิงค์ออกไซด์ นาโนคอมโพสิท

สารเคมีที่ใช้ประกอบไปด้วย

- $Cu(NO_3)_2 \cdot 3H_2O$ จากบริษัท Sigma-aldrich
- $Zn(NO_3)_2 \cdot 6H_2O$ จากบริษัท Sigma-aldrich
- กรดอะซิติก
- แอมโมเนียมไฮดรอกไซด์
- ไคโตซาน 80% deacetylation และมี M_w = 290,000 Da

ในขั้นตอนแรกนำไคโตซานมาละลายใน 100 มิลลิลิตรของ 1% กรดอะซิติกในน้ำกลั่น หลังจากนั้น ทำการกวนไคโตซานทิ้งไว้ 1 คืน เติม 3.749 กรัม $Cu(NO_3)_2 \cdot 3H_2O$ และ 4.616 กรัม $Zn(NO_3)_2 \cdot 6H_2O$ (อัตราส่วนโดยโมลของคอปเปอร์ต่อซิงค์เป็น 1:1) ลงในสารละลายไคโตซาน หลังจากนั้นทำการปรับค่าพีเอชเท่ากับ 6 โดยใช้สารละลายแอมโมเนียมไฮดรอกไซด์ ทำการกวนที่อุณภูมิ 60 องศาเซลเซียส เป็นเวลา 6 ชั่วโมง เพื่อให้แน่ใจว่าไคโตซานสามารถทำหน้าที่เป็นสารตกตะกอนร่วมได้อย่างสมบูรณ์ หลังจากนั้นปรับอุณหภูมิของของผสมไปที่ 80 องศาเซลเซียส เพื่อระเหยสารละลายออก สารตกตะกอนที่ได้จะนำมาอบให้แห้งที่อุณหภูมิ 120 องศาเซลเซียส เป็นเวลา 24 ชั่วโมง ผลิตภัณฑ์ที่ได้จะถูกนำมาเผาภายใต้สภาวะอากาศที่อุณหภูมิ 450 องศาเซลเซียส เป็นเวลา 2 ชั่วโมง โดยใช้อัตราการให้ความร้อน 2 องศาเซลเซียสต่อนาที เพื่อที่จะตรวจสอบผลกระทบของค่าพีเอชและความเข้มข้นของไคโตซาน การทดลองดังกล่าวข้างต้นได้ทำซ้ำแต่มีการปรับค่าพีเอชเป็น 7 และ 8 ในขณะที่ ปริมาณไคโตซานมีการปรับเปลี่ยนเป็น 0, 0.0030 และ 0.006 มิลลิกรัมต่อลิตร ผลิตภัณฑ์ที่สังเคราะห์ได้จะให้ชื่อว่า CZ- *x* ที่ซึ่ง *x* คือความเข้มข้นของไคโตซาน

2.2 การวิเคราะห์คุณลักษณะของคอปเปอร์ออกไซด์-ซิงค์ออกไซด์ นาโนคอมโพสิท

2.2.1 การถ่ายภาพด้วยกล้องจุลทรรศน์อิเล็กตรอนแบบส่องกราด

พื้นผิวและองค์ประกอบของผลิตภัณฑ์ที่สังเคราะห์ได้จะถูกตรวจสอบด้วยเทคนิคการถ่ายภาพด้วยกล้องจุลทรรศน์อิเล็กตรอนแบบส่องกราด (FE-SEM: Hitachi-S4700) ต่อกับเครื่องวิเคราะห์องค์ประกอบธาตุ โดยตัวอย่างจะมีการเคลือบทองก่อนการวิเคราะห์

2.2.2 การวิเคราะห์เฟสและขนาดผลึกของคอปเปอร์ออกไซด์และซิงค์ออกไซด์

X-ray diffractometer ถูกใช้สำหรับวิเคราะห์เฟสและขนาดผลึกของคอปเปอร์ออกไซด์และซิงค์ออกไซด์ บน Bruker D8 Advance โดยการวิเคราะห์ทำที่อุณหภูมิห้องในช่วง 20° ถึง 80° โดยขนาดผลึกสามารถคำนวนได้จากสมการของ Scherrer ดังแสดงในสมการที่ 1

$$d = \frac{0.89\lambda}{B\cos\theta} \times \frac{180^{o}}{\pi} \qquad (1)$$

โดยที่ d คือ ขนาดผลึกเฉลี่ย λ คือ ความยาวคลื่น ของรังสีเอ็กซ์ (1.54 อังสตรอม) และ B คือความกว้างของครึ่งหนึ่งของพีคที่สูงที่สุด

2.2.3 การวิเคราะห์ความเสถียรทางความร้อน

Thermal gravimetric และ temperature difference analysis ถูกใช้ในการวิเคราะห์อุณหภูมิในการสลายตัวของพอลิเมอร์และการเปลี่ยนรูปให้เป็นออกไซด์ของคอปเปอร์และซิงค์ไนเตรต โดยใช้ตัวอย่าง 20 มิลลิกรัมใส่ในถ้วยอะลูมินาและให้ความร้อนที่อัตราการให้ความร้อน 10 องศาเซลเซียสต่อนาที ภายใต้อัตราการไหลของก๊าซไนโตรเจนที่ 80 มิลลิลิตรต่อนาที

2.2.4 การวิเคราะห์พื้นที่ผิว ขนาดรูพรุนและปริมาตรรูพรุน

N_2-sorption ถูกใช้ในการวิเคราะห์หาพื้นที่ผิว การกระจายตัวของรูพรุนและปริมาตรรูพรุนของตัวเร่งปฏิกิริยาที่เตรียมได้ โดยก่อนการวิเคราะห์ตัวอย่างจะต้องทำการไล่ความชื้นออกก่อนโดยให้ความร้อนที่ 200 องศาสเซลเซียส เป็นเวลา 12 ชั่วโมง โดยการกระจายตัวของรูพรุนคำนวนด้วยวิธี Barrett–Joyner–Halenda (BJH) ปริมาตรรูพรุนรวมคำนวนที่ตำแหน่ง P/P_0 = 0.995 พื้นที่ผิวรวมคิดด้วยวิธี BET (Brunauer–Emmert–Teller) ในช่วง P/P_0 = 0.05 ถึง 0.30

2.2.5 การวิเคราะห์พื้นที่ผิว ขนาดรูพรุนและปริมาตรรูพรุน

N_2-sorption ถูกใช้ในการวิเคราะห์หาพื้นที่ผิว การกระจายตัวของรูพรุนและปริมาตรรูพรุนของตัวเร่งปฏิกิริยาที่เตรียมได้ โดยก่อนการวิเคราะห์ตัวอย่างจะต้องทำการไล่ความชื้นออกก่อนโดยให้ความร้อนที่ 200 องศาสเซลเซียส เป็นเวลา 12 ชั่วโมง โดยการกระจายตัวของรูพรุนคำนวนด้วยวิธี Barrett–Joyner–Halenda (BJH) ปริมาตรรูพรุนรวมคำนวนที่ตำแหน่ง P/P_0 = 0.995 พื้นที่ผิวรวมคิดด้วยวิธี BET (Brunauer–Emmert–Teller) ในช่วง P/P_0 = 0.05 ถึง 0.30

2.2.6 การวิเคราะห์พื้นที่ผิวของคอปเปอร์

ในปฏิกิริยาการเติมก๊าซไฮโดรเจนของก๊าซคาร์บอนไดออกไซด์ โลหะคอปเปอร์ถือว่าเป็นตัวเร่งปฏิกิริยาหลัก ดังนั้นการปริมาณพื้นที่ผิวที่ว่องไวในการเกิดปฏิกิริยาของโลหะคอปเปอร์จึงเป็นเรื่องสำคัญมาก โดยพื้นที่ผิวของโลหะคอปเปอร์จะคิดจาก วิธีการดูดซับทางเคมีด้วยก๊าซไนตรัสออกไซด์

2.2.7 การวิเคราะห์การรีดิวซ์ของคอปเปอร์ออกไซด์เป็นโลหะคอปเปอร์

การศึกษาการรีดิวซ์ของคอปเปอร์ออกไซด์ด้วยไฮโดรเจนถูกวิเคราะห์ด้วย DSC-TGA เทคนิค โดยใช้ตัวอย่าง 10 มิลลิกรัมใส่ในถ้วยอะลูมินาและทำการระเหยความชื้นด้วยอากาศแห้งที่อุณหภูมิ 200 องศาเซลเซียส เป็นเวลา 1 ชั่วโมง หลังจากลดอุณหภูมิของปฏิกรณ์ลงมาที่อุณหภูมิห้อง จากนั้นเปลี่ยนวาล์วเป็นก๊าซไฮโดรเจน แล้วเพิ่มอุณหภูมิจากอุณหภูมิห้องไปเป็น 400 องศาเซลเซียส ด้วยอัตราการให้ความร้อน 5 องศาเซลเซียสต่อนาที

2.3 การทดสอบความสามารถในการเร่งปฏิกิริยาการเติมก๊าซไฮโดรเจนของก๊าซคาร์บอนไดออกไซด์เพื่อผลิตเมทานอล

ตัวเร่งปฏิกิริยาที่เตรียมได้จะนำมาทดสอบประสิทธิภาพในการเร่งปฏิกิริยาการเติมก๊าซไฮโดรเจนของก๊าซคาร์บอนไดออกไซด์เพื่อผลิตเมทานอล โดยจะใช้ปฏิกรณ์ท่อแบบเบดนิ่งที่มีเส้นผ่ายศูนย์กลางภายใน 7.75 มิลลิเมตร โดยเริ่มแรกนำตัวเร่งปฏิกิริยา 0.5 กรัม เจือจางด้วย 0.5 กรัม ซิลิกา และนำไปบรรจุให้อยู่กึ่งกลางเทอร์โมคัปเปิล ตัวเร่งปฏิกิริยาถูกรีดิวซ์ภายใต้สภาวะความดันบรรยากาศด้วยก๊าซไฮโดรเจน ที่อัตราการไหล 80 มิลลิลิตรต่อนาที ที่อุณหภูมิ 350 องศาเซลเซียส เป็นเวลา 2 ชั่วโมง ที่อัตราการให้ความร้อน 5 องศาเซลเซียสต่อนาที ภายหลังจากกระบวนการรีดิวซ์ อุณหภูมิของปฏิกรณ์ลดลงอยู่ที่ 180 องศาเซลเซียส ภายใต้การไหลของก๊าซไนโตรเจน และทำการป้อนก๊าซผสมระหว่างก๊าซคาร์บอนไดออกไซด์และก๊าซไฮโดรเจนเข้าไปในปฏิกรณ์ที่อัตราส่วนโดยโมลเท่ากับ 1:3 โดยอัตราการไหลรวมมีค่าเท่ากับ 4,800 มิลลิลิตรต่อกรัมตัวเร่งปฏิกิริยาต่อชั่วโมง ทำการเพิ่มความดันของปฏิกรณ์จนมีค่าเท่ากับ 20 บาร์ ผลิตภัณฑ์ขาออกจะถูกวิเคราะห์ด้วยทคนิคแก๊สโครมาโทกราฟี โดยการวิเคราะห์ ก๊าซไฮโดรเจน ก๊าซคาร์บอนมอนออกไซด์ ก๊าซคาร์บอนไดออกไซด์ ก๊าซไนโตรเจน และน้ำ จะถูกวิเคราะห์ด้วย แก๊สโครมาโทรกราฟ รุ่น GC-2014 จากบริษัท Shimadzu โดยใช้ดีเทคเตอร์ชนิด Thermal conductivity และใช้คอลัมน์ชนิด Unibead-C ส่วนผลิตภัณฑ์ที่เป็นพวกไฮโดรคาร์บอน ใช้แก๊สโครมาโทรกราฟ รุ่น GC-8A จากบริษัท Shimadzu โดยใช้ดีเทคเตอร์ชนิด Flame ionization และใช้คอลัมน์ชนิด Porapaq-Q

3. ผลการทดลองและการอภิปายผลการทดลอง

รูปที่ 1 แสดงการเสถียรทางความร้อนของผลิตภัณฑ์ที่สังเคราะห์ที่ค่าพีเอช 7 และปริมาณความเข้มข้นของไคโตซานต่างๆ เมื่อไม่ใช้ไคโตซานเป็นสารช่วยตกตะกอนพบพีคดูดความร้อนหนึ่งพีค และพีคคายความร้อนสองพีคที่อุณหภูมิ 135 228 และ 259 องศาเซลเซียส ตามลำดับ พีคดูดความร้อนสอดคล้องกับปริมาณน้ำหนักสารที่หายไป 10 เปอร์เซ็นต์ซึ่งเกี่ยวข้องกับการสูญเสียน้ำใน

โครงสร้าง ปริมาณการสูญเสียน้ำหนักประมาณ 52 เปอร์เซ็นต์ ระหว่าง 200 ถึง 280 องศาเซลเซียส สามารถอธิบายได้จากการสลายตัวจาก ซิงค์ไฮดรอกไซด์เป็นซิงค์ออกไซด์ และคอปเปอร์ไฮดรอกไซด์เป็นคอปเปอร์ออกไซด์ เมื่อทำการเติมไคโตซานลงไป พบว่าพีคการดูดความร้อนซึ่งเป็นการกำจัดน้ำออกจากโครงสร้างยังคงอยู่ แต่พีคการคายความร้อนพีคแรกขยับตำแหน่งจาก 228 เป็น 203 องศาเซลเซียส พร้อมกับแสดงการเปลี่ยนแปลงน้ำหนักของสารอย่างทันทีทันใด บ่งบอกว่าเกิดการเผาไหม้อัตโนมัติเกิดขึ้น โดยไคโตซานที่เติมลงไปทำหน้าที่เป็นเชื้อเพลิง น้ำหนักที่ลดลงที่เหลืออยู่อีก 14 เปอร์เซ็นต์ ในช่วงอุณหภูมิ 203 ถึง 265 องศาเซลเซียส สามารถเป็นเนื่องจาก การสลายตัวที่ไม่สมบูรณ์ของ ซิงค์ไฮดรอกไซด์และคอปเปอร์ไฮดรอกไซด์ และเมื่อเพิ่มปริมาณไคโตซานไปเป็น 0.0060 กรัมต่อมิลลิลิตร การสลายตัวเกิดขึ้นภายในขั้นตอนเดียว ซึ่งสามารถเป็นเนื่องจากพลังงานที่เพิ่มมากขึ้นจากเชื้อเพลิงที่มากขึ้น อย่างไรก็ตามพีคการคายความร้อนมีการเลื่อนไปที่ตำแหน่งอุณหภูมิที่สูงขึ้นเป็น 209 องศาเซลเซียส ซึ่งสูงกว่าตัวเร่งปฏิกิริยาที่ใช้ปริมาณไคโตซานที่ต่ำกว่า (0.0030 กรัมต่อมิลลิลิตร) เหตุการณ์นี้สามารถเป็นเนื่องไคโตซานถูกโลหะออกไซด์ล้อมไว้ทำให้ทำหน้าที่ของตัวมันได้ไม่เต็มที่ เมื่อศึกษาที่ค่าพีเอชอื่นๆพบว่าให้ผลที่เหมือนกับการสังเคราะห์ตัวเร่งที่ค่าพีเอช 7 จึงสรุปได้ว่าไคโตซานทำหน้าที่เป็นเชื้อเพลิงสำหรับช่วยในการเผาไหม้ให้เกิดขึ้นได้ที่อุณหภูมิต่ำกว่าตัวเร่งปฏิกิริยาที่เตรียมโดยไม่ใช้ไคโตซานเป็นสารช่วยตะตะกอนร่วม

โครงสร้างของตัวเร่งปฏิกิริยาคอปเปอร์ออกไซด์และซิงค์ออกไซด์ที่เตรียมได้ถูกนำมาถ่ายภาพด้วยกล้องจุลทรรศน์อิเล็กตรอนแบบส่องกราดและผลที่จะแสดงในรูปที่ 2 เมื่อไม่มีการเติมไคโตซาน (รูปที่ 2a ถึง2c) จะได้ 2 โครงสร้างที่แตกต่างกันอย่างชัดเจน โครงสร้างหนึ่งเป็นการรวมตัวกันของผลึกที่มีลักษณะเป็นแผ่นๆ อีกโครงสร้างหนึ่งเป็นการรวมตัวกันของผลึกที่มีรูปร่างไม่เป็นระเบียบ ผลึกแผ่นมีขนาดประมาณ 300 ถึง 500 นาโนเมตร ซึ่งใหญ่กว่าผลึกที่มีรูปร่างไม่เป็นระเบียบ (100 ถึง 300 นาโนเมตร) ผลการวิเคราะห์องค์ประกอบธาตุพบว่าซิงค์ออกไซด์เป็นองค์ประกอบโดยส่วนใหญ่ของผลึกแผ่น ในขณะที่คอปเปอร์ออกไซด์เป็นองค์ประกอบโดยส่วนใหญ่ของผลึกที่มีรูปร่างไม่เป็นระเบียบ ผลลัพธ์นี้บ่งบอกว่าซิงค์ออกไซด์และคอปเปอร์ออกไซด์เกิดแยกจากกัน เมื่อมีการเติม 0.0015 กรัมต่อมิลลิลิตร (รูปที่ 2d ถึง2f) ไคโตซานลงไปในสารละลาย พบทรงกลมกลวงเกิดขึ้นซึ่งมีขนาดเฉลี่ยประมาณ 300 ถึง 500 นาโนเมตร ที่กำลังขยายสูงขึ้นพบว่าพื้นผิวของทรงกลมกลวงประกอบไปด้วยผลึกระดับนาโนมากมาย เมื่อมีการเพิ่มปริมาณไคโตซานเป็น 0.0030 กรัมต่อมิลลิลิตร (รูปที่ 2g ถึง2i) พบว่าขนาดของทรงกลมกลวงเล็กลงกว่าในกรณีที่ใช้ไคโตซาน 0.0015 กรัมต่อมิลลิลิตร พร้อมทั้งความเป็นทรงกลมกลวงเดี่ยวหายไป เกิดการเชื่อมต่อกันระหว่างทรงกลมแทน และเมื่อยังคงเพิ่มปริมาณไคโตซานต่อไปเป็น 0.0045 กรัมต่อมิลลิลิตร (รูปที่ 2g ถึง2i) จะไม่สามารถสังเกตุเห็นอีกต่อไป แต่จะเห็นเป็นการรวมกลุ่มกันของอนุภาคระดับนาโนแทน เมื่อวิเคราะห์องค์ประกอบธาตุของตัวเร่งปฏิกิริยาที่เตรียมจากการใช้ไคโตซานเป็นสารช่วยตกตะกอนร่วมพบว่า เมื่อใช้ไคโตซาน 0.0015 กรัมต่อมิลลิตร คิดอัตราส่วนของคอปเปอร์ต่อซิงค์ได้เป็น 0.93 ซึ่งบ่งบอกว่ามีการกระจายตัวของคอปเปอร์ออกไซด์และซิงค์ออกไซด์อย่างสม่ำเสมอในโครงสร้างของตัวเร่งปฏิกิริยา แสดงให้เห็นว่าไคโตซานสามารถใช้เป็นสารช่วยในการตกตะกอนร่วม

ของคอปเปอร์ออกไซด์และซิงค์ออกไซด์ได้ อย่างไรก็ตามเมื่อเพิ่มความเข้มข้นของไคโตซานมากขึ้น อัตราส่วนของคอปเปอร์ต่อซิงค์ลดลงเป็น 0.85 และ 0.75 สำหรับปริมาณไคโตซาน 0.0030 และ 0.0045 กรัมต่อมิลลิตร ตามลำดับ แสดงให้เห็นว่าความเข้มข้นของไคโตซานที่ 0.0015 กรัมต่อมิลลิตร เป็นปริมาณที่เหมาะสม

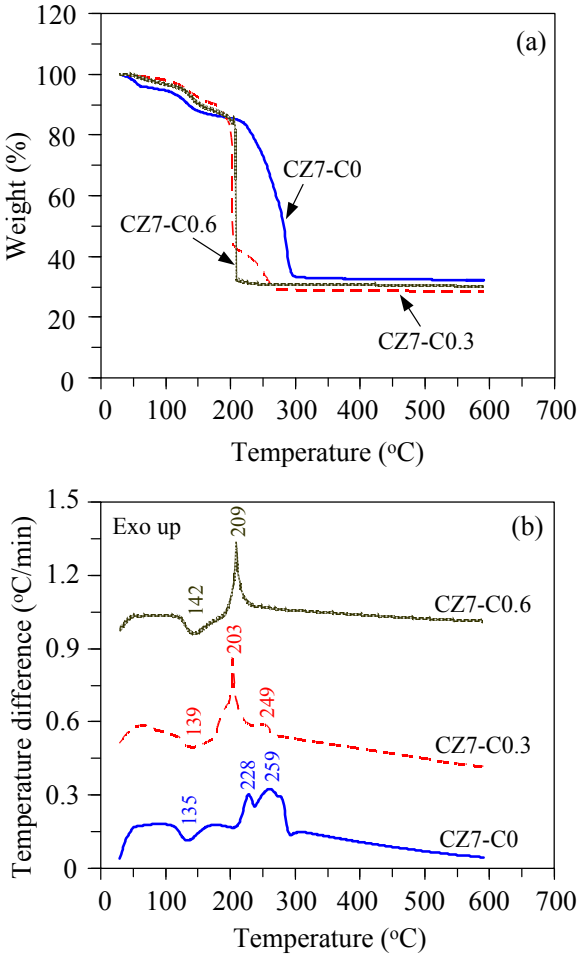

รูปที่ 1 การวิเคราะห์ความเสถียรทางความร้อน (a) และผลต่างของอุณหภูมิ (b) ของผลิตภัณฑ์ที่สังเคราะห์ที่ค่าพีเอช 7 และปริมาณไคโตซานต่างๆ

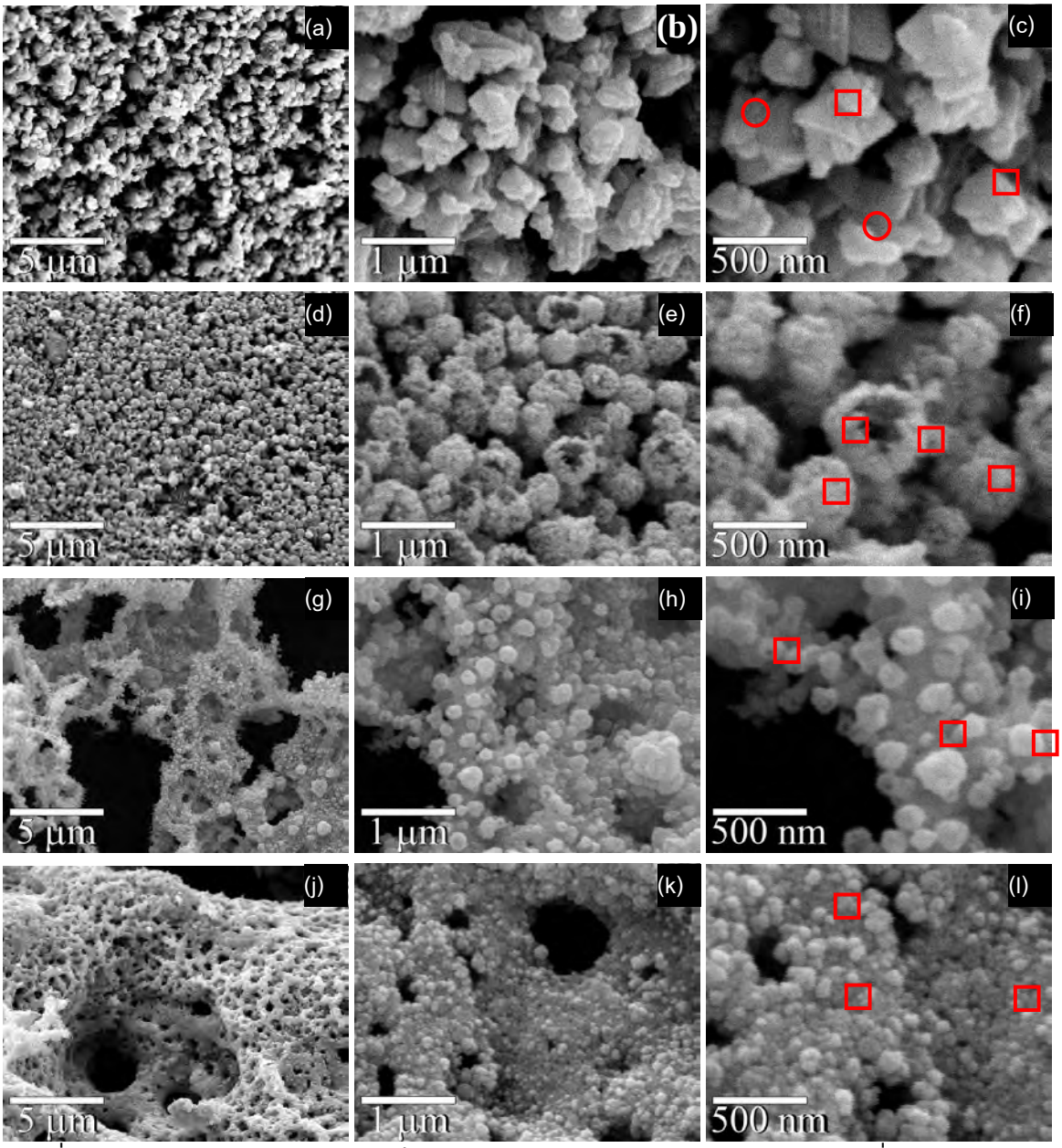

รูปที่ 2 ภาพถ่ายด้วยกล้องจุลทรรศน์อิล็กตรอนแบบส่องกราดของตัวเร่งปฏิกิริยาที่เตรียมจากค่าพีเอช 7 และความเข้มข้นของไคโตซานเป็น 0 (a ถึง c) 0.0015 (d ถึง f) 0.0030 (g ถึง i) และ 0.0045 (j ถึง c) กรัมต่อมิลลิลิตร

รูปที่ 3 แสดงผลการวิเคราะห์เฟสและขนาดผลึกของผลิตภัณฑ์ที่เตรียมที่ความเข้มข้นของไคโตซานต่างๆ พบว่า รูปแบบ XRD แสดงพีคที่ตำแหน่ง 32.54 °, 35.52°, 38.81°, 48.56° and 61.50° ซึ่งเป็นการบ่งบอกถึงเฟสคอปเปอร์ออกไซด์ที่เป็นโมโนคลินิคซึ่งสอดคล้องกับพีคมาตรฐาน JCPDS 05-0661 ในขณะที่พีคอื่นๆตรงกับพีคมาตรฐานของซิงค์ออกไซด์ (JCPDS 36-1451) สารตัวอย่างทั้งหมดแสดงพีคที่ตำแหน่งเดียวกันซึ่งเป็นการบ่งบอกว่าไคโตซานที่เติมลงไปจะไม่ไปเปลี่ยนแปลงความเป็นผลึกของสารตัวอย่าง พีคที่สูงสุดของคอปเปอร์ออกไซด์และซิงค์ออกไซด์ที่ตำแหน่ง 35.52° และ 36.25° ตามลำดับ ถูกใช้ในการคำนวนหาขนาดผลึกเฉลี่ยด้วยสมการ Scherrer จาก

ตารางที่ 1 สามารถเห็นได้ว่าขนาดผลึกของคอปเปอร์ออกไซด์และซิงค์ออกไซด์ที่สังเคราะห์โดยไม่ใช้ไคโตซาน มีค่าเท่ากับ 20.4 และ 29.1 นาโนเมตร ตามลำดับ เมื่อมีการเติมไคโตซานลงไป พบว่าขนาดผลึกเฉลี่ยของตัวเร่งปฏิกิริยาทั้ง 3 ตัวมีขนาดเล็กลง ที่ความเข้มข้นไคโตซาน 0.0015 กรัมต่อมิลลิลิตร พบว่าขนาดผลึกเล็กลงไปถึง 43.6 เปอร์เซ็นต์ และ 35.4 เปอร์เซ็นต์ เมื่อเทียบกับขนาดผลึกเฉลี่ยของตัวเร่งที่เตรียมโดยไม่ใส่ไคโตซาน ตามลำดับ อย่างไรก็ตามเมื่อปริมาณไคโตซานเพิ่มมากขึ้น การลดลงของขนาดผลึกน้อยลง ที่ความเข้มข้นไคโตวาน 0.0045 กรัมต่อมิลลิลิตร พบว่าขนาดผลึกลดลงเพียงแค่ 20.6 และ 10.0 เปอร์เซ็นต์ สำหรับคอปเปอร์ออกไซด์และซิงค์ออกไซด์ตามลำดับ

จากผลการทดลองดังกล่าว ไคโตซานที่เติมลงไปมีบทบาทในการใช้เป็นตัวตกตะกอนร่วมและลดขนาดของโลหะออกไซด์ ซึ่งภายในโมเลกุลของไคโตซานเองจะมีหมู่เอมีนและไฮดรอกไซด์ ซึ่งสามารถที่จะเกิดอันตรปฏิกิริยากับโลหะออกไซด์ได้ ทำให้ปริมาณของโลหะที่จะไปฟอร์มตัวให้อนุภาคมีขนาดใหญ่ขึ้นลดลง อย่างไรก็ตามเมื่อเพิ่มปริมาณไคโตซานทำให้ได้โครงร่างของไคโตซานที่หนาแน่นมากขึ้น โลหะไม่สามารถที่จะแพร่ไปด้านในได้สะดวกและเกิดการร่วมตัวกันอยู่ที่ด้านนอกโครงร่างของไคโตซานเท่านั้น ทำให้ไคโตซานไม่สามารถที่จะป้องกันการเติบโตของผลึกโลหะออกไซด์

ตารางที่ 1 องค์ประกอบที่พื้นผิวคิดจากค่าเฉลี่ย และขนาดผลึกของโลหะออกไซด์ขนิดต่างๆ

ตัวอย่าง [a]	ตำแหน่ง	Cu/Zn	ขนาดโลหะออกไซด์เฉลี่ย (นาโนเมตร)	
			CuO [b]	ZnO [b]
CZ-0	สี่เหลี่ยม	0.14	20.4	29.1
	วงกลม	2.72		
CZ-0.0015	สี่เหลี่ยม	0.93	11.5	18.8
CZ-0.0030	สี่เหลี่ยม	0.85	13.5	23.4
CZ-0.0045	สี่เหลี่ยม	0.75	16.2	26.2

[a] ตัวอย่างทั้งหมดให้สัญลักษณ์เป็น CZ-*x* ที่ซึ่ง *x* คือความเข้มข้นของไคโตซานในหน่วย กรัมต่อมิลลิลิตร

[b] ขนาดผลึกของคอปเปอร์ออกไซด์และซิงค์ออกไซด์คำนวนจากสมการ Scherrer โดยใช้พีคที่สูงสุดที่ 35.52° and 36.25° ตามลำดับ

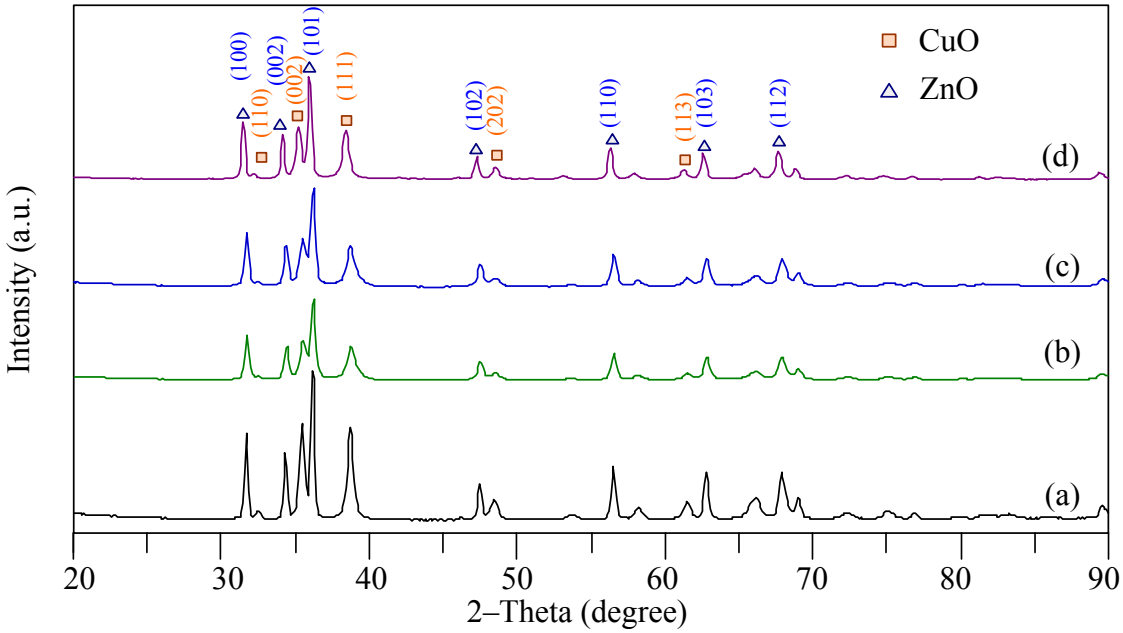

รูปที่ 3 เฟสและองค์ประกอบของตัวเร่งปฏิกิริยา (a) CZ-0 (b) CZ-0.0015 (c) CZ-0.0030 และ (d) CZ-0.0045

รูปที่ 4 แสดงไอโซเทอมและการกระจายตัวของรูพรุนของตัวอย่างซึ่งถูกวิเคราะห์ด้วยเทคนิคการดูดซับด้วยก๊าซไนโตรเจน ในขณะที่พื้นที่ผิวและปริมาตรรูพรุนรวมแสดงไว้ในตารางที่ 2 ไอโซเทอมของผลิตภัณฑ์ที่เตรียมโดยไม่ใช้ไคโตซานมีปริมาตรการดูดซับก๊าซไนโตรเจนที่ต่ำมาก บ่งบอกว่าวัสดุที่ได้เป็นแบบไม่มีรูพรุน (รูปที่ 4a) ในขณะที่การกระจายตัวของรูพรุนมีค่าต่ำมากและมีรูพรุนหลากหลายชนิด (รูปที่ 4e) เมื่อมีการใช้ไคโตซานเป็นสารช่วยตกตะกอน (รูปที่ 4b) พบว่าไอโซเทอมเป็นแบบชนิดที่ 2 ซึ่งบ่งบอกการมีอยู่ของรูพรุนระดับมาโครพอร์ ที่ความเข้มข้นไคโตซาน 0.0015 กรัมต่อมิลลิลิตร การกระจายตัวของรูพรุนเป็นแบบสองรูพรุน (รูปที่ 4d) ที่ตำแหน่ง 42 และ 215 นาโนเมตร ซึ่งสามารถอธิบายได้จากรูพรุนจากช่องว่างของการรวมกันของอนุภาคระดับนาโนและรูพรุนขนาดใหญ่เกิดเนื่องจากรูพรุนที่เป็นช่องเปิดของทรงกลมกลวงที่เห็นได้จากภาพถ่ายรูปที่ 3f เมื่อมีการเพิ่มความเข้มข้นไคโตซานต่อไปอีกที่ 0.0030 และ 0.0045 กรัมต่อมิลลิลิตร (รูปที่ 4c) พบว่ารูพรุนขนาดใหญ่หายไป ในขณะที่รูพรุนขนาดเล็กโตขึ้นจาก 42 ไปเป็น 60 และ 80 นาโนเมตร ตามลำดับ

พื้นที่ผิวและปริมาตรรูพรุนรวมของตัวเร่งปฏิกิริยาที่เตรียมโดยไม่ใส่ไคโตซานมีค่าเป็น 14.5 ตารางเมตรต่อกรัม และ 0.06 มิลลิลิตรต่อกรัม ตามลำดับ เมื่อมีการเติมไคโตซานที่ความเข้มข้น 0.0015 กรัมต่อมิลลิลิตร ลงไปพบว่าพื้นที่ผิวมีค่าสูงขึ้นเป็น 46.2 ตารางเมตรต่อกรัม และปริมาตรรูพรุนสูงถึง 0.16 มิลลิลิตรต่อกรัม เมื่อเพิ่มปริมาณไคโตซานมากขึ้น พื้นที่ผิวและปริมาตรรูพรุนของตัวเร่งปฏิกิริยากลับมีค่าลดลง แต่ยังคงสูงกว่าในกรณีที่ไม่มีการเติมไคโตซาน

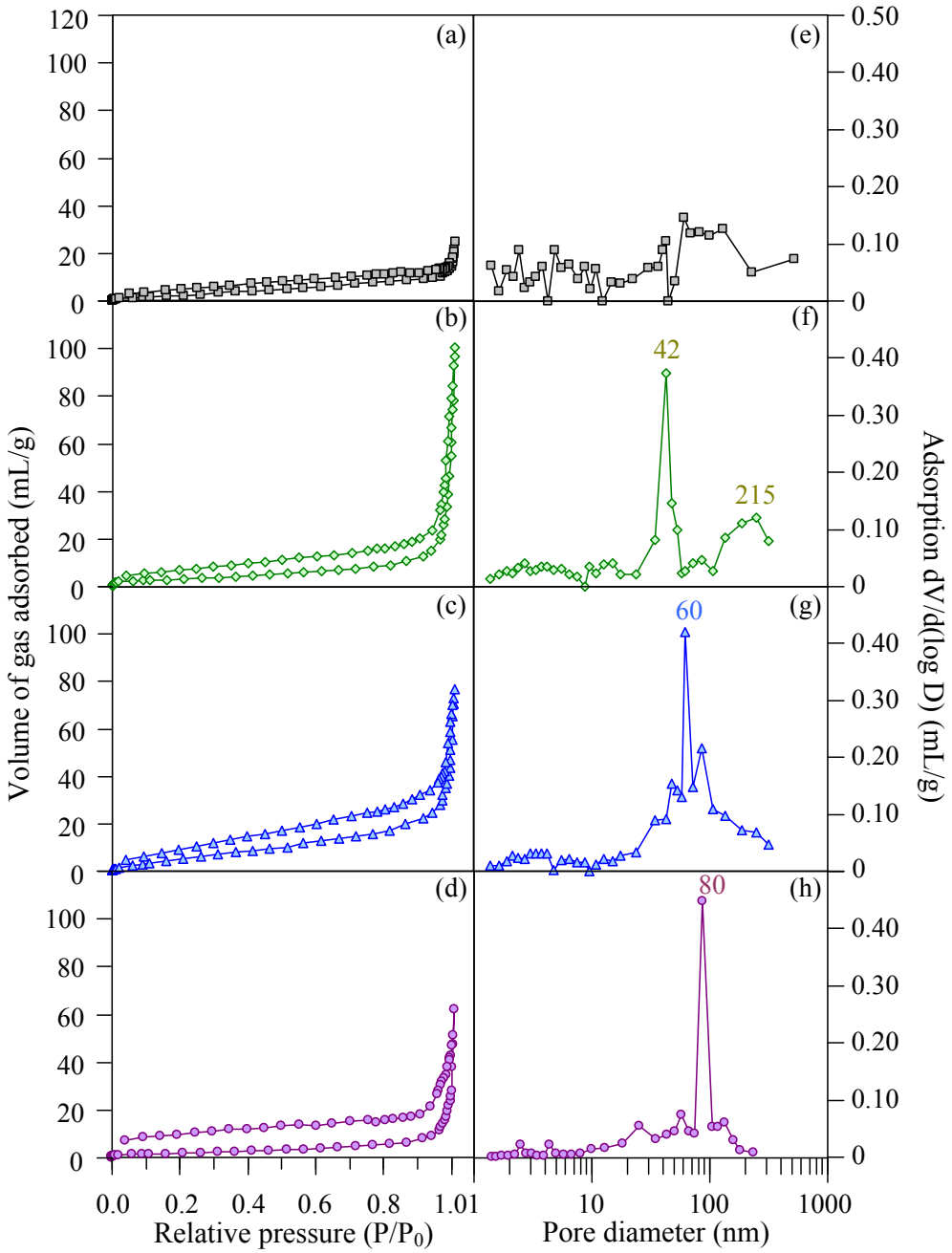

รูปที่ 4 ไอโซเทอม (a ถึง d) และการกระจายตัวของรูพรุน (e ถึง h) ของตัวเร่งปฏิกิริยา CZ-0 (a และ e) CZ-0.0015 (b และ f) CZ-0.0030 (c และ g) และ CZ-0.0045 (d และ h)

ตารางที่ 2 แสดงขนาดรูพรุนเฉลี่ย พื้นที่ผิว ปริมาตรรูพรุนและพื้นที่ผิวของคอปเปอร์

ตัวเร่งปฏิกิริยา	ขนาดรุพรุนเฉลี่ย (นาโนเมตร)	พื้นที่ผิว (ตารางเมตรต่อกรัม)	ปริมาตรรูพรุน (มิลลิลิตรต่อกรัม)	พื้นที่ผิวคอปเปอร์ (ตารางเมตรต่อกรัม)
CZ-0	-	14.5	0.06	5.5
CZ-0.0015	42 and 215	46.2	0.16	15.4
CZ-0.0030	60	34.5	0.13	12.5
CZ-0.0045	80	28.4	0.11	8.4

รูปที่ 5 แสดงการพฤติกรรมการรีดิวซ์ของคอปเปอร์ออกไซด์ไปเป็นคอปเปอร์ จะเห็นได้ว่าตัวเร่งปฏิกิริยา CZ-0 แสดงพีคการคายความร้อน 2 พีค ที่ตำแหน่งอุณหภูมิ 465 เคลวิน และ 471 เคลวิน ซึ่งบ่งบอกถึงการมีคอปเปอร์สปีชีร์อยู่ 2 สปีชีร์ พีคที่ตำแหน่งอุณหภูมิต่ำกว่าสามารถอธิบายได้จากการรีดิวซ์ของคอปเปอร์ที่กระจายตัวดี ในขณะที่อีกพีคหนึ่งคือการรีดิวซ์ของบัลค์คอปเปอร์ออกไซด์ ผลการทดลองนี้เปิดเผยว่าคอปเปอร์ส่วนใหญ่ตกตะกอนแยกจากซิงค์ออกไซด์และส่วนน่อยเท่านั้นของคอปเปอร์ที่รวมอยู่กับซิงค์ออกไซด์ เมื่อมีการเติมไคโตซานลงไป 0.0015 กรัมต่อมิลลิลิตร พบพีคคายความร้อนเพียงแค่พีคเดียวเท่านั้น ที่อุณหภูมิ 461 เคลวิน ซึ่งบ่งบอกการกระจายตัวของคอปเปอร์ออกไซด์เฟสในคอปเปอร์ออกไซด์-ซิงค์ออกไซด์ คอมโพซิท เมื่อเพิ่มปริมาณความเข้มข้นของไคโตซานเป็น 0.0030 และ 0.0045 กรัมต่อมิลลิลิตร พบว่าพีคคายความร้อนกลายเป็น 2 พีคเหมือนตอนเริ่มแรก แต่จุดยอดมีการเลื่อนไปที่อุณหภูมิต่ำกว่า ซึ่งแนะนำว่าคอปเปอร์ออกไซด์ที่มีขนาดเล็กกว่าสามารถรีดิวซ์ได้ง่ายกว่า มีข้อสังเกตว่าคอปเปอร์ออกไซด์ของ CZ-0.0030 และ CZ-0.0045 ซึ่งมีขนาดใหญ่กว่าคอปเปอร์ออกไซด์ของ CZ-0.0015 สามารถถูกรีดิวซ์ได้ง่ายกว่า นี้อาจจะเป็นเพราะว่าการที่ CZ-0.0015 มีการผสมกันอย่างสม่ำเสมอของคอปเปอร์ออกไซด์และซิงค์ออกไซด์ ทำให้เกิดอันตรกิริยาที่สูงกว่า จึงเกิดการรีดิวซ์ได้ยาก

ในการเร่งปฏิกิริยาการผลิตเมทานอลจากปฏิกิริยาการเติมก๊าซไฮโดรเจนของก๊าซคาร์บอนไดออกไซด์นั้น โลหะคอปเปอร์จะทำหน้าที่หลักในการเร่งปฏิกิริยา ดังนั้นการวิเคราะห์หาพื้นที่ผิวของคอปเปอร์จึงเป็นสิ่งที่จำเป็น จากตารางที่ 2 พบว่า ตัวเร่งปฏิกิริยาที่เตรียมโดยใช้ไคโตซาน 0.0015 กรัมต่อมิลลิลิตรให้พื้นที่ผิวสูงสุดที่ 15.4 ตารางเมตรต่อกรัม รองลงมาเป็น CZ-0.0030 CZ-0.0045 และตัวเร่งปฏิกิริยาที่เตรียมโดยไม่ใส่ไคโตซานจะให้พื้นที่ผิวต่ำสุดที่ 5.5 ตารางเมตรต่อกรัม

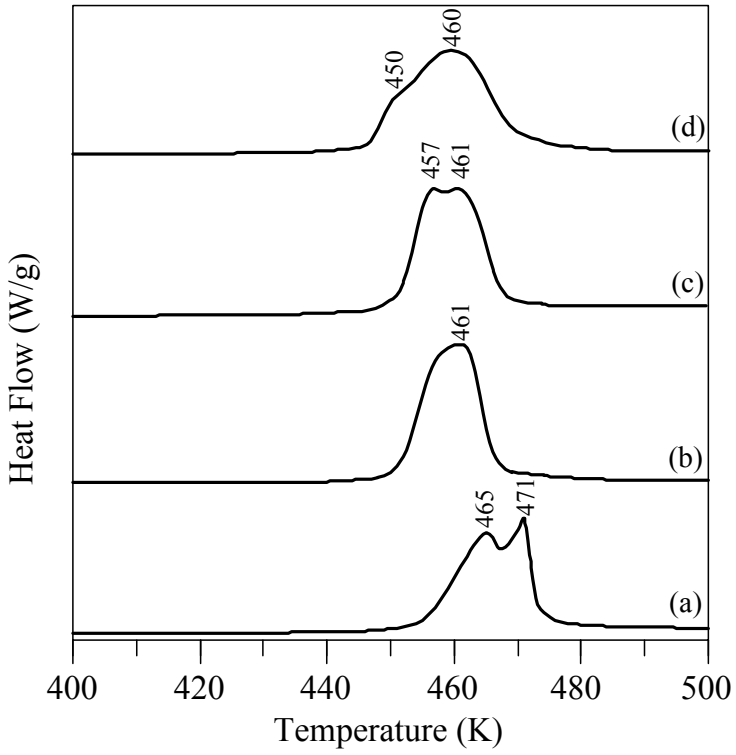

รูปที่ 5 พฤติกรรมการรีดิวซ์ของตัวเร่งปฏิกิริยาชนิดต่างๆ (a) CZ-0 (b) CZ-0.0015 (c) CZ-0.0030 และ (d) CZ-0.0045

เมื่อทราบคุณลักษณะทางกายภาพและทางเคมีของตัวเร่งปฏิกิริยาที่เตรียมโดยใช้และไม่ใช้ไคโตซานเป็นสารตกตะกอนร่วมแล้ว จึงนำตัวเร่งปฏิกิริยาที่เตรียมได้มาทดสอบการเร่งปฏิกิริยาการสังเคราะห์เมทานอลจากปฏิกิริยาการเติมก๊าซไฮโดรเจนของก๊าซคาร์บอนไดออกไซด์ โดยทำปฏิกิริยาที่ความดัน 20 บาร์และปรับเปลี่ยนอุณหภูมิในการทำปฏิกิริยา 5 ค่าได้แก่ 180 200 220 240 260 องศาเซลเซียส ได้ผลดังนี้ เมื่อมีการเพิ่มอุณหภูมิจาก 180 องศาเซลเซียสไปที่ 240 องศาเซลเซียส ค่าการแปลงผันของก๊าซคาร์บอนไดออกไซด์เพิ่มมากขึ้นเรื่อยๆ และนอกจากนี้ไม่พบการเสื่อมสภาพของตัวเร่งปฏิกิริยาเนื่องจากค่าการแปลงผันไม่ได้ลดลงเมื่อเวลาเปลี่ยนไป และเห็นได้ชัดเจนว่าตัวเร่งปฏิกิริยาที่เตรียมโดยใช้ไคโตซานเป็นสารช่วยตกตะกอนให้ค่าการแปลงผันที่สูงกว่าตัวเร่งปฏิกิริยาที่ไม่ใช้ไคโตซานช่วยตกตะกอน ที่อุณหภูมิ 260 องศาเซลเซียส ค่าการแปลงผันของก๊าซคาร์บอนไดออกไซด์ของตัวเร่งปฏิกิริยาทุกตัวยังคงเพิ่มขึ้น อย่างไรก็ตาม สัญญาณของการเสื่อมสภาพของตัวเร่งปฏิกิริยาเริ่มปรากฏ โดยเห็นได้จากค่าการแปลงผันของก๊าซคาร์บอนไดออกไซด์ที่ลดลงไปเมื่อเวลาผ่านไป 10 ชั่วโมง ของตัวเร่งปฏิกิริยา CZ-0, CZ-0.0015, CZ-0.0030 และ CZ-0.0045 เป็นดังนี้ 1.32, 1.23, 3.56, และ 4.59 เปอร์เซ็นต์ ตามลำดับ

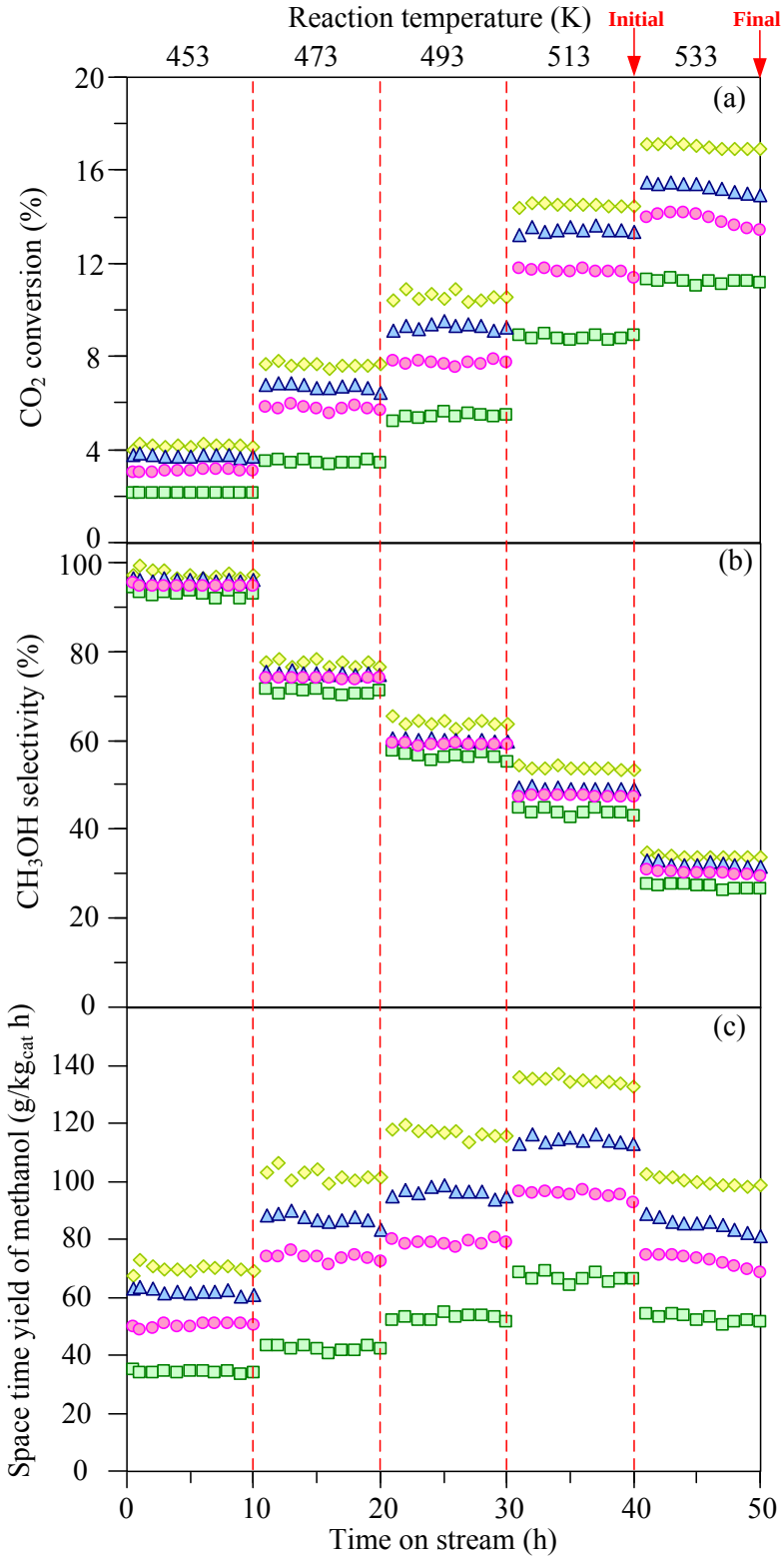

รูปที่ 6 ค่าการแปลงผันของก๊าซคาร์บอนไดออกไซด์ (a) และค่าการเลือกเกิดของเมทานอล (b) อัตราการเกิดเมทานอล (c) ของตัวเร่งปฏิกิริยา of □ CZ-0, ◇ CZ-0.0015, △ CZ-0.0030 and ○ CZ-0.0045 ที่อุณหภูมิต่าง ๆ

ค่าการเลือกเกิดเมทานอลของตัวเร่งปฏิกิริยาทุกตัวลดลงกับการเพิ่มอุณหภูมิในการทำปฏิกิริยาเนื่องจากสมดุลทางเทอร์โมไดนามิกส์ กับปฏิกิริยาการผันกลับของน้ำเกิดร่วมคู่ขนาน ในขณะที่ อัตราการเกิดเมทานอลเพิ่มขึ้นกับการเพิ่มขึ้นของอุณหภูมิในการเกิดปฏิกิริยาจาก 180 ถึง 240 องศาเซลเซียส เนื่องจากค่าการแปลงผันของก๊าซคาร์บอนไดออกไซด์ที่สูงและค่าการเลือกเกิดเมทานอลที่สูงด้วย ค่าการเลือกเกิดเมทานอลที่สูงสุดเกิดขึ้นโดยใช้ตัวเร่งปฏิกิริยา CZ-0.0015 ที่อุณหภูมิ 240 องศาเซลเซียส มีอัตราการเกิดเมทานอลเป็น 135 กรัมเมทานอลต่อกิโลกรัมตัวเร่งปฏิกิริยาต่อชั่วโมง เช่นเดียวกับค่าการแปลงผันของก๊าซคาร์บอนไดออกไซด์ อัตราการเกิดเมทานอลก็ลดลงเช่นกันสำหรับการทำปฏิกิริยาที่อุณหภูมิ 260 องศาเซลเซียส โดยพบว่าเปอร์เซ็นการลดลงของอัตราการเกิดเมทานอลเป็น 4.84, 4.05, 8.15, และ 8.00 เปอร์เซ็นต์ สำหรับตัวเร่งปฏิกิริยา CZ-0, CZ-0.0015, CZ-0.0030 และ CZ-0.0045 ตามลำดับ ซึ่งจะเห็นได้ว่าตัวเร่งปฏิกิริยาที่เตรียมด้วยความเข้มข้นของไคโตซานสูงมีโอกาสที่จะเสื่อมสภาพเร็วกว่า ตัวเร่งปฏิกิริยาที่ไม่มีการเติมไคโตซานและ เติมไคโตซานเพียง 0.0015 กรัมต่อมิลลิลิตร ซึ่งเป็นการบ่งบอกว่าผลึกคอปเปอร์ที่มีขนาดใหญ่จะมีความเสถียรมากกว่าผลึกคอปเปอร์ที่มีขนาดเล็กซึ่งสามารถที่จะถูกออกซิไดส์ไปเป็นคอปเปอร์ออกไซด์ได้ง่ายกว่า อีกประเด็นหนึ่งคือ การเสื่อมสภาพเนื่องจากการสูญเสียพื้นที่ผิวจากกระบวนการ sintering เนื่องจากอุณหภูมิสูง จากผลการวิเคราะห์คุณลักษณะก่อนหน้าเห็นได้ว่าการใช้ไคโตซานช่วยตกตะกอนร่วมสามารถทำให้คอปเปอร์มีขนาดเล็กลงและกระจายตัวได้ดีกับซิงค์ออกไซด์ อย่างไรก็ตามสำหรับ CZ-0.0030 และ CZ-0.0045 พื้นผิวของซิงค์ออกไซด์ไม่สามารถป้องกันการร่วมตัวของคอปเปอร์ที่มีขนาดนาโนได้ เนื่องจากคอปเปอร์ออกไซด์มีขนาดเล็กแต่ไม่ได้ผสมกันดีกับซิงค์ออกไซด์ทำให้มีอันตรปฏิกิริยาต่ำ และเมื่อได้รับความร้อนจึงเกิดการเคลื่อนที่ของอนุภาคคอปเปอร์มารวมตัวกันได้ ดังนั้นทำให้พื้นที่ผิวคอปเปอร์รวมลดลง

ผลของพื้นที่ผิวของคอปเปอร์ต่อปฏิกิริยาการสังเคราะห์เมทานอลจากการเติมไฮโดรเจนของก๊าซคาร์บอนไดออกไซด์ ถูกตรวจสอบที่อุณหภูมิต่างๆ และผลลัพธ์แสดงในรูปที่ 7 เห็นได้อย่างชัดเจนว่าทั้งค่าการแปลงผันของก๊าซคาร์บอนไดออกไซด์ (รูปที่ 7a) และอัตราการเกิดเมทานอล(รูปที่ 7b) เพิ่มขึ้นกับพื้นที่ผิวของคอปเปอร์ที่เพิ่มขึ้น อย่างไรก็ตาม เพียงแค่ตัวเร่งปฏิกิริยาที่เตรียมโดยใช้ไคโตซานเป็นตัวช่วยตกตะกอนร่วมเท่านั้น (CZ-0.0015, CZ-0.0030, และ CZ-0.0045) ที่ให้ความสัมพันธ์เป็นแบบเชิงเส้น ในขณะที่ตัวเร่งปฏิกิริยาที่เตรียมโดยไม่ใส่ไคโตซาน มีค่าการแปลงผันของก๊าซคาร์บอนไดออกไซด์และอัตราการเกิดเมทานอล (พื้นที่ผิวของคอปเปอร์ = 5.5 ตารางเมตรต่อกรัม) แตกต่างอย่างชัดเจนจากแนวโน้มของตัวเร่งปฏิกิริยาที่เตรียมโดยใช้ไคโตซาน (พื้นที่ผิวของคอปเปอร์ = 8.4 ถึง15.4 ตารางเมตรต่อกรัม) จากงานวิจัยก่อนหน้าพบว่าพื้นที่ผิวของคอปเปอร์ไม่ได้เป็นปัจจัยเดียวที่เร่งปฏิกิริยาการเกิดเมทานอลแต่ยังมีอิทธิพลของการผสมกันของคอปเปอร์และซิงค์ ซึ่งงานวิจัยนี้เป็นการยืนยันกับงานวิจัยก่อนหน้าว่าการผสมกันของคอปเปอร์และซิงค์ช่วยในการเร่งปฏิกิริยาการสังเคราะห์เมทานอลจากปฏิกิริยาการเติมก๊าซไฮโดรเจนของก๊าซคาร์บอนไดออกไซด์

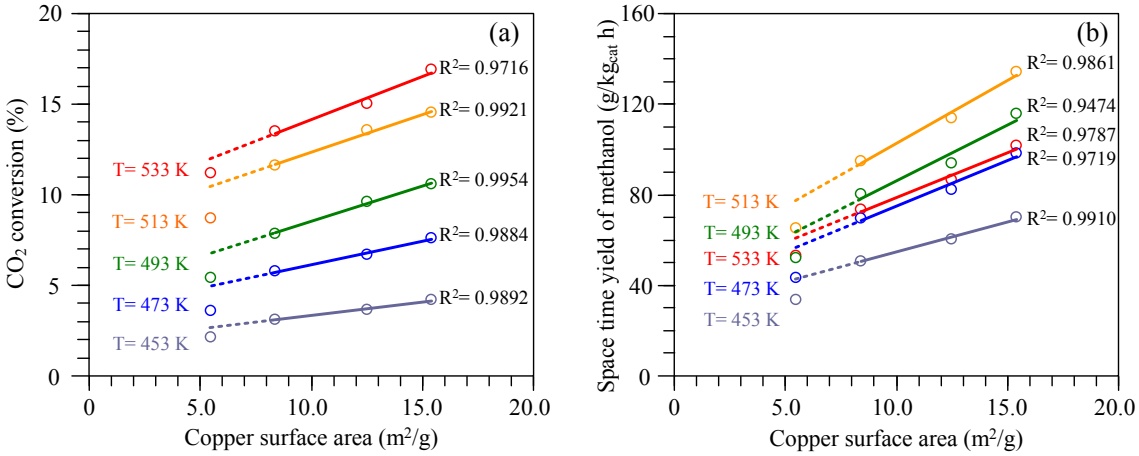

รูปที่ 7 ค่าการแปลงผันของก๊าซคาร์บอนไดออกไซด์ (a) และ อัตราการเกิดเมทานอล (b) ตามค่าพื้นที่ผิวของคอปเปอร์ที่อุณหภูมิต่าง ๆ

4. สรุปผลการทดลอง

จากผลการทดลองสรุปได้ว่า การใช้ไคโตซานเป็นสารช่วยตกตะกอนร่วมมีผลอย่างมากต่อคุณลักษณะทางกายภาพและทางเคมีของตัวเร่งปฏิกิริยาคอปเปอร์ออกไซด์และซิงค์ออกไซด์คอมโพซิท รวมทั้งประสิทธิภาพในการเร่งปฏิกิริยาการสังเคราะห์เมทานอลจากการเติมก๊าซไฮโดรเจนของก๊าซคาร์บอนไดออกไซด์ คอปเปอร์ออกไซด์-ซิงค์ออกไซด์คอมโพซิท ที่มีลักษณะเป็นทรงกลมกลวงเกิดขึ้นจากการใช้ปริมารไคโตซาน 0.0015 กรัมต่อมิลลิกรัม เมื่อเพิ่มปริมาณความเข้มข้นของไคโตซาน พบว่าทรงกลมกลวงหายไปและเกิดเป็นการรวมตัวกันเป็นกลุ่มของอนุภาคคอปเปอร์แทน ค่าการแปลงผันของก๊าซคาร์บอนไดออกไซด์และอัตราการเกิดเมทานอลของตัวเร่งปฏิกิริยาที่เตรียมโดยใช้ไคโตซานเป็นสารช่วยตกตะกอนร่วมสูงกว่าในกรณีที่ไม่ใช้ไคโตซาน อย่างไรก็ตามที่อุณหภูมิในการเกิดปฏิกิริยาสูง ตัวเร่งที่เตรียมโดยใช้ความเข้มข้นของไคโตซานสูงส่งสัญญาณบอกถึงการเริ่มเสื่อมสภาพ ซึ่งเป็นเนื่องจากคอปเปอร์ออกไซด์ที่มีขนาดเล็กและอันตรปฏิกิริยาของคอปเปอร์ออกไซด์กับซิงค์ออกไซด์ที่ต่ำทำให้เกิดการรวมตัวกันของคอปเปอร์ได้ง่าย

5. ข้อเสนอแนะสำหรับงานวิจัยในอนาคต

ตัวเร่งปฏิกิริยาคอปเปอร์ออกไซด์-ซิงค์ออกไซด์นาโนคอมโพซิทที่เตรียมได้มีความสามารถในการเร่งปฏิกิริยาได้ดี แต่มีปัญหาในการเกิดการหลอมรวมตัวกันได้ง่ายดังนั้นน่าจะมีการผสมตัวรองรับจำพวก ซิลิกา เซอร์โครเนียม หรือ คาร์บอน เข้าไปเพื่อเพิ่มอันตรปฏิกิริยาให้คอปเปอร์และซิงค์มาเกาะ

หัวข้อที่ 2 ผลของซิลิการที่มีรูพรุนสองขนาดต่อขนาดอนุภาคและการรีดิวซ์ของโคบอลต์ออกไซด์

1. วัตถุประสงค์การทดลอง

1) ศึกษาผลของตัวรองรับซิลิกาที่มีรูพรุนสองขนาดต่อขนาดอนุภาคของโคบอลต์ออกไซด์
2) ศึกษาผลของตัวรองรับซิลิกาที่มีรูพรุนสองขนาดต่อการรีดิวซ์อนุภาคโคบอลต์ออกไซด์ให้เป็นโลหะโคบอลต์
3) เปรียบเทียบผลในข้อ 1 และข้อ2 โดยใช้โคบอลต์ที่โหลดบนตัวรองรับซิลิกาที่มีรูพรุนหนึ่งขนาด

2. วิธีการทดลอง

ในงานวิจัยนี้ขั้นตอนการเตรียมจะมีอยู่ 3 หัวข้อด้วยกันแบ่งออกเป็น การสังเคราะห์ซิลิกาที่มีรูพรุน 2 ขนาด การโหลดตัวเร่งปฏิกิริยาโคบอลต์ลงบนตัวรองรับซิลิกาที่มีรูพรุนสองขนาด และการวิเคราะห์คุณสมบัติทางกายภายและทางเคมีของตัวเร่งปฏิกิริยา

2.1 การสังเคราะห์ซิลิกาที่มีรุพรุนสองขนาด

ซิลิกาที่มีรูพรุนสองขนาดจะเตรียมโดยใช้โซเดียมซิลิเกตเป็นแหล่งของซิลิกาและใช้ไคโตซานเป็นสารแม่แบบในการกำหนดรูพรุนของซิลิกา ขั้นตอนการเตรียมจะเริ่มจากการละลายไคโตซานในสารละลายกรดอะซีติก เติมโซเดียมซิลิเกตลงไปในสารละลายไคโตซาน ปรับค่ากรด-เบสเป็นค่า 3, 4 และ 5เพื่อที่จะควบคุมรูพรุนและโครงสร้าง หลังจากนั้นกวนที่อุณหภูมิ 40 องศาเซลเซียสเป็นเวลา 24 ชั่วโมง หลังจากนั้นนำเป็นเข้าเครื่อง Autoclave แล้วเก็บไว้ที่อุณหภูมิ 100 องศาเป็นเวลา 24 ชั่วโมง ของแข็งที่ได้จะถูกนำมาล้าง กรอง อบ และนำไปเผาที่อุณหภูมิ 600 องศาเซลเซียสเพื่อกำจัดไคโตซานออกไป ซิลิกาที่มีรูพรุนหนึ่งขนาดก็สามารถเตรียมได้จากวิธีการข้างต้นเพียงแต่จะไม่มีการใส่ไคโตซาน ตัวรองรับซิลิกาที่สังเคราะห์จะถูกกำหนดสัญลักษณ์เป็น BPS สำหรับซิลิกาที่มีรูพรุนสองขนาด และ UPS สำหรับซิลิกาที่มีรูพรุนหนึ่งขนาด

2.2 การโหลดตัวเร่งปฏิกิริยาโคบอลต์ลงบนตัวรองรับซิลิกาที่มีรูพรุนสองขนาด

ทำการโหลดโลหะโคบอลต์ลงไปด้วยวิธีจุ่มชุม แล้วนำสารที่เตรียมได้ไปอบที่อุณหภูมิ 120 องศาเซลเซียสเป็นเวลา 12 ชั่วโมง

2.3 การวิเคราะห์คุณสมบัติทางกายภายและทางเคมีของตัวเร่งปฏิกิริยา

ตัวรองรับซิลิกาและตัวเร่งปฏิกิริยาที่เตรียมได้จะถูกนำมาวิเคราะห์คุณสมบัติทางกายภาพและทางเคมีด้วยเทคนิคดังต่อไปนี้

- เทคนิคการดูดซับโดยใช้แก๊สไนโตรเจน เพื่อหาพื้นที่ผิว ปริมาตรรูพรุน และการกระจายตัวของรูพรุน
- เทคนิคการเลี้ยวเบนของรังสีเอ๊กซ์ เพื่อดูความเป็นผลึกของตัวเร่งและสามารถคำนวณหาขนาดของตัวเร่งได้
- เทคนิคการถ่ายภาพแบบส่องกราด จะทำให้เห็นโครงสร้างพื้นผิวของตัวรองรับและตัวเร่งปฏิกิริยา
- เทคนิคการถ่ายภาพแบบส่องผ่าน จะทำให้เห็นขนาดของตัวรองรับและตัวเร่ง และการกระจายตัวของตัวโลหะบนตัวรองรับ
- เทคนิคการศึกษาการรีดิวซ์ด้วยไฮโดรเจนเมื่อมีการเปลี่ยนแปลงอุณหภูมิ

3. ผลการทดลองและการอภิปายผลการทดลอง

จากรูปที่ 8a พบว่าไอโซเทอมของตัวรองรับซิลิกาที่มีรูพรุนหนึ่งขนาด (UPS) จะเป็นแบบชนิดที่ IV ซึ่งบ่งบอกว่าขนาดรูพรุนของซิลิกาจะอยู่ในช่วงเมโซพอร์ ในขณะที่ไอโซเทอมของตัวรองรับซิลิกาที่มีรูพรุนสองขนาด (BPS) เป็นแบบผสมระหว่างชนิดที่ IV และ II ซึ่งบ่งบอกว่ารูพรุนของซิลิกาจะมีสองขนาดที่แตกต่างกันคือขนาดเมโซพอร์และมาโครพอร์ รูปที่ 8c แสดงให้ว่าการกระจายตัวของรูพรุนของซิลิกาที่มีรูพรุนหนึ่งขนาดนั้นอยู่ในช่วงที่แคบ ในขณะที่การกระจายตัวของรูพรุนของซิลิกาที่มีรูพรุนสองขนาดนั้น รูพรุนขนาดเล็กจะมีขนาดเท่ากับซิลิกาที่มีรูพรุนหนึ่งขนาด คือ 6.5 นาโนเมตร ในขณะที่รูพรุนขนาดใหญ่จะมีขนาดประมาณ 60–200 นาโนเมตร การที่ซิลิกาที่มีรูพรุนหนึ่งขนาดและซิลิกาที่มีรูพรุนสองขนาด มีรูพรุนขนาดเมโซพอร์เท่ากันนั้นทำให้สามารถเปรียบเทียบอิทธิพลของรูพรุนขนาดใหญ่ได้อย่างยุติธรรม หลังจากทำการโหลดโคบอลต์ลงไปพบว่าลักษณะไอโซเทอม (รูปที่ 8b) และการกระจายตัวของรูพรุน (รูปที่ 8d) ยังมีลักษณะเดิมแต่จะมีปริมาณการดูดซับลดลงเล็กน้อยบ่งบอกว่าโคบอลต์ที่โหลดลงไปจะไปบดบังรูพรุนบางส่วน

จากผล X-ray diffraction (รูปที่ 9) ให้ข้อมูลว่าโคบอลต์ที่สังเคราะห์ได้อยู่ในรูปของ โคบอลต์ออกไซด์ (Co_3O_4) และสามารถคำนวนขนาดผลึกได้จากสมการของ Scherrer พบว่าได้ขนาดอนุภาคของโคบอลต์ออกไซด์ที่อยู่บนซิลิกาที่มีรูพรุนสองขนาดใหญ่ประมาณ 10.6 นาโนเมตร ซึ่งมีขนาดใหญ่กว่าอนุภาคของโคบอลต์ออกไซด์ที่อยู่บนซิลิกาที่มีรูพรุนหนึ่งขนาดคือ 9.8 นาโนเมตร ซึ่งจากผลการถ่ายภาพด้วยกล้องจุลทรรศน์อิเล็กตรอนแบบส่องกราด (รูปที่ 10) และกล้องจุลทรรศน์อิเล็กตรอนแบบส่องผ่าน (รูปที่ 11) ทำให้สรุปได้ว่าโคบอลต์ที่โหลดบนซิลิกาที่มีรูพรุนสองขนาดสะสมได้ทั้งบนรูพรุนขนาดเล็กและขนาดใหญ่ และเมื่อมีการสะสมที่รูพรุนขนาดใหญ่โคบอลต์สามารถที่จะเคลื่อนตัวมารวมตัวกันได้ง่ายทำให้ได้อนุภาคขนาดใหญ่กว่าการสะสมตัวบนรูพรุนขนาดเล็ก

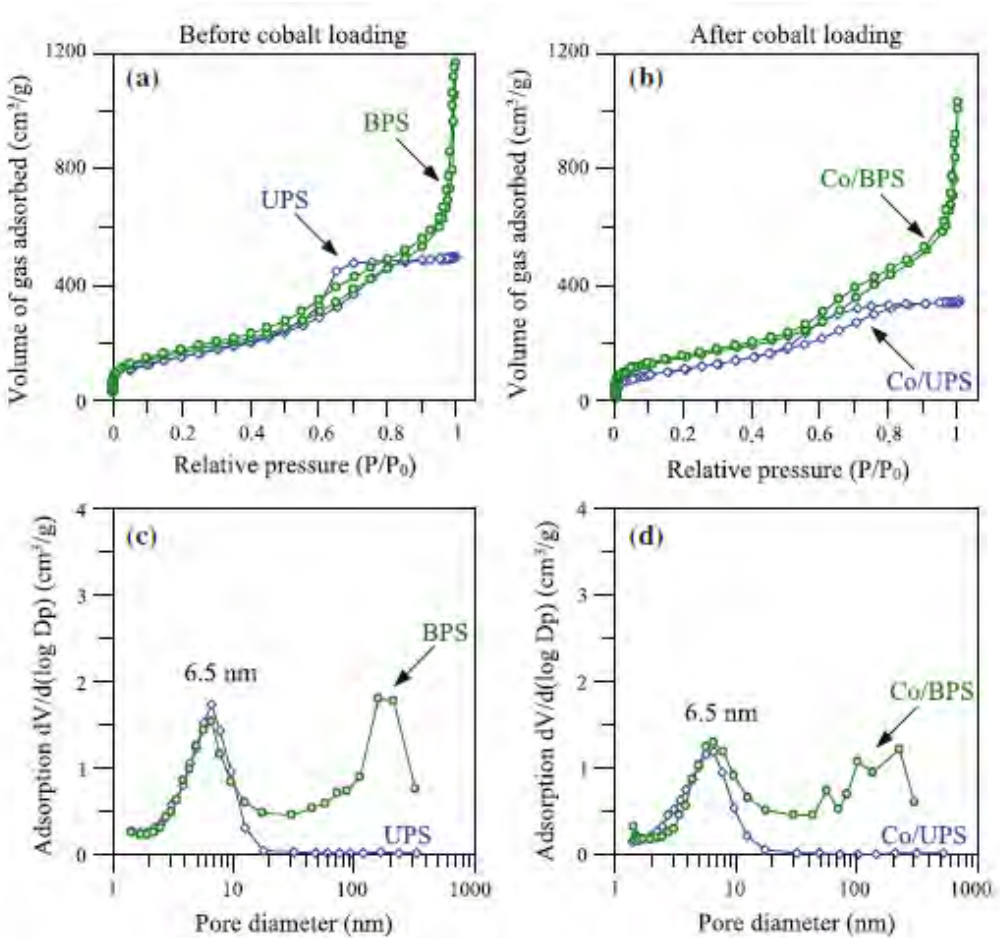

รูปที่ 8 ไอโซเทอมการดูดซับด้วยแก๊สไนโตรเจน (a และ b)และการกระจายตัวของรูพรุน (c และ d) ของตัวรองรับซิลิกาที่มีรูพรุนหนึ่งขนาด (UPS) และตัวรองรับซิลิกาที่มีรูพรุนสองขนาด (BPS) โดยที่ a และ c เป็นของซิลิกาที่ยังไม่ได้โหลดโคบอลต์ b และ d เป็นของซิลิกาที่มีการโหลดโคบอลต์แล้ว

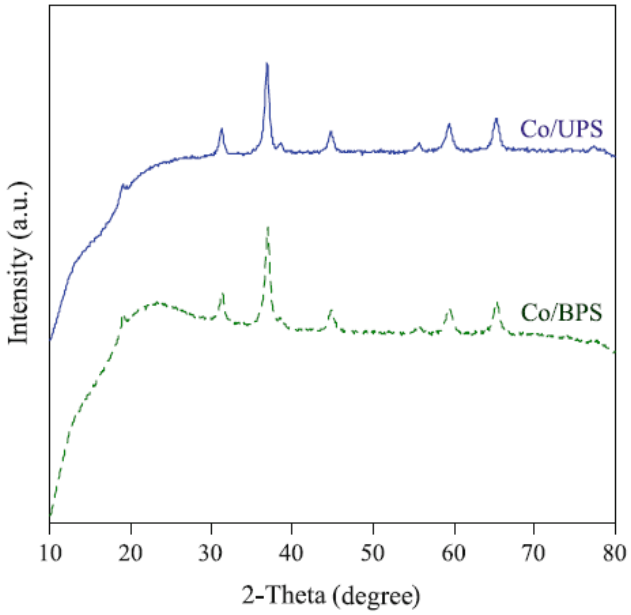

รูปที่ 9 เฟสและองค์ประกอบของ Co/UPS และ Co/BPS

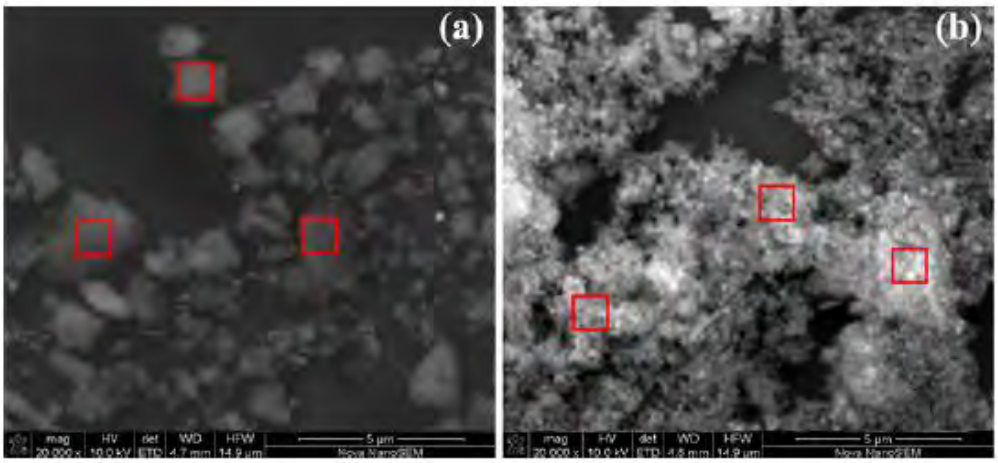

รูปที่ 10 ภาพถ่ายด้วยกล้องจุลทรรศน์อิเล็กตรอนชนิดส่องกราดของตัวเร่งปฏิกิริยาที่ผ่านการคัลไซน์ (a) Co/UPS และ (b) Co/BPS

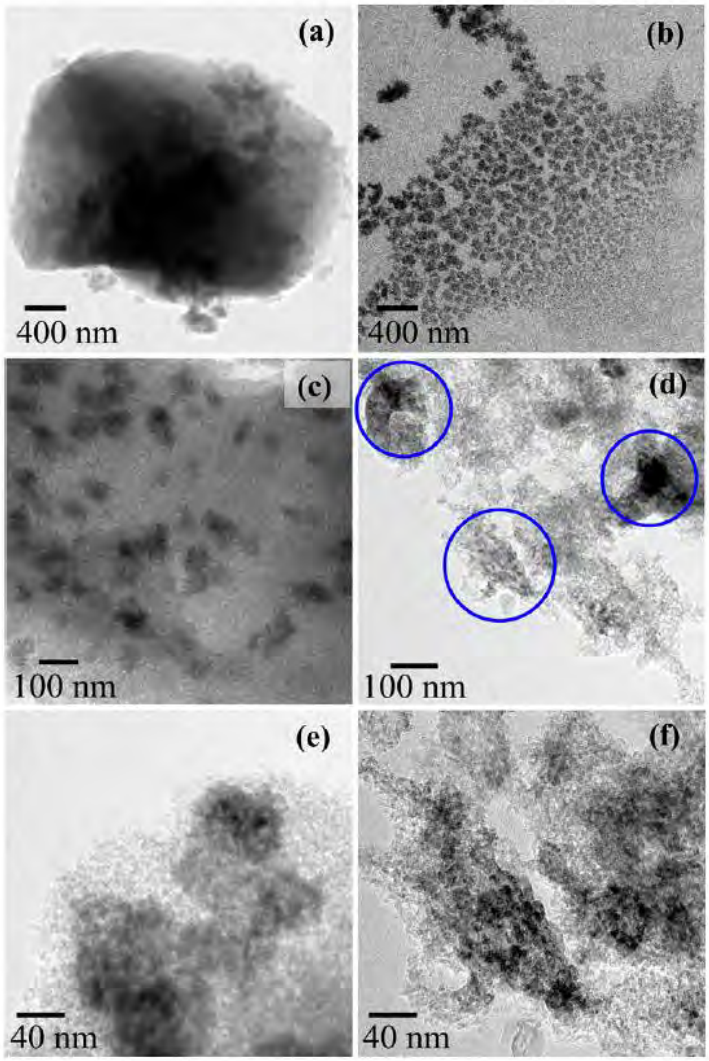

รูปที่ 11 ภาพถ่ายด้วยกล้องจุลทรรศน์อิเล็กตรอนชนิดส่องผ่านของตัวเร่งปฏิกิริยาที่ผ่านการคัลไซน์ (a,c และe) Co/UPS และ (b,d และ f) Co/BPS

จากรูปที่ 12 แสดงผลของการรีดิวซ์โคบอลต์ออกไซด์บนตัวรองรับซิลิกาที่มีรูพรุนหนึ่งขนาด (รูปที่ 12a) และโคบอลต์ออกไซด์บนตัวรองรับซิลิกาที่มีรูพรุนสองขนาด (รูปที่12b) ศึกกราฟแต่ละเส้นใช้อัตราการเพิ่มอุณหภูมิต่างกันคือ 5, 10, 15 และ 20 องศาเซลเซียสต่อนาที ซึ่งข้อมูลที่ได้สามารถนำมาคำนวนหาค่าพลังงานกระตุ้นในการรีดิวซ์ได้ จากรูปที่ 12a และ 12b พบว่าโคบอลต์ออกไซด์ถูกรีดิวซ์เป็นสองช่วง ช่วงแรกระหว่างอุณหภูมิ 260 – 270 องศาเซลเซียส เป็นการรีดิวซ์ของ Co_3O_4 ไปเป็น CoO และ ช่วงที่สองอุณหภูมิ 350 – 510 องศาเซลเซียส เป็นการรีดิวซ์ของ CoO ไปเป็น Co^0 พบว่าโคบอลต์ออกไซด์ที่โหลดบนตัวรองรับซิลิกาที่มีรูพรุนสองขนาดสามารถถูกรีดิวซ์ได้ที่อุณหภูมิต่ำกว่าโคบอลต์ออกไซด์ที่โหลดบนตัวรองรับซิลิกาที่มีรู พรุนหนึ่งขนาด

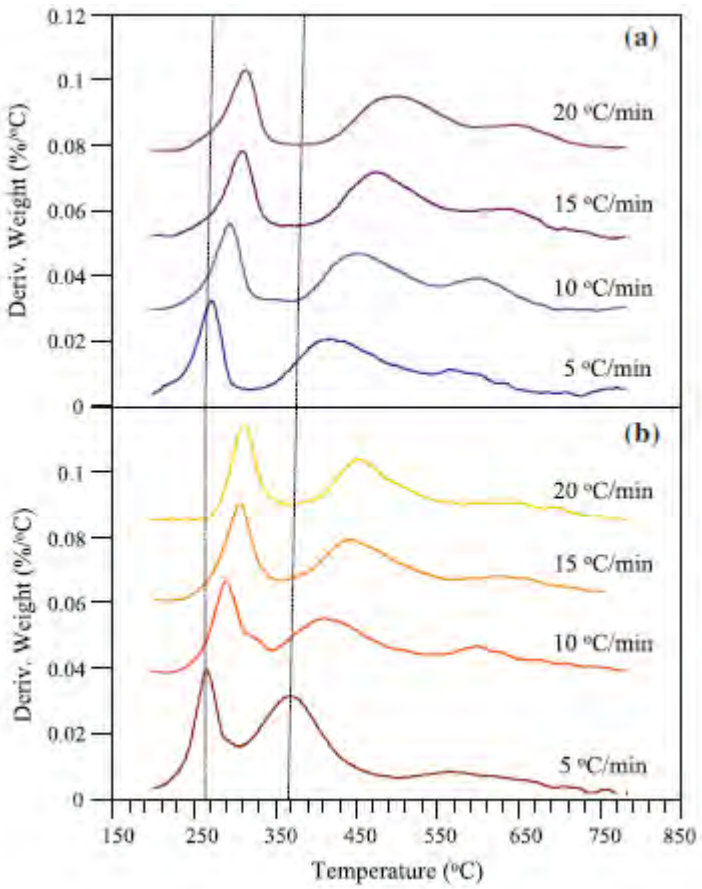

รูปที่ 12 โค้งการเปลี่ยนแปลงน้ำหนักเมื่อมีการไหลผ่านของก๊าซไฮโดรเจนที่อัตราการให้ความร้อนต่างๆ (a) Co/UPS และ (b) Co/BPS

เมื่อนำข้อมูลจากรูปที่ 4 มาหาพลังงานกระตุ้นในแต่ละขั้นตอนโดยใช้สมการของ Kissinger (สมการที่ 1)

$$\ln\left(\frac{\beta}{T_p^2}\right) = \ln\left(\frac{AR}{E}\right) - \frac{E}{R}\frac{1}{T_p} \qquad (1)$$

โดยที่ β คือ อัตราการให้ความร้อน (heating rate)

Tp คือ อุณหภูมิสูงสุดของแต่ละโค้ง

A คือ Pre-exponential factor

R คือ ค่าคงที่ของก๊าซ

E คือค่าพลังงานกระตุ้น

พบว่าโคบอลต์ออกไซด์ที่โหลดบนซิลิกาที่มีรูพรุนสองขนาดมีพลังงานกระตุ้นในการรีดิวซ์จาก Co_3O_4 ไปเป็น CoO เท่ากับ 64.55 kJ/mol และการรีดิวซ์จาก CoO ไปเป็น Co^0 48.93 kJ/mol ซึ่งต่ำกว่าโคบอลต์ ออกไซด์ที่โหลดบนซิลิกาที่มีรูพรุนหนึ่งขนาดทั้งสองขั้นตอน (รูปที่ 13) ทั้งนี้เนื่องจากโดเมนของซิลิกาที่มีรูพรุนสองขนาดจะสั้นกว่า (รูปที่ 14) ทำให้การแพร่ของก๊าซไฮโดรเจนเพื่อไปทำปฏิกิริยากับ Co_3O_4 และ CoO และการแพร่ออกของสารผลิตภัณฑ์ (น้ำ) ได้ง่ายกว่าโดเมนของซิลิกาที่มีรูพรุนหนึ่งขนาดที่มีขนาดใหญ่กว่ามาก

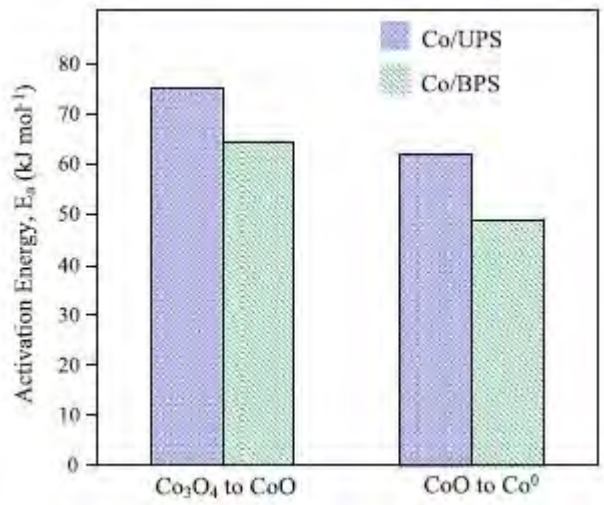

รูปที่ 13 ค่าพลังงานกระตุ้นของการรีดิวซ์ Co_3O_4 ไปเป็น CoO และ การรีดิวซ์ของ CoO ไปเป็น Co^0 ของ Co/UPS และ Co/BPS

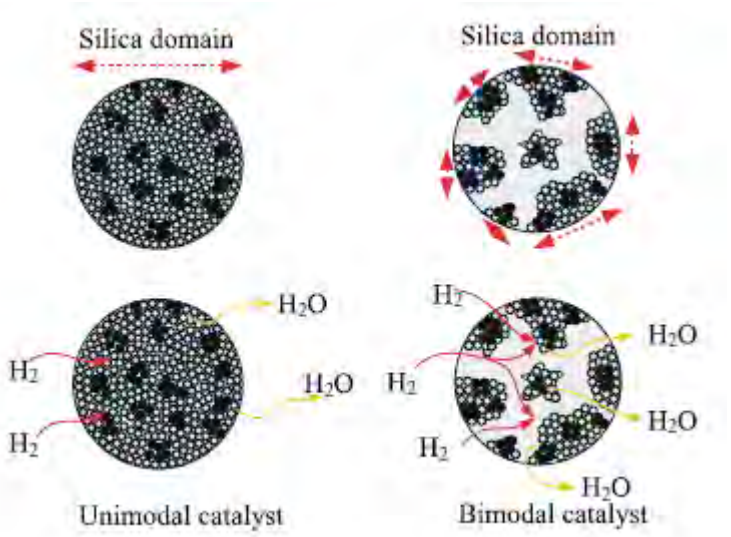

รูปที่ 14 แผนภาพแสดงโดเมนของซิลิกาที่มีรูพรุนหนึ่งขนาดและซิลิกาที่มีรูพรุนสองขนาด

4. สรุปผลการทดลอง

จากผลการทดลอง พบว่าอนุภาคโคบอลต์ออกไซด์เฉลี่ยที่โหลดบนซิลิกาที่มีรูพรุนสองขนาดมีขนาดเท่ากับ 10.6 นาโนเมตร ซึ่งใหญ่กว่าอนุภาคของโคบอลต์ออกไซด์เฉลี่ยที่โหลดบนซิลิกาที่มีรูพรุนหนึ่งขนาดอยู่เล็กน้อย (9.8 นาโนเมตร) ทั้งนี้เป็นผลเนื่องมาจากรูพรุนระดับมาโครพอร์ทำให้เกิดการรวมตัวของโคบอลต์ออกไซด์ทั้งภายในรูพรุนขนาดเล็กและรูพรุนขนาดใหญ่ซึ่งการรวมตัวที่รูพรุนขนาดใหญ่ทำให้อนุภาคโคบอลต์ออกไซด์ทีโอกาสที่จะรวมกันเป็นอนุภาคขนาดใหญ่ได้ง่ายกว่า โคบอลต์ออกไซด์ที่โหลดบนซิลิกาที่มีรูพรุนสองขนาดสามารถถูกรีดิวซ์ได้ง่ายกว่าโคบอลต์ออกไซด์ที่โหลดบนซิลิกาที่มีรูพรุนหนึ่งขนาดทั้งสองขั้นตอน (Co_3O_4 ไปเป็น CoO และ การรีดิวซ์ของ CoO ไปเป็น Co^0) ซึ่งการรีดิวซ์ได้ง่ายกว่านี้เป็นผลเนื่องมาจากลักษณะทางกายภาพของซิลิกาที่มีรูพรุนสองขนาดมีโดเมนที่สั้นกว่าทำให้การแพร่เข้า-ออกของสารโมเลกุลทำได้ง่ายกว่า

5. ข้อเสนอแนะสำหรับงานวิจัยในอนาคต

ซิลิกาที่มีรูพรุนสองขนาดสามารถช่วยเพิ่มประสิทธิภาพในการแพร่ได้เหมาะสำหรับปฏิกิริยาที่มีความต้านทานการแพร่เป็นขั้นกำหนดปฏิกิริยา โดยสามารถนำไปทดสอบเป็นตัวรองรับตัวเร่งในปฏิกิริยา ไบโอดีเซล หรือการเร่งปฏิกิริยาการผลิตดีเซลผ่านกระบวนการสังเคราะห์แบบฟิชเชอร์-โทรปช์

Keywords : ตัวเร่งปฏิกิริยาวิวิธพันธ์ ทรงกลมกลวง เมทานอล ไคโตซาน ก๊าซคาร์บอนไดออกไซด์ ซิลิกาที่มีรูพรุนสองขนาด

Output จากโครงการวิจัยที่ได้รับทุนจาก สกว.

ผลงานตีพิมพ์ในวารสารวิชาการนานาชาติ

เรื่องที่ 1

Witoon, T.*, Permsirivanich, T., Donphai, W., Jaree, A., Chareonpanich, M. CO_2 hydrogenation to methanol over Cu/ZnO nanocatalysts prepared via a chitosan-assisted co-precipitation method. *Fuel Processing Technology* **2013**, 116, 72–78. (IF 2012 = 2.816)

เรื่องที่ 2

Witoon, T.*, Permsirivanich, T., Chareonpanich, M. Chitosan-assisted combustion synthesis of CuO–ZnO nanocomposites: Effect of pH and chitosan concentration. *Ceramics International* **2013**, 39, 3371–3375. (IF 2012 = 1.789)

เรื่องที่ 3

Witoon, T.*, Chareonpanich, M., Limtrakul, J. Effect of bimodal porous silica on particle size and reducibility of cobalt oxide. *Journal of Porous Materials* **2013**, 20, 481–488. (IF 2012 = 1.348)

เรื่องที่ 4

Witoon, T.* Polyethyleneimine-loaded bimodal porous silica as low-cost and high-capacity sorbent for CO_2 capture. *Materials Chemistry and Physics* **2012**, 137, 235–245. (IF 2012 = 2.072)

เรื่องที่ 5

Witoon, T.*, Chareonpanich, M. Interaction of chitosan with tetraethyl orthosilicate on the formation of silica nanoparticles: effect of pH and chitosan concentration. *Ceramics International* **2012**, 38, 5999–6007. (IF 2012 = 1.789)

เรื่องที่ 6

Witoon, T.* Characterization of calcium oxide derived from waste eggshell and its application as CO_2 sorbent. *Ceramics International* **2011**, 37, 3291–3298. (IF 2012 = 1.789)

เรื่องที่ 7

Witoon, T.*, Tepsarn, S., Kittipokon, P., Embley, B., Chareonpanich, M. Effect of pH and chitosan concentration on precipitation and morphology of hierarchical porous silica. *Journal of Non-Crystallite Solids* **2011**, 357, 3513–3519. (IF 2012 = 1.597)

ภาคผนวก

Fuel Processing Technology 116 (2013) 72–78

Contents lists available at SciVerse ScienceDirect

Fuel Processing Technology

journal homepage: www.elsevier.com/locate/fuproc

CO_2 hydrogenation to methanol over Cu/ZnO nanocatalysts prepared via a chitosan-assisted co-precipitation method

Thongthai Witoon [a,b,c,*], Tinnavat Permsirivanich [a], Waleeporn Donphai [a], Attasak Jaree [a], Metta Chareonpanich [a,b,c]

[a] National Center of Excellence for Petroleum, Petrochemicals and Advance Material, Department of Chemical Engineering, Faculty of Engineering, Kasetsart University, Bangkok 10900, Thailand
[b] Center for Advanced Studies in Nanotechnology and Its Applications in Chemical Food and Agricultural Industries, Kasetsart University, Bangkok 10900, Thailand
[c] NANOTEC-KU-Center of Excellence on Nanoscale Materials Design for Green Nanotechnology, Kasetsart University, Bangkok 10900, Thailand

ARTICLE INFO

Article history:
Received 7 November 2012
Received in revised form 17 April 2013
Accepted 24 April 2013
Available online xxxx

Keywords:
Heterogeneous catalysis
Hollow sphere
Chitosan
Carbon dioxide
Nanomaterials

ABSTRACT

In this study, CuO–ZnO nanocomposites were prepared by chitosan-assisted co-precipitation method and performed as catalyst for CO_2 hydrogenation to methanol. Effects of chitosan concentration on the physico-chemical properties of the nanocomposites as well as the catalytic activity have been investigated. The obtained catalysts were characterized by means of scanning electron microscopy, X-ray diffraction, N_2 adsorption–desorption, N_2O chemisorption and temperature-programmed reduction. Chitosan was found to act not only as a coordination compound to produce a homogeneous combination of CuO–ZnO nanocomposite, but also as a soft template for the formation of hollow nanospheres. The CuO and ZnO crystallite sizes of the hollow nanospheres were found to be 11.5 and 18.8 nm, respectively, which were smaller than those of other catalysts. The increase of chitosan concentration caused a change in catalyst morphology and a reduction in BET surface area as well as metallic copper surface area, but still higher than those of the unmodified catalyst. The catalysts prepared by using chitosan as precipitating agent exhibited a higher space time yield of methanol than the unmodified catalyst, which was attributed to a synergetic effect of the CuO nanoparticle incorporated in the CuO–ZnO nanocatalyst. However, when the reaction temperature was increased up to 533 K, a decline in the space time yield of methanol was observed for the catalysts prepared at high chitosan concentration.

1. Introduction

Carbon dioxide (CO_2) is considered to be the major cause of climate change, because of its greenhouse properties and continuous accumulation in the atmosphere. A reduction of CO_2 emission can potentially occur as a result of increased energy efficiency, substitution of non-carbon fuels, or by carbon capture and storage (CCS) [1]. In addition to permanent storage, the utilization of CO_2 has received increased global attention. There are essentially two major pathways for utilizing CO_2 [2,3]: 1) as a feedstock for fuels and various chemicals productions, and 2) as a solvent or working fluid. Although the utilization of CO_2 will not solve the atmospheric CO_2 accumulation as well as the global warming problems, it might contribute to such issues by reducing the volume of CO_2 produced via the use of fuels and chemicals [4].

CO_2 has been already used in chemical industry for synthesis of several organic compounds, such as urea, salicyclic acid, methanol, cyclic carbonates, and poly carbonate-based plastics [2]. Among them, methanol is one of the most versatile compounds developed as it can be used as a feedstock for chemicals, such as formaldehyde, acetic acid and biodiesel [5–8]. All of these derivative chemicals would be considered completely renewable. Moreover, methanol can be looked upon as a way of converting hydrogen into an energy carrier that can be more conveniently stored and transported.

Cu/ZnO based catalysts are known to be active and selective for the synthesis of methanol from CO_2 hydrogenation. Co-precipitation technique, which usually employs alkaline carbonate as a precipitating agent, is the most common commercially used to prepare Cu/ZnO based catalysts. However, this technique has some disadvantages since the precipitation process is lengthy as more than 12 h are essentially required for ageing step [9–12]. Moreover, the residual alkaline content in the catalyst is found to have a negative effect on the synthesis of methanol from CO_2 hydrogenation [12]. Therefore the large volume of water is needed to leach the alkaline content to acceptable level, leading to a costly process.

Naturally abundant biopolymers such as chitin and chitosan are widely used to remove heavy metal ions such as copper, zinc, nickel and lead from wastewater [13,14]. Thus it might be possible to use

* Corresponding author at: National Center of Excellence for Petroleum, Petrochemicals and Advance Material, Department of Chemical Engineering, Faculty of Engineering, Kasetsart University, Bangkok 10900, Thailand. Tel.: +66 2579 2083; fax: +66 2561 4621.
E-mail address: fengttwi@ku.ac.th (T. Witoon).

0378-3820/$ – see front matter © 2013 Elsevier B.V. All rights reserved.
http://dx.doi.org/10.1016/j.fuproc.2013.04.024

them as precipitating agent instead of alkaline carbonate solution. Herein, we report a simple, green and efficient method for preparation of CuO–ZnO nanocomposites by facile chitosan-assisted co-precipitation method, and their catalytic performances for the methanol synthesis from CO_2 hydrogenation have been investigated at different reaction temperatures.

2. Experimental

2.1. Preparation of CuO–ZnO nanocomposites

The starting materials were $Cu(NO_3)_2 \cdot 3H_2O$, $Zn(NO_3)_2 \cdot 6H_2O$, acetic acid, ammonium hydroxide and chitosan. Chitosan with 80% deacetylation was purchased from Eland Corporation. The weight average molar mass of chitosan (M_w = 290,000 Da) was determined by Gel Permeation Chromatography (GPC, Water 600E) using 0.5 M acetic acid and 0.5 M sodium acetate as an eluent at a flow rate of 0.6 mL/min. Pullulans (M_w: 5900–708,000 Da) were used as standard samples to calibrate the column.

In a typical synthesis process, chitosan was dissolved overnight in 100 mL of 1% v/v acetic acid in deionized water at room temperature, agitated with a magnetic stirrer. Subsequently, 3.749 g $Cu(NO_3)_2 \cdot 3H_2O$ and 4.616 g $Zn(NO_3)_2 \cdot 6H_2O$ (mole ratio of Cu/Zn = 1/1) were added into the chitosan solution. Then the pH value of the mixture was quickly adjusted to 7 by the addition of aqueous NH_4OH. The resulting mixture was stirred at 333 K for 6 h to ensure the chitosan completely chelating with the metal ions. Subsequently, the mixture was heated at 353 K to evaporate the solvent. The precipitate was then dried in an oven at 393 K for 24 h. Finally, the product was calcined in a furnace under air atmosphere at 723 K for 2 h with a heating rate of 2 K/min. In comparison with the traditional co-precipitation method [9–12], chitosan assisted co-precipitation method provided a shorter and low-cost process because there is no further requirement for ageing and washing steps. In order to investigate the effect of the chitosan on the physico–chemical properties of CuO–ZnO catalysts, the chitosan concentration was varied from 0 to 0.0045 g mL^{-1}. The obtained products are denoted as CZ-*x*; where *x* is a chitosan concentration of 0, 0.0015, 0.0030 and 0.0045 g mL^{-1}.

2.2. Characterization of CuO–ZnO nanocatalysts

The surface morphology and surface compositions of the samples were examined with a field emission scanning electron microscopy (FE-SEM: Hitachi-S4700) equipped with energy-dispersive X-ray spectroscopy (EDS). The samples were sputter coated with gold prior to examination.

X-ray diffraction (XRD) patterns of the catalysts were done on a diffractometer (Bruker D8 Advance) using Cu-K_α radiation. The measurements were made at room temperature at a range of 20°–90° on 2θ with a step size of 0.05°. The diffraction patterns were analyzed using the Joint Committee on Powder Diffraction Standards (JCPDS). CuO and ZnO crystallite sizes were calculated by means of the Scherrer Eq. as shown below:

$$d = \frac{0.89\lambda}{B\cos\theta} \times \frac{180^o}{\pi} \quad (1)$$

where d denotes the mean crystallite size, λ is the X-ray wave length (1.54 Å), and B is the full width half maximum (FWHM) of the peak.

Nitrogen sorption isotherms of the catalysts were measured at 77 K with a Quantachrome Autosorb-1C instrument. Prior to sorption measurements, the products were degassed at 473 K for 12 h. The pore size distribution was calculated by using the Barrett–Joyner–Halenda (BJH) methods. The specific pore volumes were measured at a relative pressure P/P_0 of 0.995. The total surface area (S_{BET}) of the catalysts was derived by using the BET (Brunauer–Emmert–Teller) analysis in the relative pressure range between P/P_0 = 0.05 and 0.3. The copper (Cu^0) surface area of the catalysts was obtained by N_2O-titration measurements as described elsewhere [15].

The extent of CuO reduction in hydrogen was measured using a DSC-TGA 2960 thermal analyzer. The samples (10 mg) were placed in an alumina pan and were dehydrated in dry air at 473 K for 1 h. Then the samples were cooled down to room temperature. Subsequently, the samples were heated in a flow of hydrogen (100 mL/min) from room temperature to 673 K with a heating rate of 5 K/min. TGA technique used in the present work to measure extent of CuO reduction was successfully tested for supported $CuO/ZnO/Al_2O_3$, CuO/CeO_2, CuO/ZrO_2 and $CuO/ZnO/ZrO_2$ catalysts [16–18].

2.3. Catalytic activity test

CO_2 hydrogenation was carried out in a fixed–bed stainless steel reactor (7.75 mm inner diameter). In a typical experiment, 0.5 g fresh catalyst was diluted with 0.5 g inert silica sand (75–150 μm). The catalyst was reduced *in situ* at atmospheric pressure in pure H_2 flow (80 mL/min) at 623 K for 2 h with a heating rate of 5 K/min. After reduction, the temperature was decreased to 433 K under flow of N_2, and subsequently a flow of CO_2 and H_2 mixture (CO_2:H_2 molar ratio of 1:3) was fed through the reactor. The feed flow rate was set at 4800 $mL/g_{cat} \cdot h$. The reactor pressure was slowly raised to 2.0 MPa and the reactor was heated to a given temperature (453, 473, 493, 513 and 533 K). The effluent gaseous products were analyzed by using gas chromatography. Analysis of H_2, CO, CO_2, N_2 and H_2O was performed using GC–2014 gas chromatography equipped with a thermal conductivity detector (TCD) and a Unibead-C column. Hydrocarbon products were analyzed by using GC 8A equipped with a flame ionization detector (FID) detector and a Porapak-Q column.

3. Results and discussion

The apparent morphologies of the CuO–ZnO nanocomposites prepared at different chitosan concentrations examined by means of a SEM are shown in Fig. 1. Without the addition of chitosan (Fig. 1a–c), an aggregate of two different morphologies including a plate-like structure and an irregular spherical shape was observed. The size of the plate-like structure was found to be approximately 300–500 nm which was larger than that of the irregular spherical shape (100–300 nm). The EDX results revealed that the main component of the plate-like structure was ZnO whereas that of the irregular spherical shape was CuO, implying that the CuO and ZnO products occurred separately. Once 0.0015 g mL^{-1} chitosan was used (Fig. 1d–f), individual hollow spheres with an average size of approximately 300–500 nm were formed. An enlarged SEM image (Fig. 1f) from the surface of the hollow nanospheres clearly revealed that the shell of the hollow nanospheres was composed of numerous nanocrystals. With increasing the chitosan concentration to 0.0030 g mL^{-1} (Fig. 1 g–i), the size of the hollow nanospheres was found to decrease when compared to that of the product prepared at lower amount of chitosan (CZ-0.0015). Moreover, the hollow spheres were connected together and formed a loose network. With a yet higher chitosan concentration (Fig. 1j–l), the hollow spheres were no longer observed and instead an agglomerate of nanoparticles was obtained. Based on the results of the EDX analysis on several spots, the ratio of Cu/Zn of the catalyst CZ-0.0015 was found to be 0.93 which was indicative for a uniform distribution of CuO and ZnO in the structure of the catalysts. However, the increase of chitosan concentration caused a decrease of the ratio of Cu/Zn to be 0.85 and 0.75 for the catalysts CZ-0.0030 and CZ-0.0045, respectively.

The XRD patterns of the products synthesized at different chitosan concentrations are shown in Fig. 2. The major peaks at 2θ values of 32.54°, 35.52°, 38.81°, 48.56° and 61.50° which are indexed to the

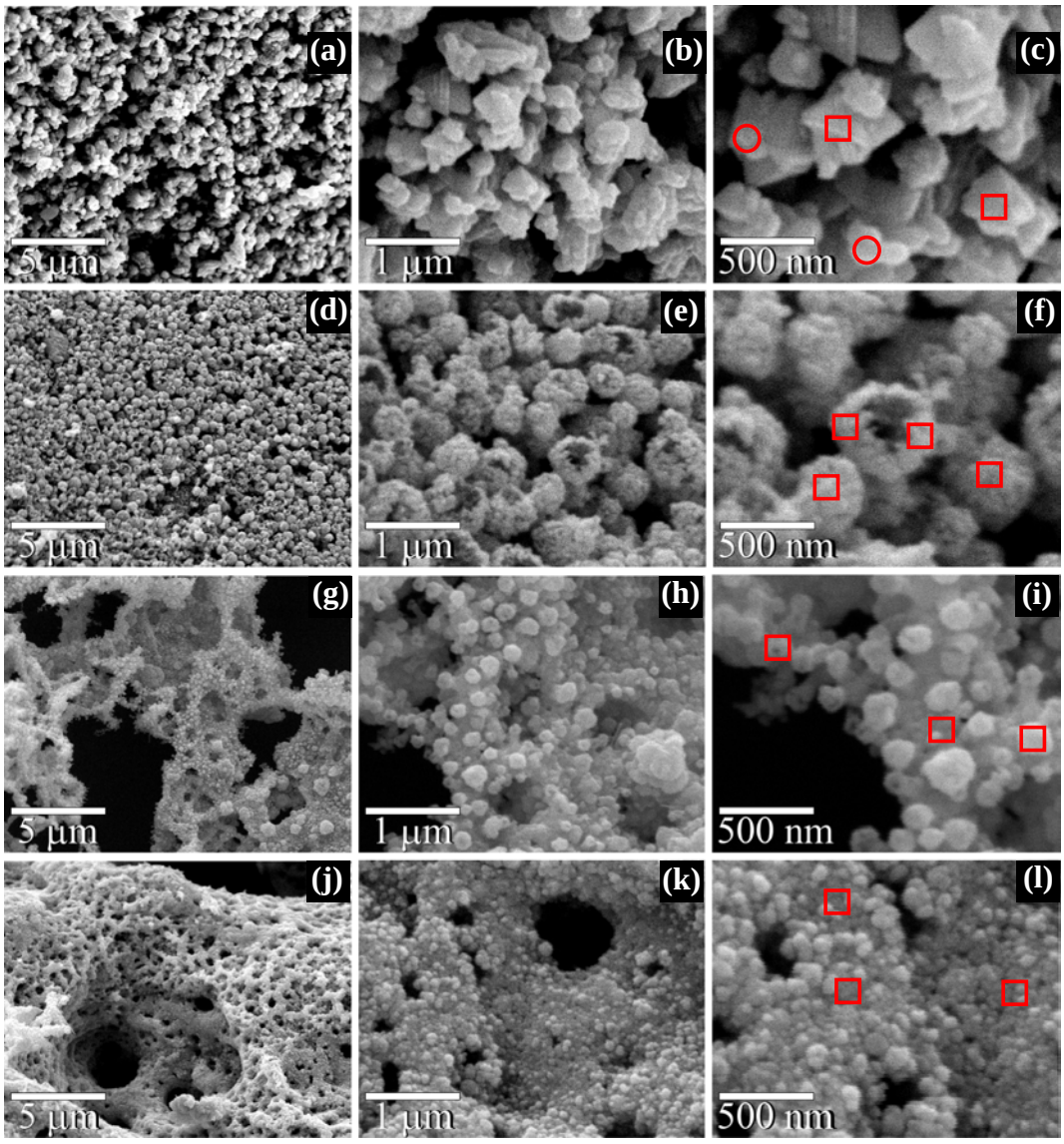

Fig. 1. SEM images at different magnifications of all catalysts: (a–c) CZ-0, (d–f) CZ-0.0015, (g–i) CZ-0.0030 and (i–l) CZ-0.0045.

CuO diffractions of (110), (002), (111), (202) and (113) planes, respectively are consistent with the JCPDS 05-0661 and ascribed to the monoclinic CuO crystal phase. The other diffraction peaks matched the standard data for a heaxagonal wurtzite ZnO (JCPDS 36–1451). It can be seen that the XRD pattern of all products

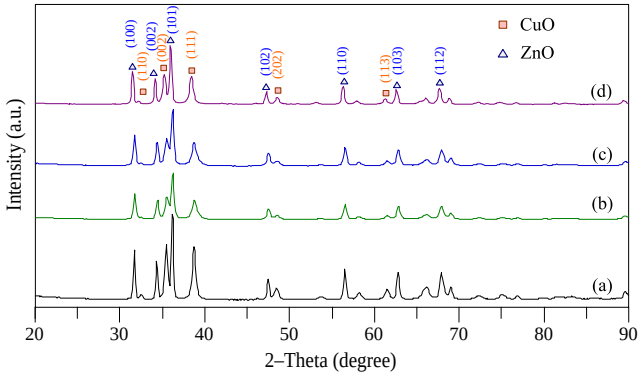

Fig. 2. XRD patterns of all catalysts: (a) CZ-0, (b) CZ-0.0015, (c) CZ-0.0030 and (d) CZ-0.0045.

appeared at the identical 2θ angles, indicating that the chitosan molecules did not alter the crystalline phases of the products. The most intense peak of CuO and ZnO centered at 35.52° and 36.25°, respectively is used to calculate the average crystallite size with the Scherrer Equation. Note that the similar trends were obtained when other peaks were applied.

As shown in Table 1, the CuO and ZnO crystallite sizes of the unmodified catalyst were found to be 20.4 and 29.1 nm, respectively. With the use of chitosan, both the CuO and ZnO crystallite sizes were significantly decreased. At low chitosan concentration (CZ-0.0015), the CuO and ZnO crystallite sizes were found to be reduced by 43.6% and 35.4%, respectively, when compared to their original size. However, the percent reduction in crystallite size was found to be decreased with increasing the chitosan concentration. At high chitosan concentration (CZ-0.0045), only 20.6% and 10.0% of size reduction of CuO and ZnO could be achieved respectively. Several literatures reported that chitosan could effectively chelate heavy metal ions because the active sites including the amino ($-NH_2$) and/or hydroxyl ($-OH$) groups along the backbone chains of chitosan molecules served as coordination sites [19–21]. These interactions might be strong enough to restrict mobility of metal species, and therefore limited the available number of metal species to form the larger crystal. However,

Table 1
Surface compositions reported as average value and metal oxides crystallite size.

Samples [a]	Position	Cu/Zn	Average metal oxides crystallite size (nm)	
			CuO [b]	ZnO [b]
CZ-0	Rectangular	0.14	20.4	29.1
	Circle	2.72		
CZ-0.0015	Rectangular	0.93	11.5	18.8
CZ-0.0030	Rectangular	0.85	13.5	23.4
CZ-0.0045	Rectangular	0.75	16.2	26.2

[a] The samples are denoted as CZ-*x* where *x* is the chitosan concentration in g mL^{-1}.
[b] The crystallite sizes for CuO and ZnO were calculated with the Scherrer equation using the most intense peak centered at 35.52° and 36.25°, respectively.

the dense chitosan network was possibly formed at high chitosan concentration. The metal species hardly penetrated within the dense chitosan network, and adsorbed randomly on the external chitosan network. Therefore the active sites were reduced and the chitosan molecule was inefficient to prevent the crystal growth for such condition. Note that chitosan molecule would prefer to control the crystal growth of CuO rather than that of ZnO. This is likely because the adsorption rate of copper species with the chitosan molecules was faster than that of zinc species [19–21], resulting in a larger amount of zinc species to be remained in the solution which could promote the formation of a larger crystal.

As the characteristics of the pore structure of CuO–ZnO nanocomposites could affect the transport of reactants and need to be therefore thoroughly investigated. The pore characteristics of all samples measured by N_2-physisorption are shown in Fig. 3 and their textural properties inclusive the BET surface area and total pore volume are listed in Table 2. As shown in Fig. 3a, the isotherm of the sample prepared without the chitosan addition was found to be almost parallel to the x-axis, an indication of non-porous materials. The quite low and multimodal peak intensities suggested non-uniform porosity as a result of mixed mesopores and macropores (Fig. 3e). With the chitosan addition, the type II isotherm was found (Fig. 3b–d), which suggests the existence of macroporous structure in the catalysts. The peak intensity of these samples was found to be sharp and located in the macropore region. However, the pore size was found to be dissimilar and strongly depend on the chitosan concentration. At 0.0015 g mL^{-1} chitosan (Fig. 3f), the bimodal pores centered at 42 and 215 nm were observed, which could be related to the aggregate of nanoparticles and the opening part of hollow sphere as shown by SEM image (Fig. 1f), respectively. With further increasing chitosan concentration to 0.0030 and

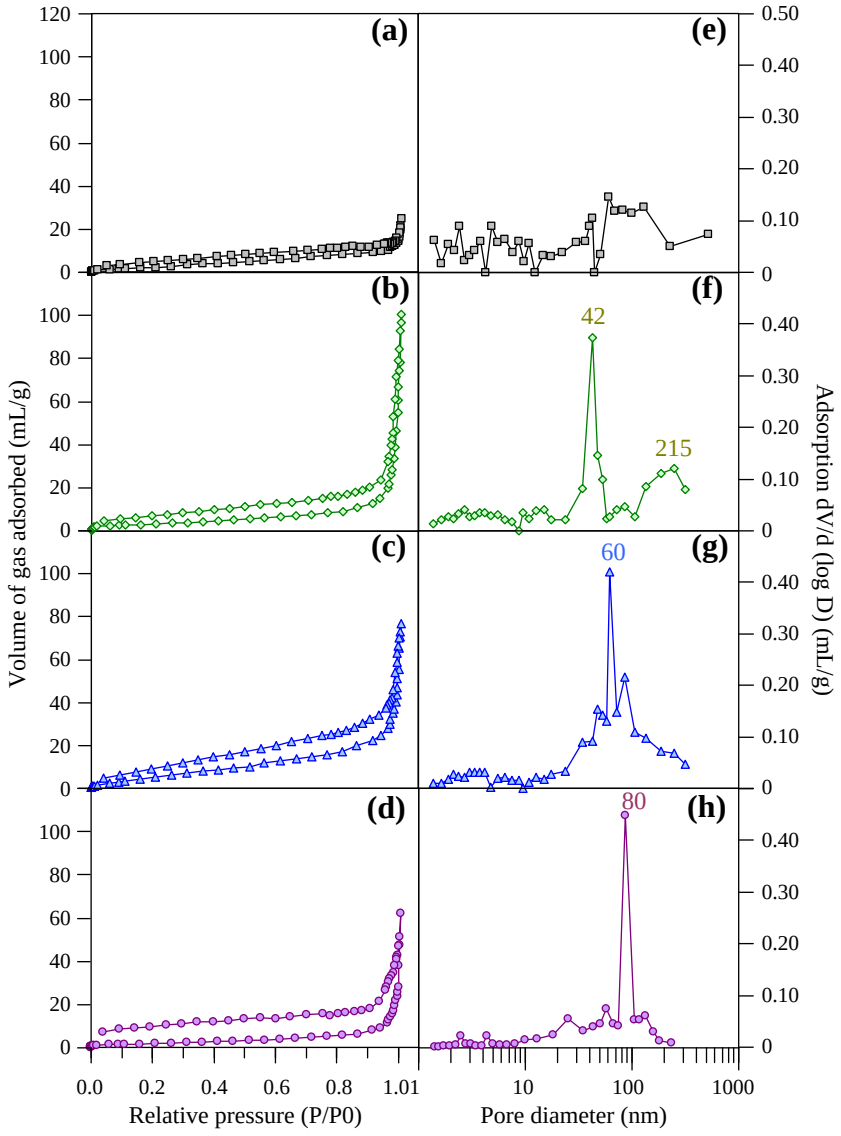

Fig. 3. N_2-sorption isotherms and pore size distributions of all catalysts: (a and e) CZ-0, (b and f) CZ-0.0015, (c and g) CZ-0.0030 and (e and h) CZ-0.0045.

Table 2
Average pore size, BET surface area, total pore volume and copper surface area of the catalysts.

Catalysts	Average pore diameter (nm)	BET surface area (m^2/g)	Total pore volume (mL/g)	Copper surface area (m^2/g)
CZ-0	–	14.5	0.06	5.5
CZ-0.0015	42 and 215	46.2	0.16	15.4
CZ-0.0030	60	34.5	0.13	12.5
CZ-0.0045	80	28.4	0.11	8.4

0.0045 g mL^{-1} (Fig. 3 g and h), the large pore size (215 nm) was disappear and the smaller pore size was established to have shifted to 60 and 80 nm, respectively.

The BET surface area and total pore volume of the sample prepared without the chitosan addition were found to be 14.5 m^2/g and 0.06 cm^3/g, respectively. When the chitosan was used, the increase in the BET surface and the total pore volume was observed. The highest BET surface area (46.2 m^2/g) and the largest total pore volume (0.16 cm^3/g) were achieved for the catalyst CZ-0.0015. After this chitosan concentration, the BET surface area and the total pore volume were found to slightly decrease but still higher than that of the unmodified catalyst.

Fig. 4 shows the reduction profiles of all catalysts. The catalyst CZ-0 displays two main exothermic peaks at the maximum temperatures of 465 K and 471 K, a suggestion of the presence of two reducible copper species. The peak at lower temperature can be ascribed to the reduction of highly dispersed CuO species [22] while the peak at higher temperature can be attributed to the reduction of bulk-like CuO phases [22]. This result revealed that most of copper species were precipitated as separate phase and a small percent of CuO formed in the CuO–ZnO composite. With small amount of chitosan addition (0.0015 g mL^{-1}), only one sharp peak appeared at 461 K is observed, which is an indication of the homogeneous dispersion of CuO phase in the CuO–ZnO composite. With further increase the amount of chitosan to 0.0030 and 0.0045 g mL^{-1}, the double peak appears again. However, the maximum peaks are established to have shifted toward lower temperature compared to those of the unmodified catalyst, which suggests a smaller CuO crystallite size to be reduced easier than a larger one. Note that a larger CuO crystallite size of the CZ-0.0030 and CZ-0.0045 catalysts can be reduced at lower temperature compared to the smaller CuO crystallite size of the CZ-0.0015 catalyst. This result may be due to the fact that the CZ-0.0015 catalyst is a homogeneous mixture of CuO and ZnO as examined by the SEM-EDX analysis (Cu/Zn ratio = 0.93). In other words, CuO nanoparticles could be adjacently formed with ZnO nanoparticles leading to a strong interaction, which possibly make it more difficult to be reduced when compared to the reduction of aggregated CuO nanoparticles.

As the active form of copper-based catalyst in the methanol synthesis is mainly metallic surface of copper (Cu^0), the reduction of copper oxide species is essentially performed to obtain the active phase. As shown in Table 2, the metallic copper surface area of the catalysts follows the similar trend of the BET surface area. This result was in good agreement with the reduction behavior and SEM analysis that the catalyst CZ-0.0015 exhibited the homogeneous distribution of CuO in the CuO–ZnO composite.

Effects of reaction temperature on the activity of the CuO–ZnO nanocomposite in CO_2 hydrogenation to methanol are shown in Fig. 5. With increasing reaction temperature from 473 to 513 K, CO_2 conversion of all catalysts was found to be increased with no sign of

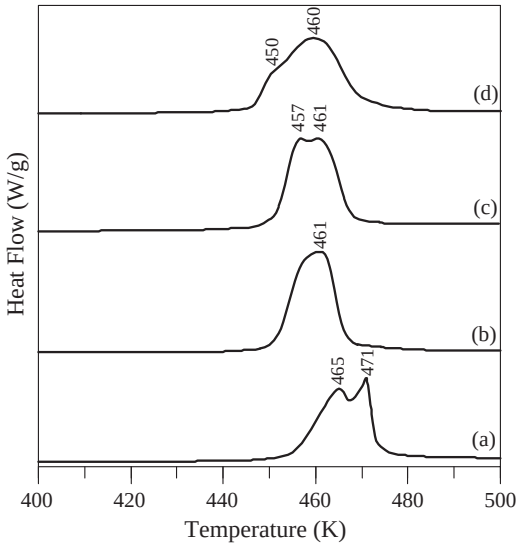

Fig. 4. TPR profiles of all catalysts: (a) CZ-0, (b) CZ-0.0015, (c) CZ-0.0030 and (d) CZ-0.0045.

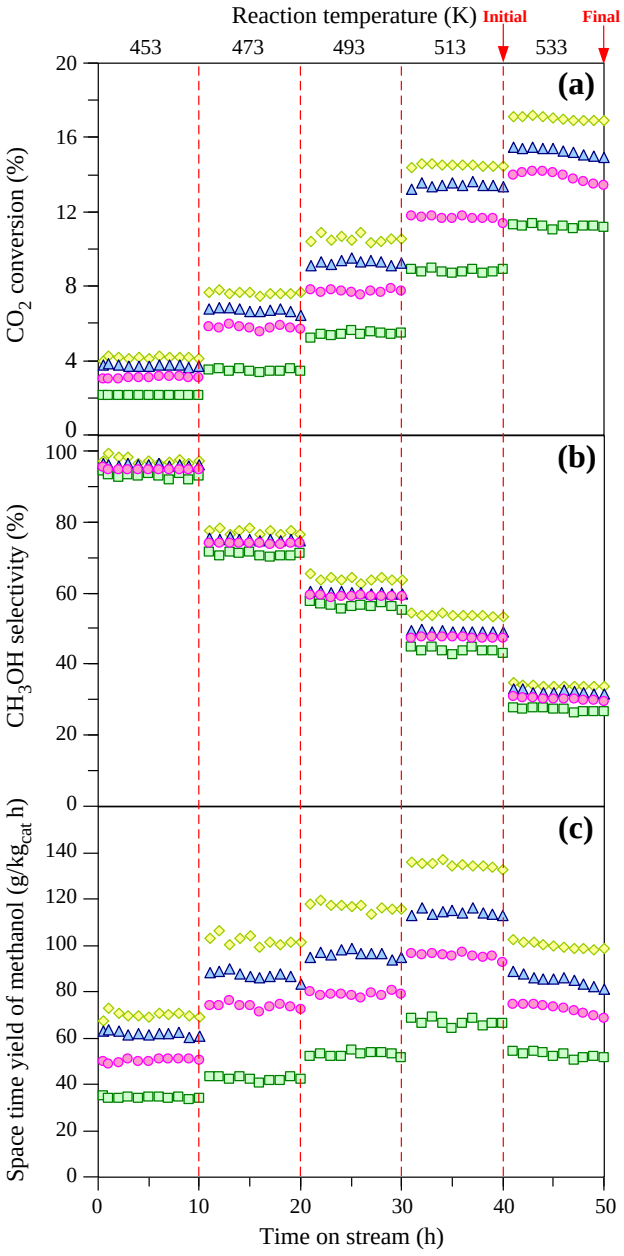

Fig. 5. CO_2 conversion (a), CH_3OH selectivity (b) and STY of methanol (c) of □ CZ-0, ◇ CZ-0.0015, △ CZ-0.0030 and ○ CZ-0.0045 at different reaction temperatures.

deactivation and the catalyst prepared via chitosan-assisted co-precipitation method was found to be more active than that prepared without the chitosan. At 533 K, CO_2 conversion of all catalysts still increased, however, the sign of deactivation was observed. When compared to the initial CO_2 conversion at 533 K, the CO_2 conversion after 10 h was found to decrease by 1.32%, 1.23%, 3.56% and 4.59% for the CZ-0, CZ-0.0015, CZ-0.0030 and CZ-0.0045 catalysts, respectively.

The methanol selectivity of all catalysts was found to decrease with the increase of reaction temperature due to a thermodynamic equilibrium of methanol and a parallel increase in the participation of the endothermic reverse-water-gas-shifted reaction. The space time yield (STY) of methanol was found to increase with the increase of reaction temperature from 453 to 513 K due to the increase of CO_2 conversion and relatively high methanol selectivity. The highest STY of methanol was found (at 513 K) to be 135 g/kg_{cat} h for the catalyst CZ-0.0015 which was established to be 190% more effective than that of the unmodified catalyst. The STY of methanol operated at 533 K was found to be lower than that at 493–513 K due to a dramatically decrease of methanol selectivity. Again, compared to the initial STY of methanol at 533 K, the STY of methanol after 10 h was found to decrease by 4.84%, 4.05%, 8.15% and 8.00% the CZ-0, CZ-0.0015, CZ-0.0030 and CZ-0.0045 catalysts, respectively. This indicates that the deactivation of the catalysts prepared at high chitosan concentration (CZ-0.0030 and CZ-0.0045) is easier than that of the other catalysts (CZ-0 and CZ-0.0015). This is likely due to the fact that the larger copper crystallites can remain in the metallic form, while the small copper crystallites are possibly oxidized to Cu_2O or CuO [23]. In addition, this behavior can be a thermally induced deactivation caused by a loss of surface area of copper. Note that chitosan-assisted co-precipitation can enhance the metallic copper surface area as CuO can be better dispersed on the surface of ZnO. However, for the CZ-0.0030 and CZ-0.0045 catalysts, the surface of ZnO cannot prevent an aggregate of copper nanoparticles from a sintering process. This is likely that the interaction between CuO and ZnO of those catalysts was relatively weak as shown in Fig. 4. Therefore mobility of CuO can occur and CuO nanoparticles may be aggregated to form the larger one when the reaction temperature was increased.

The effect of metallic copper surface area on the activity of synthesis of methanol from CO_2 hydrogenation over all catalysts was investigated at different reaction temperatures and the results are shown in Fig. 6. It can be clearly seen that both CO_2 conversion (Fig. 6a) and STY of methanol (Fig. 6b) increased with the increase of the metallic copper surface area. However, only the catalysts prepared with the chitosan addition (CZ-0.0015, CZ-0.0030, and CZ-0.0045) show a linear relationship. Both CO_2 conversion and space time yield of methanol of the unmodified catalyst (S_{Cu} = 5.5 m^2/g) obviously deviated from the linear trend of variation of the metallic copper surface area of 8.4–15.4 m^2/g. Several literatures reported that the catalytic activity of synthesis of methanol from CO_2 hydrogenation not only depended on the metallic copper surface area but also a synergy effect between Cu and ZnO [24–26]. In contrast to the catalysts prepared with the chitosan addition, the CuO and ZnO of the unmodified catalyst precipitated separately with a low degree of combination, and therefore the deviation of the catalytic activity of the unmodified catalyst could be due to a lower synergy effect between Cu and ZnO.

4. Conclusion

In summary, the use of chitosan as precipitating agent was found to significantly influence on the physicochemical properties of the CuO–ZnO nanocomposites as well as catalytic performance for CO_2 hydrogenation to methanol. Hollow CuO–ZnO nanospheres with the homogeneous distribution of CuO could be formed by adding a small amount of chitosan (CZ-0.0015). When the chitosan concentration was increased (CZ-0.0030 and CZ-0.0045), the hollow structure was no longer observed and instead an aggregate of CuO–ZnO nanoparticles was obtained. The CuO and ZnO crystallite sizes were found to decrease when compared to the unmodified catalyst. However, at high chitosan concentration, the CuO nanoparticles tended to aggregate themselves, resulting in a reduction of copper surface area. The CO_2 conversion and the space time yield of methanol of the catalysts prepared with chitosan were found to exceed those of the unmodified catalyst. However, at high reaction temperature, a sign of deactivation was observed for the catalysts prepared with high chitosan concentration (CZ-0.0030 and CZ-0.0045) which was possibly due to the weak interaction between CuO and ZnO.

Acknowledgements

This work was financially supported by the Thailand Research Fund (Grant No. MRG5480196), the National Center of Excellence for Petroleum, Petrochemical and Advanced Materials (NCE-PPAM), and the National Research University Project of Thailand (NRU). The authors would like to thank the partial support from the Nanotechnology Center (NANOTEC), NSTDA, Ministry of Science and Technology, Thailand through its program of Center of Excellence Network and the Kasetsart University Research and Development Institute (KURDI).

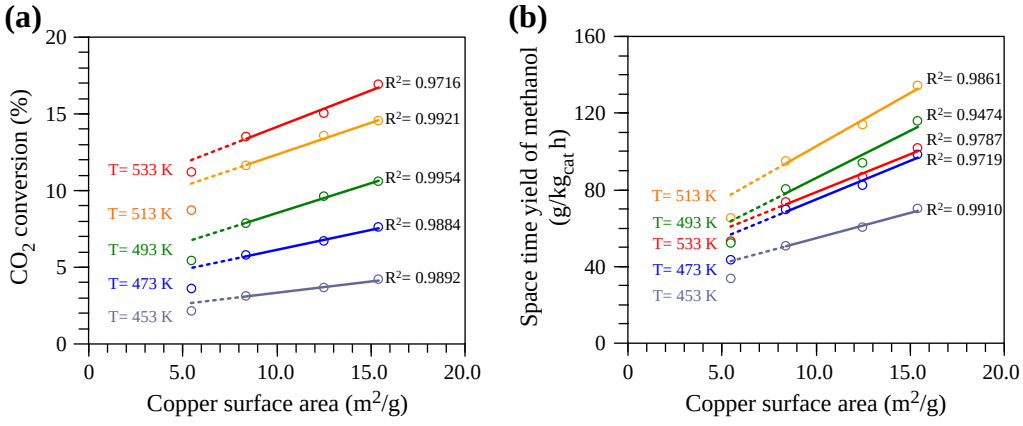

Fig. 6. CO_2 conversion (a) and STY of methanol (b) as a function of metallic copper surface area at different reaction temperatures.

References

[1] A.A. Olajire, CO_2 capture and separation technologies for end-of-pipe applications – A review, Energy 35 (2010) 2610–2628.
[2] M. Aresta, Carbon dioxide: utilization options to reduce its accumulation in the atmosphere, in carbon dioxide as chemical feedstock, in: M. Aresta (Ed.), Wiley-VCH, Weinheim, Germany, 2010, http://dx.doi.org/10.1002/9783527629916.ch1.
[3] G. Centi, S. Perathoner, Opportunities and prospects in the chemical recycling of carbon dioxide to fuels, Catalysis Today 148 (2009) 191–205.
[4] M. Aresta, Carbon dioxide capture and storage, in: M. Maroto-Valer (Ed.), Woodhead Publishing Limited, Abington Hall, Granta Park, Cambridge, CB216AH, UK, 2009.
[5] R.H. Borgwardt, Methanol production from biomass and natural gas as transportation fuel, Industrial and Engineering Chemistry Research 37 (1998) 3760–3767.
[6] X. Zhang, L. Zhong, Q. Guo, H. Fan, H. Zheng, K. Xie, Influence of the calcination on the activity and stability of the $Cu/ZnO/Al_2O_3$ catalyst in liquid phase methanol synthesis, Fuel 89 (2010) 1348–1352.
[7] L. Shi, K. Tao, R. Yang, F. Meng, C. Xing, N. Tsubaki, Study on the preparation of Cu/ZnO catalyst by sol–gel auto-combustion method and its application for low-temperature methanol synthesis, Applied Catalysis A: General 401 (2011) 46–55.
[8] E. Samei, M. Taghizadeh, M. Bahmani, Enhancement of stability and activity of $Cu/ZnO/Al_2O_3$ catalysts by colloidal silica and metal oxides additives for methanol synthesis from a CO_2-rich feed, Fuel Processing Technology 92 (2011) 1164–1168.
[9] F. Bimbela, D. Chen, J. Ruiz, L. García, J. Arauzo, Ni/Al coprecipitated catalysts modified with magnesium and copper for the catalytic steam reforming of model compounds from biomass pyrolysis liquids, Applied Catalysis B: Environmental 119–120 (2012) 1–12.
[10] S.-I. Fujita, S. Moribe, Y. Kanamori, M. Kakudate, N. Takezawa, Preparation of a coprecipitated Cu/ZnO catalyst for the methanol synthesis from CO_2—effects of the calcination and reduction conditions on the catalytic performance, Applied Catalysis A: General 207 (2001) 121–128.
[11] E.F. López, V.S. Escribano, C. Resini, J.M. Gallardo-Amores, G. Busca, A study of coprecipitated Mn-Zr oxides and their behaviour as oxidation catalysts, Applied Catalysis B: Environmental 29 (2001) 251–261.
[12] R. Raudaskoski, M.V. Niemelä, R.L. Keiski, The effect of ageing time on co-precipitated $Cu/ZnO/ZrO_2$ catalysts used in methanol synthesis from CO_2 and H_2, Topics in Catalysis 45 (2007) 57–60.
[13] C.-Y. Chen, C.-Y. Yang, A.-H. Chen, Biosorption of Cu(II), Zn(II), Ni(II) and Pb(II) ions by cross-linked metal-imprinted chitosans with epichlorohydrin, Journal of Environmental Management 92 (2011) 796–802.
[14] R.-S. Juang, H.-J. Shao, Effect of pH on competitive adsorption of Cu(II), Ni(II), and Zn(II) from water onto chitosan beads, Adsorption 8 (2002) 71–78.
[15] F. Arena, K. Barbera, G. Italiano, G. Bonura, L. Spadaro, F. Frusteri, Synthesis, characterization and activity pattern of $Cu-ZnO/ZrO_2$ catalysts in the hydrogenation of carbon dioxide to methanol, Journal of Catalysis 249 (2007) 185–194.
[16] L. Kundakovic, M. Flytzani–Stephanopoulos, Reduction characteristics of copper oxide in cerium and zirconium oxide systems, Applied Catalysis A: General 171 (1998) 13–29.
[17] W. Ning, H. Shen, H. Liu, Study of the effect of preparation method on CuO–ZnO–Al_2O_3 catalyst, Applied Catalysis A: General 211 (2001) 153–157.
[18] P.H. Matter, U.S. Ozkan, Effect of pretreatment conditions on Cu/Zn/Zr-based catalysts for the steam reforming of methanol to H_2, Journal of Catalysis 234 (2005) 463–475.
[19] D. Kołodyńska, Chitosan as an effective low-cost sorbent of heavy metal complexes with the polyaspartic acid, Chemical Engineering Journal 173 (2011) 520–529.
[20] M. Monier, Adsorption of Hg^{2+}, Cu^{2+}, Zn^{2+} ions from aqueous solution using formaldehyde cross-linked modified chitosan-thioglyceraldehyde Schiff's base, International Journal of Biological Macromolecules 50 (2012) 773–781.
[21] R.-S. Juang, H.-J. Shao, A simplified equilibrium model for sorption of heavy metal ions from aqueous solutions on chitosan, Water Research 36 (2002) 2999–3008.
[22] Y. Zhang, J. Fei, Y. Yu, X. Zheng, Methanol synthesis from CO_2 hydrogenation over Cu based catalyst supported on zirconia modified γ-Al_2O_3, Energy Conversionand Management 47 (2006) 3360–3367.
[23] J. Sloczyński, R. Grabowski, P. Olszewski, A. Kozlowska, J. Stoch, M. Lachowska, J. Skrzypek, Effect of metal oxide additives on the activity and stability of $Cu/ZnO/ZrO_2$ catalysts in the synthesis of methanol from CO_2 and H_2, Appl. Catal. A: Gen. 310 (2006) 127–137.
[24] Q. Sun, Y.-L. Zhang, H.-Y. Chen, J.-F. Deng, D. Wu, S.-Y. Chen, A novel process for the preparation of Cu/ZnO and $Cu/ZnO/Al_2O_3$ ultrafine catalyst: structure, surface properties, and activity for methanol synthesis from $CO_2 + H_2$, Journal of Catalysis 167 (1997) 92–105.
[25] T. Fujitani, J. Nakamura, The effect of ZnO in methanol synthesis catalysts on Cu dispersion and the specific activity, Cat. Lett. 56 (1998) 119–124.
[26] M. Kurtz, H. Wilmer, T. Genger, O. Hinrichsen, M. Muhler, Deactivation of supported copper catalysts for methanol synthesis, Cat. Lett. 86 (2003) 77–80.

Available online at www.sciencedirect.com

SciVerse ScienceDirect

Ceramics International 39 (2013) 3371–3375

CERAMICS INTERNATIONAL

www.elsevier.com/locate/ceramint

Short communication

Chitosan-assisted combustion synthesis of CuO–ZnO nanocomposites: Effect of pH and chitosan concentration

Thongthai Witoon[a,b,*], Tinnavat Permsirivanich[a], Metta Chareonpanich[a,b]

[a]*National Center of Excellence for Petroleum, Petrochemicals and Advance Material, Department of Chemical Engineering, Faculty of Engineering, Kasetsart University, Bangkok 10900, Thailand*

[b]*Center for Advanced Studies in Nanotechnology and Its Applications in Chemical Food and Agricultural Industries, Kasetsart University, Bangkok 10900, Thailand*

Received 8 June 2012; received in revised form 7 August 2012; accepted 8 August 2012
Available online 19 August 2012

Abstract

CuO–ZnO nanocomposites were synthesized via a chitosan-assisted solution combustion method. The effects of pH and chitosan concentration on the physicochemical properties of the CuO–ZnO nanocomposites have been investigated. Thermal behavior, morphological structures, surface composition, crystal type and specific surface area of the products were characterized by means of thermal gravimetric and differential temperature analysis, scanning electron microscopy, energy dispersive X-ray spectroscopy, X-ray diffraction and N_2-sorption analysis, respectively. Without the use of chitosan, CuO and ZnO particles were separately formed while CuO and ZnO crystallite sizes tended to be decreased with increasing the pH value. Chitosan was found to not only induce a homogeneous mixture of CuO–ZnO nanocomposites but also prevent the growth of CuO and ZnO nanoparticles. Moreover, chitosan also acted as a fuel which promoted the formation of CuO and ZnO nanoparticles at lower temperature.

Keywords: B. Composites; Chitosan; Solution combustion

1. Introduction

Nanocomposites are of great interest in many scientific and technological disciplines as they not only provide the best properties of their individual parents but also create the considerable synergy effects. Recently, CuO–ZnO nanocomposites have received much attention due to their potential uses in many applications, such as catalyst for methanol synthesis [1], solar cells [2], gas sensors [3,4] and photocatalysis [5,6]. Taking photocatalysis as an example, the composites of ZnO and CuO were found to reduce the recombination of electrons and holes and thus promoted the photocatalytic activity to be more efficient than that of an individual ZnO [5,6].

Various techniques such as hydrothermal [4], co-precipitation [7], sol–gel [8] and solution combustion [9–13] have been used to prepare metal oxide nanocomposites. Among these, the solution combustion, a redox reaction taken place between an oxidant and a fuel, has a great advantage through relative low temperature and simple equipment, which makes this method suitable and economic for large-scale production. Several organic compounds such as glycine [9], citric acid [10,11], urea [10,12], L-alanine [10] and polyethylene glycol [13] were found to not only act as a fuel but also have a significant influence in a nucleation and growth of the primary nanoparticles, resulting in a variety of size, shape, phase composition, morphology as well as their potential application [14]. In addition to organic compound, the synthesis parameters such as pH and temperature of the solution considerably affected the variation in the type of metal species [15,16] as well as the structural configuration of the organic compounds [17].

Chitosan, which is a non-toxic, inexpensive and bio-compatible polymer, is an interesting material to be used as

*Corresponding author at: National Center of Excellence for Petroleum, Petrochemicals and Advance Material, Department of Chemical Engineering, Faculty of Engineering, Kasetsart University, Bangkok 10900, Thailand. Tel.: +66 2579 2083; fax: +66 2561 4621.
E-mail address: fengttwi@ku.ac.th (T. Witoon).

0272-8842/$ - see front matter © 2012 Elsevier Ltd and Techna Group S.r.l. All rights reserved.
http://dx.doi.org/10.1016/j.ceramint.2012.08.018

a fuel in the synthesis of metal oxide nanocomposites since a large number of active hydroxyl and amine groups along the backbone chains of chitosan molecules can serve as coordination sites. Herein we propose a novel and promising bioploymer, chitosan, as an organic additive for the solution combustion synthesis of CuO–ZnO nanocomposites. The effects of pH and chitosan concentration on combustion characteristics and physical properties of the composites were investigated and characterized by means of thermal gravimetric and differential thermal analysis (TG–DTA), N_2-sorption isotherms, X-ray diffraction (XRD) and scanning electron microscopy (SEM).

2. Experimental

2.1. Chemicals and reagents

Copper nitrate trihydrate $Cu(NO_3)_2 \cdot 3H_2O$, zinc nitrate hexahydrate $Zn(NO_3)_2 \cdot 6H_2O$, acetic acid CH_3COOH and ammonium hydroxide NH_4OH (28 wt%) were purchased from Sigma-Aldrich Company. Chitosan with 80% deacetylation was purchased from Eland Corporation. The molecular weight of the chitosan determined by Gel Permeation Chromatography (GPC, Waters 600E) using 0.5 M acetic acid and 0.5 M sodium acetate as the eluent was found to be approximately 290 kDa. All chemicals and reagents are of analytical grade and used without any further purification.

2.2. Preparation of CuO–ZnO nanocomposites

Chitosan was dissolved overnight in 100 mL of 1% v/v acetic acid in deionized water at room temperature, agitated with a magnetic stirrer. Subsequently, 3.749 g $Cu(NO_3)_2 \cdot 3H_2O$ and 4.616 g $Zn(NO_3)_2 \cdot 6H_2O$ (mole ratio of Cu/Zn = 1/1) were added into the chitosan solution. Then the pH value of the mixture was quickly adjusted to 6 by the addition of aqueous NH_4OH. The resulting mixture was stirred at 333 K for 6 h to ensure the chitosan completely chelating with the metal ions. Subsequently, the mixture was heated at 353 K to evaporate the solvent. The precipitate was then dried in an oven at 393 K for 24 h. Finally, the product was calcined in a furnace under nitrogen atmosphere at 723 K for 2 h with a heating rate of 2 K/min. In order to investigate the effect of the pH value and the chitosan concentration, the pH value was changed to 7 and 8, while the amount of chitosan addition was varied from 0 to 0.6 g. The samples are denoted as CZ*x*–C*y* (*x* = pH value and *y* = amount of chitosan addition in grams).

2.3. Characterization of CuO–ZnO nanocomposites

The combustion characteristic of the dried samples was investigated with a SDT2960 simultaneous DTA–TGA Universal 2000 at a heating rate of 10 °C/min under a flow of nitrogen (80 mL/min). The specific surface area (S_{BET}) of the composites was determined with a Quantachrome Autosorb-1C instrument at −196 °C. X-ray diffraction (XRD) patterns of the composites were done on a diffractometer (Bruker D8 Advance) using Cu-K_α radiation. The measurements were made at room temperature at a range of 20°–90° on 2θ with a step size of 0.05°. The diffraction patterns were analyzed using the Joint Committee on Powder Diffraction Standards (JCPDS). CuO and ZnO crystallite sizes were calculated by means of the Scherrer Equation as shown below:

$$d = \frac{0.89\lambda}{B\cos\theta} \times \frac{180^\circ}{\pi} \quad (1)$$

where d denotes the mean crystallite size, λ is the X-ray wave length (1.54 Å), and B is the full width half maximum (FWHM) of the peak. The surface morphology and surface compositions of the samples were examined with a field emission scanning electron microscopy (FE-SEM: Hitachi-S4700) equipped with energy-dispersive X-ray spectroscopy (EDS). The samples were sputter coated with gold prior to examination.

3. Results and discussion

Fig. 1 shows a thermal behavior of the products synthesized at different chitosan concentrations investigated by TG–DTA measurement. It can be seen that, without the use of chitosan (CZ_7–C_0), there is an endothermic peak and two exothermic peaks appear at 135, 228 and 259 °C, respectively. The endothermic peak with a weight loss of approximately 10% can be attributed to the loss of residual water in the gel. A large weight loss of approximately 52% between 200 and 280 °C is ascribed to the decomposition of nitrate, $Zn(OH)_2$ to ZnO and $Cu(OH)_2$ to CuO. The addition of chitosan to the precursor solution was found to affect the combustion rate of the gel. At low chitosan concentration (CZ_7–$C_{0.3}$), the peak at approximately 139 °C, corresponding to the removal of water in the gel, still exist. However, the first exothermic peak was found to shift its position from 228 to 203 °C with a sudden decrease in weight of approximately 46%, an indication of autocatalytic combustion behavior at which chitosan served as a fuel. The remaining weight loss (14%) occurring in the region of 203–265 °C could be ascribed to incomplete decomposition of nitrate, $Zn(OH)_2$ to ZnO and $Cu(OH)_2$ to CuO. At a higher chitosan concentration (CZ_7–$C_{0.6}$), the decomposition of the gel occurred suddenly in a single step, which is potentially due to a greater amount of energy released from the reaction as the increase of fuel. However, the maximum of the exothermic peak was found to slightly shift towards a higher temperature (209 °C) when compared to that of the sample CZ_7–$C_{0.3}$. This observation could be due to the entrapment of chitosan molecules surrounded by metal hydroxides, which interrupt the role of chitosan. The similar trends

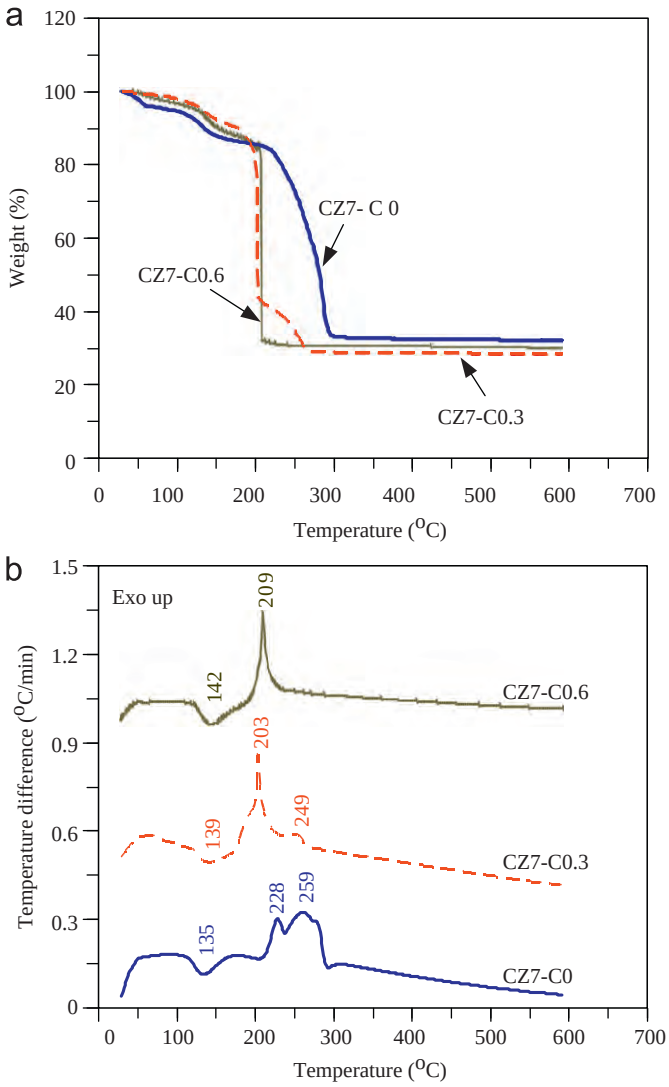

Fig. 1. TG (a) and DTA (b) curves of the dried gel prepared without (CZ_7–C_0) and with chitosan (CZ_7–$C_{0.3}$ and CZ_7–$C_{0.6}$).

were also observed for the samples synthesized at other pH values (not shown here).

The apparent morphologies of the samples synthesized at different pH values and chitosan concentrations examined by means of a SEM are shown in Fig. 2. The surface compositions (Cu/Zn) were investigated by SEM–EDX with several spots and the average value was considered for each system. The results of Cu/Zn ratio of all samples are summarized in Table 1. The samples synthesized without the use of chitosan were found to have two different morphologies (Fig. 2a–c). At pH 6 (Fig. 2a), the sample shows a platelet-like morphology and a pyramid-shaped structure with average size of approximately 1 and 3 μm, respectively. The Cu/Zn ratio of the platelet and the pyramid was found to be 2.53 (circle) and 0.09 (rectangular), respectively, an indication for the separate formation of CuO and ZnO phases since the initial ratio of Cu/Zn was equal to 1. The similar trends were also observed when the pH value was increased to 7 (Fig. 2b) and 8 (Fig. 2c).

Once chitosan was applied at low concentration (Fig. 2d–f), the platelet-like morphology and the pyramid-shaped structure were no longer observed and instead only an aggregation of irregular spherical structure was obtained. The Cu/Zn ratio was found to be 0.88, 0.92 and 1.04 for the samples synthesized at pH 6, 7 and 8, respectively, which was indicative of a homogeneous mixture of CuO and ZnO nanoparticles. The increase of chitosan concentration was found to change the irregular spherical structure to a foamy filament and spongy in nature for the samples synthesized at pH 6 and 7 (Fig. 2g and h). This could be due to the fact that the addition of chitosan in reaction mixture acts as a fuel as evident from the thermal analysis data. The increase in chitosan content acts as a space filling agent, which possibly leaves empty spaces during the combustion process and thus resulting in the existence of huge porosity of the CuO–ZnO nanocomposites. At pH 8 (Fig. 2i), a denser aggregation of irregular spherical structure was obtained. The Cu/Zn ratio was found to be 0.72, 0.75 and 0.80 for the samples synthesized at pH 6, 7 and 8, respectively. Note that these ratios were considerably lower than unity, indicating that the large portion of the external surface of the particles were coated by zinc oxides.

The XRD patterns of the samples synthesized at different pH values and chitosan concentrations are shown in Fig. 3. The peaks at 32.54°, 35.52°, 38.81°, 48.56° and 61.50° of the 2θ were attributed to the CuO diffractions of (110), (002), (111), (202) and (113), respectively. The other diffraction peaks matched the standard data for a heaxagonal wurtzite ZnO (JCPDS 36–1451). The peak intensities of the samples synthesized without the use of chitosan were found to be decreased with increasing the pH of the mixture (Fig. 3a–c), which is attributed to the decrease in crystallinity. The average crystallite sizes of the samples calculated with the Scherrer Equation on the CuO (111) and the ZnO (100) are listed in Table 1. The average crystallite size of CuO was found to be 28.5, 18.2 and 17.8, while that of ZnO was found to be 36.8, 28.9 and 28.5 for the samples synthesized at pH 6, 7 and 8, respectively.

The XRD pattern (Fig. 3a–c) of the samples synthesized with chitosan appeared at the identical 2θ angles as that of the samples synthesized without chitosan, indicating that chitosan did not alter the crystalline phases of the samples. At low chitosan concentration, the CuO and ZnO crystallite sizes were found to be considerably smaller than those of the samples prepared without the use of chitosan. However, further increase in the chitosan concentration resulted in a significant increase in crystallite sizes of CuO and ZnO.

The variation in CuO and ZnO crystallite sizes and their morphologies could be attributed to the interaction between chitosan molecules and metal cations. Under near neutral conditions (pH 6–8), nitrogen atoms of amino groups along the backbone chains of chitosan molecules

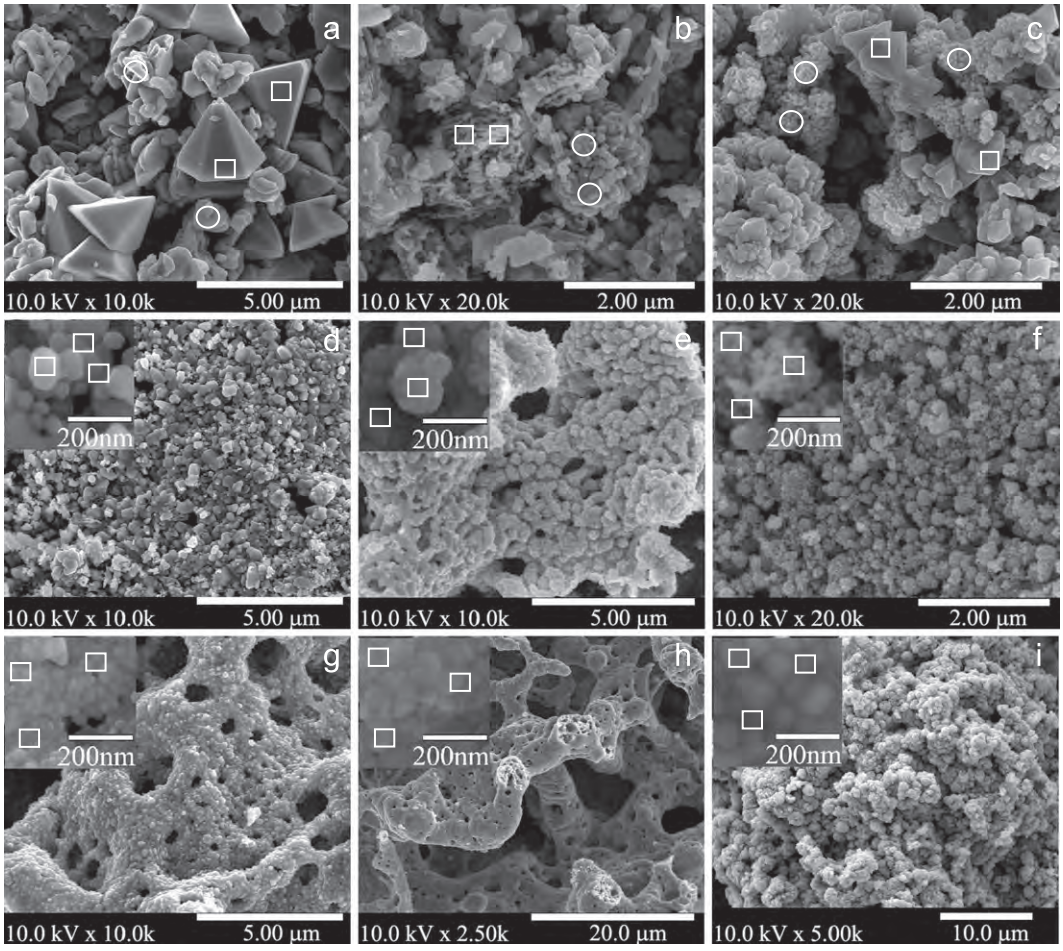

Fig. 2. SEM images of CZ_6–C_0 (a), CZ_7–C_0 (b), CZ_8–C_0 (c), CZ_6–$C_{0.3}$ (d), CZ_7–$C_{0.3}$ (e), CZ_8–$C_{0.3}$ (f), CZ_6–$C_{0.6}$ (g), CZ_7–$C_{0.6}$ (h) and CZ_8–$C_{0.6}$ (i).

Table 1
Surface compositions reported as average value, metal oxides crystallite size and BET surface area.

Catalysts[a]	Position	Cu/Zn	Metal oxides crystallite size (nm)		BET surface area (m^2/g)
			CuO	ZnO	
CZ_6–C_0	rectangular	0.09	28.5	36.8	2.0
	circle	2.53			
CZ_6–$C_{0.3}$	rectangular	0.88	13.4	30.6	28.6
CZ_6–$C_{0.6}$	rectangular	0.72	15.1	24.5	18.4
CZ_7–C_0	rectangular	0.27	18.2	28.9	14.0
	circle	4.44			
CZ_7–$C_{0.3}$	rectangular	0.92	13.6	21.6	31.5
CZ_7–$C_{0.6}$	rectangular	0.75	16.3	26.7	21.4
CZ_8–C_0	rectangular	0.16	17.8	28.5	17.2
	circle	1.31			
CZ_8–$C_{0.3}$	rectangular	1.04	11.8	21.8	32.1
CZ_8–$C_{0.6}$	rectangular	0.80	17.0	26.2	17.8

[a]The samples are denoted as CZ*x*–C*y* where *x* is the pH value and *y* is the amount of chitosan addition in grams.

hold free electrons [18,19], which can bind to copper species and zinc species by chelation. This result not only reduce the quantity of available copper species and zinc species as seeding but also prevent further growth in size of their structure since they were limited within the chitosan network. With further increasing the chitosan concentration at a higher pH value, the chitosan amount was beyond the solubility limit, leading to the formation of highly dense chitosan network. Copper species and zinc species hardly penetrated within the voids of chitosan network and randomly adsorbed on the external chitosan network. Therefore, the role of the chitosan molecules to prevent the growth of particles was inefficient when the excessive amount of the chitosan was used.

4. Conclusion

CuO–ZnO nanocomposites were produced by a chitosan-assisted solution combustion method. Chitosan was found to have three main roles on the formation of the CuO–ZnO nanocomposites: (i) chitosan could induce a homogenous mixture of CuO and ZnO nanoparticles, (ii) chitosan could prevent the growth of CuO and ZnO nanoparticles and (iii) chitosan acted as a fuel. This finding indicates that chitosan constitutes a feasible option as an organic additive for the synthesis of CuO–ZnO nanocomposites via the solution combustion method due to its potentially low costs and environmentally benign nature.

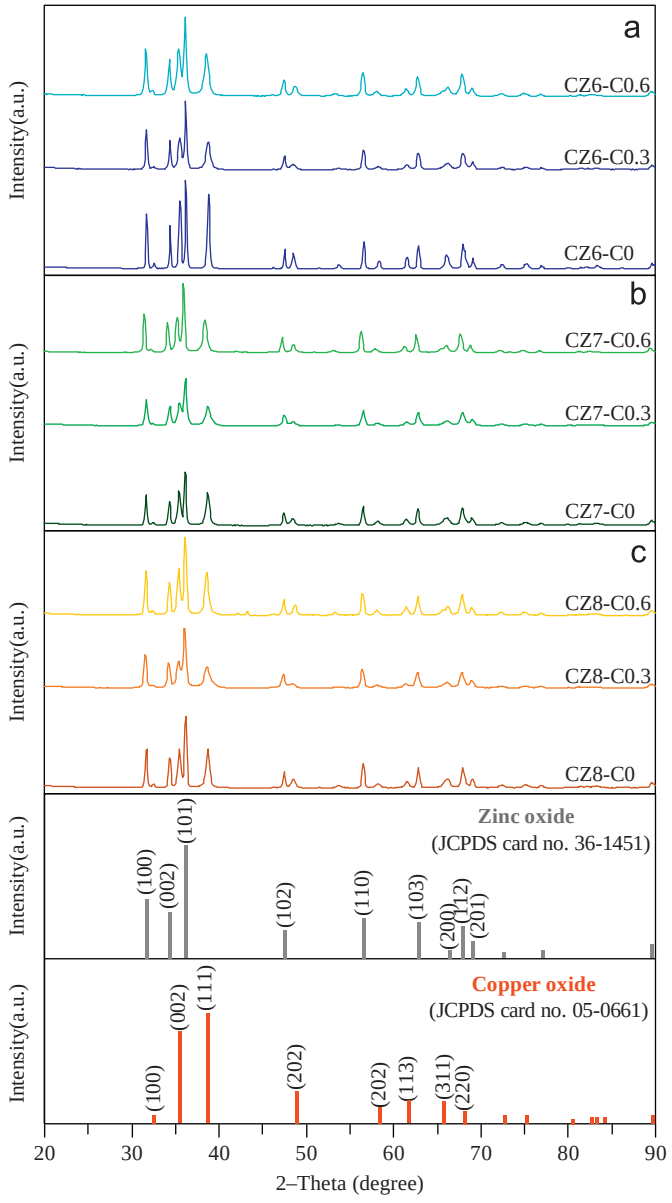

Fig. 3. XRD patterns of the products synthesized at pH 6 (a) pH 7 (b) and pH 8 (c).

Acknowledgments

This work was financially supported by the Research Grant for New Scholar (Grant no. MRG5480196) co-funded by the Thailand Research Fund (TRF); the Commission on Higher Education, Thailand; and Kasetsart University, Thailand. The authors would like to thank the National Center of Excellence for Petroleum, Petrochemical and Advanced Materials (NCE-PPAM), and Kasetsart University Research and Development Institute (KURDI). Support from the "National Research University Project of Thailand (NRU) is also acknowledged.

References

[1] J.P. Greeley, Active site of an industrial catalyst, Science 336 (2012) 810–811.
[2] H. Kidowaki, T. Oku, T. Akiyama, Fabrication and characterization of CuO/ZnO solar cells, Journal of Physics: Conference Series 352 (2012) 012022.
[3] M.-R. Yu, G. Suyambrakasam, R.-J. Wu, M. Chavali, Performance evaluation of ZnO–CuO hetero junction solid state room temperature ethanol sensor, Materials Research Bulletin 47 (2012) 1713–1718.
[4] S.-J. Kim, C.W. Na, I.-S. Hwang, J.-H. Lee, One-pot hydrothermal synthesis of CuO–ZnO composite hollow spheres for selective H_2S detection, Sensors and Actuators B-Chemical 168 (2012) 83–89.
[5] Z. Liu, H. Bai, S. Xu, D.D. Sun, Hierarchical CuO/ZnO "corn-like" architecture for photocatalytic hydrogen generation, International Journal of Hydrogen Energy 36 (2011) 13473–13480.
[6] C. Zhang, L. Yin, L. Zhang, Y. Qi, N. Lun, Preparation and photocatalytic activity of hollow ZnO and ZnO–CuO composite spheres, Materials Letters 67 (2012) 303–307.
[7] R. Raudaskoski, M.V. Niemelä, R.L. Keiski, The effect of ageing time on co-precipitated Cu/ZnO/ZrO_2 catalysts used in methanol synthesis from CO_2 and H_2, Topics in Catalysis 45 (2007) 57–60.
[8] Y. Guo, W. Meyer-Zaika, M. Muhler, S. Vukojević, M. Epple, Cu/Zn/Al xerogels and aerogels prepared by a sol–gel reaction as catalysts for methanol synthesis, European Journal of Inorganic Chemistry 23 (2006) 4774–4781.
[9] X. Guo, D. Mao, G. Lu, S. Wang, G. Wu, Glycine-nitrate combustion synthesis of CuO–ZnO–ZrO_2 catalysts for methanol synthesis from CO_2 hydrogenation, Journal of Catalysis 271 (2010) 178–185.
[10] K. Laishram, R. Mann, N. Malhan, Effect of complexing agents on the powder characteristics and sinterability of neodymium doped yttria nanoparticles, Powder Technology 229 (2012) 148–151.
[11] X. Li, Z. Feng, J. Lu, F. Wang, M. Xue, G. Shao, Synthesis and electrical properties of $Ce_{1-x}Gd_xO_{2-x/2}$ (x=0.05–0.3) solid solutions prepared by a citrate-nitrate combustion method, Ceramics International 38 (2012) 3203–3207.
[12] K. Laishram, R. Mann, N. Malhan, Single step synthesis of yttrium aluminum garnet ($Y_3Al_5O_{12}$) nanopowders by mixed fuel solution combustion approach, Ceramics International 37 (2011) 3743–3746.
[13] W. Wang, X. Liu, F. Gao, C. Tian, Synthesis of nanocrystalline $Ni_1Co_{0.2}Mn_{1.8}O_4$ powders for NTC thermistor by a gel auto-combustion process, Ceramics International 33 (2007) 459–462.
[14] D. Parviz, M. Kazemeini, A.M. Rashidi, Kh.J. Jozani, Synthesis and characterization of MoO_3 nanostructures by solution combustion method employing morphology and size control, Journal of Nanoparticle Research 12 (2010) 1509–1521.
[15] M. Ajmal, A.H. Khan, S. Ahmad, A. Ahmad, Role of sawdust in the removal of copper(II) from industrial wastes, Water Research 32 (1998) 3085–3091.
[16] A. Degen, M. Kosec, Effect of pH and impurities on the surface charge of zinc oxide in aqueous solution, Journal of the European Ceramic Society 20 (2000) 667–673.
[17] J. Berger, M. Reist, J.M. Mayer, O. Felt, N.A. Peppas, R. Gurny, Structure and interactions in covalently and ionically crosslinked chitosan hydrogels for biomedical applications, European Journal of Pharmaceutics and Biopharmaceutics 57 (2004) 19–34.
[18] A.R. Shetty, Master's Thesis: Metal Anion Removal From Wastewater Using Chitosan in a Polymer Enhanced Diafiltration System, Worcester Polytechnic Institute, United States, 2006.
[19] V.K. Mourya, N.N. Inamdar, A. Tiwari, Carboxymethyl chitosan and its applications, Advanced Materials Letters 1 (2010) 11–33.

J Porous Mater (2013) 20:481–488
DOI 10.1007/s10934-012-9619-5

Effect of bimodal porous silica on particle size and reducibility of cobalt oxide

Thongthai Witoon · Metta Chareonpanich · Jumras Limtrakul

Published online: 4 August 2012

Abstract In this study, the effect of bimodal porous silica (BPS) on particle size and reducibility of cobalt oxide has been investigated. Unimodal porous silica (UPS) was used for comparison purposes. Both silica supports were impregnated with an aqueous solution of cobalt nitrate to obtain cobalt loadings of about 10 wt%. Pore structure, specific surface area, morphology and cobalt oxide crystallite size of the cobalt oxide loaded on porous silicas were systematically characterized by means of N_2-sorption, X-ray diffraction, scanning electron microscopy and transmission electron microscopy. The reduction behavior profiles and the activation energy for the reducibility of the cobalt oxide were studied by dynamic thermal gravimetric under flow of H_2. The average particle size of cobalt oxide loaded on the BPS sample was revealed to be slightly larger than that loaded on the UPS sample, likely because cobalt oxide particles were distributed both on mesopores and macropores. The reduction temperatures of the cobalt oxide loaded on the BPS sample were found to be evidentially lower than those of the cobalt oxide loaded on the UPS sample.

Keywords Porosity · Particle size · Aggregation · Silica · Cobalt · Reduction behavior

T. Witoon (✉) · M. Chareonpanich
Department of Chemical Engineering, Faculty of Engineering, National Center of Excellence for Petroleum, Petrochemicals and Advance Material, Kasetsart University, Bangkok 10900, Thailand
e-mail: fengttwi@ku.ac.th

T. Witoon · M. Chareonpanich · J. Limtrakul
Center for Advanced Studies in Nanotechnology and Its Applications in Chemical Food and Agricultural Industries, Kasetsart University, Bangkok 10900, Thailand

1 Introduction

Recently, the intensive concerns of fossil energy depletion, air pollution and global climate change have encouraged many researchers to focus in the production of clean alternative energy. In order to deal with continually massive fuel consumption and the restriction of the emitted pollutants, high quality transportation fuels are needed. One promising source of alternative energy comprises synthetic fuels produced by the Fischer–Tropsch process, which have received increasing attention worldwide due to their compatibility with existing petroleum infrastructure and vehicles [1]. Cobalt metal is a good catalyst for Ficher–Tropsch synthesis (FTS), especially when high-chain-growth probability and low branching probability are required [2]. In order to expose as many cobalt atoms as possible to gaseous reactants, cobalt precursor is normally deposited on porous supports such as silica, alumina, titania and carbon nanotubes [3, 4]. Among these, silica is becoming very competitive because of its economical potential and availability (as it can be produced from a renewable resource such as rice husk ash).

The textural properties of porous silica supports and cobalt-support interaction have a profound impact on the size, dispersion and catalytic performance of cobalt catalysts [5–7]. For instance, the catalytic activity is proportional to the amount of active sites. High surface area of catalyst support can provide high active surface, however a support with high surface usually contains a large number of small pores, resulting in poor diffusion of reactants, intermediates and product. On the other hand, low dispersion of Co_3O_4 is often obtained for large-pore silica-supported cobalt catalysts due to an aggregation of cobalt atoms, leading in turn to low catalytic activity. In order to overcome these limitations, a support with two independently adjustable pore

diameters—one in the macropore diameter to enhance mass transfer and the other in the nanometer range to maintain high surface area—is required. Tsubaki et al. [8] prepared a bimodal catalyst containing mesopores and macropores by introducing silica sols into large-pore silica gel. Such a catalyst exhibited high carbon monoxide conversion and low methane selectivity.

An appropriate interaction of cobalt with the support is also a favorable property in achieving high activity and high selectivity to long chain hydrocarbons during Fischer–Tropsch synthesis. Strong cobalt-support interaction may leave a fraction of inactive cobalt species after reduction. Until recently, there has been, however, some lack of information about the reduction behavior of bimodal porous silica-supported cobalt catalysts.

Herein, we report the effect of bimodal porous silica on particle size and reducibility of cobalt oxide. The reduction behavior profiles and the kinetic information for the reducibility of bimodal porous silica supported catalyst were studied by dynamic thermal gravimetry under flow of H_2 at different heating rates. Meanwhile, the apparent activation energies for their thermal reduction were evaluated by the Kissinger method [9–12]. Cobalt-loaded unimodal porous silica having an identical mesopore diameter was prepared for comparison purposes. Pore structure, phases of cobalt oxides and morphology of the supports and the porous silica-supported cobalt catalysts were characterized by means of N_2-sorption isotherms, X-ray diffraction (XRD), scanning electron microscopy (SEM), and transmission electron microscopy (TEM).

2 Experimental

2.1 Chemicals and reagents

Chitosan with 80 % deacetylation was purchased from Eland Corporation. The molecular weight of the chitosan determined by Gel Permeation Chromatography (GPC, Waters 600E) using 0.5 M acetic acid and 0.5 M sodium acetate as the eluent was approximately 290 kDa. Sodium silicate ($Na_2Si_3O_7$: 27 wt% SiO_2, 4 wt% NaOH) was obtained from Thai Silicate Company. Cobalt nitrate hexahydrate (Co $(NO_3)_2$ $6H_2O$), acetic acid and sodium hydroxide were purchased from Sigma–Aldrich Company.

2.2 Porous silica synthesis

Bimodal porous silica was prepared following our recent reports [13]. In a typical synthesis, 0.1 g chitosan was dissolved in 60 ml of 2 % v/v acetic acid in deionized water at room temperature. Then, 3.7 g of sodium silicate solution (28 wt% SiO_2) was primarily diluted with 10 ml deionized water and slowly added to the chitosan solution with vigorous stirring. The pH of mixture was adjusted to 6. Subsequently, the hydrolysis–condensation reaction was carried out at 40 °C for 24 h, and then the resultant solution was aged in a Teflon-lined autoclave at 60 °C for 24 h. The solid product was filtered, washed several times with distilled water, dried at 120 °C for 12 h and calcined at 600 °C for 4 h at a heating rate of 2 °C/min. Unimodal porous silica was synthesized by using conditions similar to those mentioned above but without the addition of chitosan. The bimodal and unimodal porous silica products were designated as BPS and UPS, respectively.

2.3 Catalyst preparation

Cobalt was introduced into silica supports by an aqueous incipient wetness impregnation using solutions of cobalt nitrate prepared to obtain 10 wt% cobalt content in the final catalysts. The samples were dried in an oven at 120 °C for 12 h and then calcined in a flow of dry air at 350 °C for 4 h at a heating rate of 1 °C/min. The cobalt loaded on bimodal and unimodal porous silica products were designated as Co/BPS and Co/UPS, respectively.

2.4 Characterization

2.4.1 N_2-sorption analysis

The specific surface area, mean pore diameter and pore volume of both supports, and supports after cobalt metal loading, were determined by N_2-sorption analysis with a Quantachrome Autosorb-1C instrument at −196 °C. Prior to each measurement, the samples were degassed at 200 °C for 12 h. Pore size distributions of the samples were determined from both adsorption and desorption branches of the isotherms in accordance with the Barrett–Joyner–Hallenda (BJH) method. The specific BET (S_{BET}) was estimated for P/P_0 values from 0.05 to 0.30. The pore volume was reported as mesopore (2–50 nm) and macropore (>50 nm) volumes.

2.4.2 Scanning electron microscopy (SEM)

The surface morphology of the samples was assessed with the application of a scanning electron microscope (SEM; Nova NanoSEM 2300). The SEM was operated at 10 kV of accelerating voltage. The samples were not coated with gold.

2.4.3 X-ray powder diffraction (XRD)

The XRD measurement was performed at room temperature with a Phillips powder diffractometer using monochromatized Cu-Kα radiation. Cobalt phases were detected by

comparing the diffraction patterns to those of the standard powder XRD file compiled by the joint committee on powder diffraction standards (JCPDS). The Co_3O_4 crystallite size was calculated by means of the Scherrer Equation from the most intense Co_3O_4 peak at $2\theta = 36.9$ as shown below:

$$d = \frac{0.89\lambda}{B\cos\theta} \times \frac{180^\circ}{\pi} \quad (1)$$

where d denotes the mean crystallite diameter, λ is the X-ray wave length (1.54 Å), and B is the full width half maximum (FWHM) of the Co_3O_4 diffraction peak.

2.4.4 Transmission electron microscopy (TEM)

The nanostructure of cobalt oxide particles was revealed with the application of a transmission electron microscope (TEM; JEOL JEM-2010). In order to prepare the samples for TEM analysis, the sample was suspended in ethanol and sonicated for 3 min. The suspension was dropped onto a copper grid coated with a film of carbon and dried at room temperature.

2.4.5 Thermal gravimetric analysis

The reduction behavior of the Co/UPS and Co/BPS catalysts was determined with a SDT2960 simultaneous DTA-TGA Universal 2000. Prior to reduction measurement and in order to remove pre-adsorbed CO_2 and H_2O, the catalyst (8–10 mg) was first activated by heating it from room temperature in a flow of pure argon (50 mL/min) at a rate of 10 °C/min until 200 °C was achieved, and the sample was kept constant at 200 °C for 1 h; then the sample was cooled down to the temperature of 50 °C. Subsequently, hydrogen with a flow rate of 50 mL/min was introduced into the system. The samples were linearly heated to 800 °C at a rate of 5 °C/min while the change in the sample weight was being recorded. An identical experiment was repeated with heating rate values of 10, 15 and 20 °C/min, respectively.

3 Results and discussion

Figure 1a presents nitrogen adsorption–desorption isotherms of the porous silica products synthesized with (BPS) and without (UPS) chitosan template. The isotherm of the UPS sample is a typical type IV with H2 hysteresis loop, indicating that this material contains mainly pores of ink-bottle shape with narrow openings of similar dimensions [14]. The isotherm of the BPS sample is characteristic of type IV–II composite isotherms, an indication of mesoporous and macroporous structures. The hysteresis loop ($0.6 < P/P_0 < 0.85$) of the BPS sample is H3 hysteresis loop, which can be ascribed to slit-shaped pores [14] caused by loosely aggregated silica domains. Note that, for the BPS sample, irreversibility of adsorption is observed in the almost whole pressure range; this can be attributed to the presence of many constrictions in pores [14–16].

The pore size distribution calculated from both adsorption and desorption branches of the BPS and UPS samples are presented in Fig. 1b, c, respectively. It can be seen that the pore size distribution of the UPS sample determined from the adsorption branch (Fig. 1b) is much broader than that of the desorption branch (Fig. 1c). This was due to the fact that the amount of nitrogen gas condensed and remained in the pores gave rise to pore-blocking [15]. With the chitosan template (BPS), only an insignificant difference of pore size distributions determined from the adsorption and desorption branches is observed, which might be due to the smaller size of the silica domains. (This evidence is further confirmed by TEM images shown later). Everett [16] reported that in every systems where pore blocking occurred, pore size distribution curves derived from the desorption branch of the isotherm could possibly give a misleading picture of the pore structure. Therefore, the pore size distribution derived from the adsorption was better used for comparison. The pore size distribution derived from the adsorption of the UPS sample shows a unimodal pore distribution while that of the BPS sample displays a bimodal pore distribution: one in the range of mesopore and the other in the range of macropore (40–200 nm). The mean mesopore diameter of both samples is identical at approximately 6.5 nm.

The N_2 adsorption–desorption isotherms and the corresponding pore size distribution curves of cobalt loaded bimodal porous silica (Co/BPS) and cobalt-loaded unimodal porous silica (Co/UPS) are shown in Fig. 1b, d and f. The shape of the N_2 adsorption–desorption of both catalysts (Fig. 1b) is quite similar to their corresponding porous silica supports (see Fig. 1a), suggesting that the structure of porous silica was mostly retained upon cobalt impregnation in all cases. Also note that the shape of pore size distribution curves (Fig. 1d) remained the same, though the intensity of pores was slightly decreased.

The physical properties—such as BET surface area, mean pore diameter, and pore volume—for the porous silica supports (BPS and UPS) and their corresponding Co-supported catalysts (Co/BPS and Co/UPS) are listed in Table 1. The BET surface area and mesopore volume of all samples were comparable, whereas the macropore volume of the BPS sample was approximately 21 times larger than that of the UPS sample. Cobalt introduction on both samples led to sharp decreases in BET surface and mesopore volume of 20 and 30 %, respectively. This might be attributed to a partial blockage of the pores of the supports.

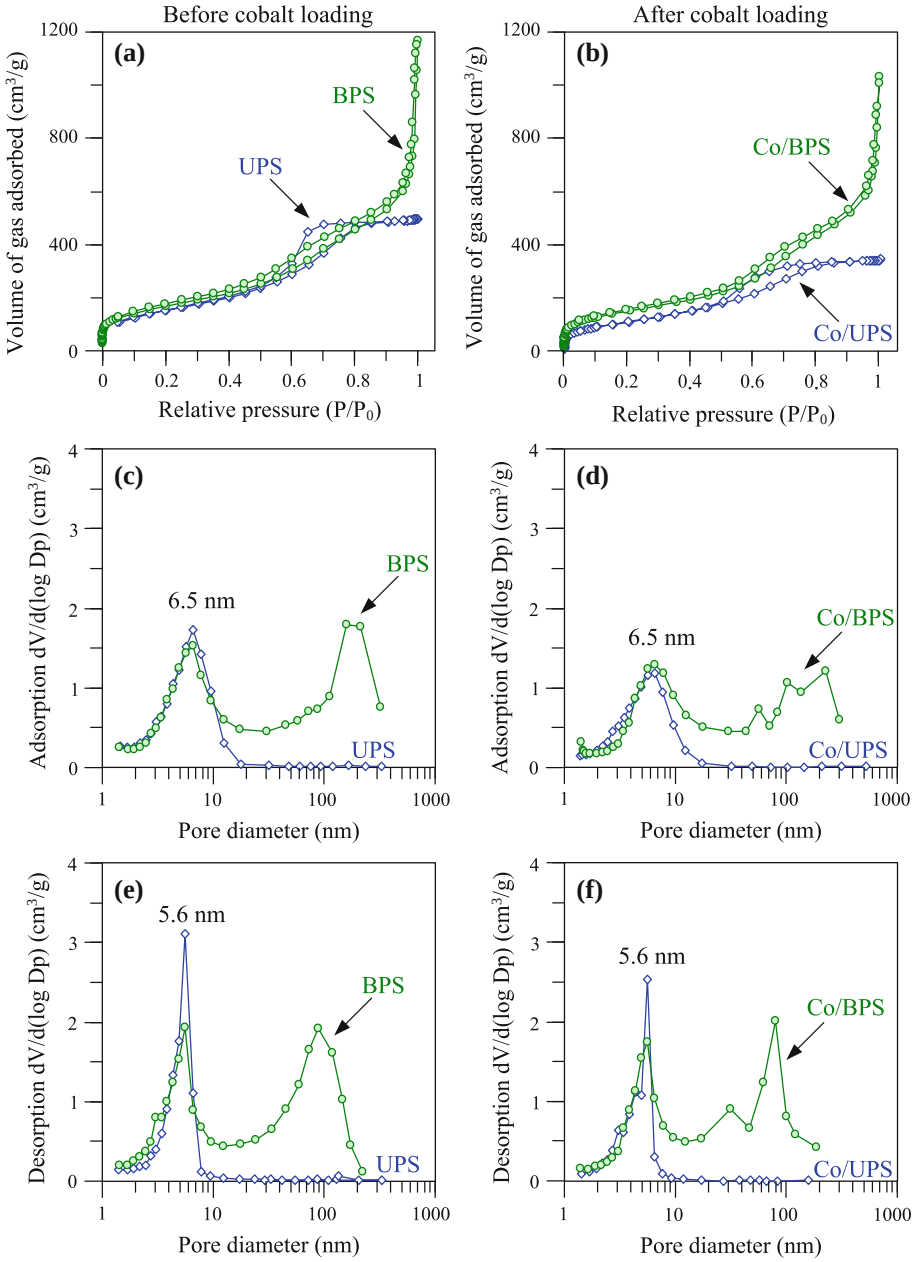

Fig. 1 N_2 adsorption–desorption isotherms (**a**, **b**) and pore size distribution curves derived from the adsorption branch (**c**, **d**) and the desorption branch (**e**, **f**) of silica supports (**a**, **c**, **e**) and silica-supported cobalt catalysts (**b**, **d**, **f**)

Table 1 Textural properties of porous silica supports and porous silica supported cobalt catalysts

Catalysts	BET surface area (m^2/g)	BJH pore diameter (nm)	Mesopore volume (cm^3/g)	Macropore volume (cm^3/g)
UPS	565	6.5	0.86	0.03
BPS	546	6.5 and 100–200	0.91	0.65
Co/UPS	439	6.5	0.57	0.01
Co/BPS	411	6.5 and 100–200	0.65	0.55

Nevertheless, the macropore volume of the BPS sample was slightly decreased (15 %), implying that the addition of cobalt slightly affected the macropore volume.

The XRD measurement was performed to investigate types of cobalt species and average Co_3O_4 crystallite size. As shown in Fig. 2, Co_3O_4 spinel phase with 2θ values of 31.3, 36.9, 44.8, 59.4 and 65.3 was found in both catalysts. The Co_3O_4 crystallite size was calculated by using the Scherrer Equation. The Co_3O_4 crystallite size (10.6 nm) of the Co/BPS catalyst was found to be slightly larger than that of the Co/UPS catalyst (9.8 nm). This could be due to the fact that the cobalt loaded on bimodal porous silica can deposit both on mesopores and macropores. Once the cobalt crystallites are supported on a macropore, more cobalt crystallites can easily aggregate and form larger clusters. In order to directly observe the size and location

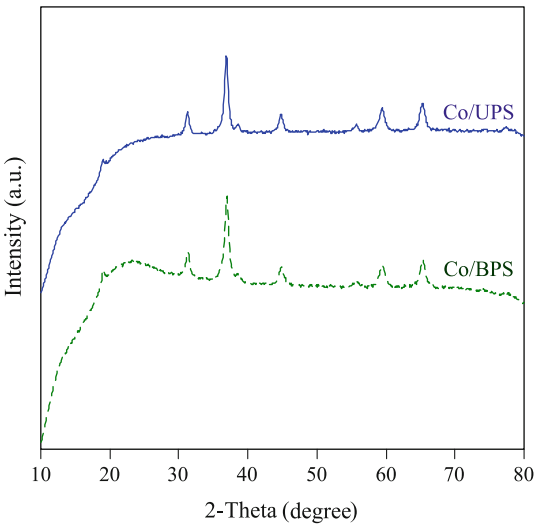

Fig. 2 XRD patterns of Co/UPS catalyst (solid line) and Co/BPS catalyst (dash line)

of cobalt particles distributed on porous silica, SEM and TEM analysis of both catalysts were performed.

Figure 3 shows SEM images of the Co/UPS and Co/BPS samples. It can be seen that the morphology of the Co/UPS catalyst (Fig. 3a) consisted of irregularly formed glass pieces, which was significantly different from the Co/BPS catalyst. The difference in the sizes of the pieces only depended on the extent of grinding and was not related to the preparation conditions. The cobalt particles (white spots) were deposited in the glass pieces. In contrast to Co/UPS catalyst, the SEM image of Co/BPS catalyst (Fig. 3b) has shown obviously very fine powder and secondary particles aggregated by spherical-like primary particles. The aggregates of secondary particles led to the formation of macroporosity as shown by the result of pore size distribution (Fig. 1). SEM-EDX was also performed to examine the surface compositions of the catalysts. The analysis of several spots was carried out and the average value was considered for each system. Cobalt content of the Co/UPS and the Co/BPS catalysts were found to be 9.44 and 9.64 %, respectively—results which were close to the original catalyst preparation content. These results were an indication of the uniform distribution of the cobalt particles, even though the structures of both catalysts were quite different.

TEM was used to investigate the pore structure of the UPS and BPS samples. It can be clearly seen that the UPS sample (Fig. 4a) shows a highly dense and extremely large silica domain (more than 5 μm) built up from an aggregation of silica nanoparticles. In contrast to the UPS sample, the BPS sample exhibits smaller silica domains (150–250 nm) with looser aggregation (Fig. 4b). The small size of the silica domains is expected to diminish the effect of pore blocking as mentioned in the pore size distribution results. TEM also provided direct observations on the size and distribution of cobalt particles in the bimodal and unimodal porous silicas (Fig. 4c–f). The darker spots on the catalyst granules represent the areas of high concentration of Co_3O_4, whereas the other parts represent the silica support with minimal or no Co_3O_4. Cobalt particles loaded on the BPS sample were evidently found to be distributed as clusters both inside the silica matrix and on the exterior surface of the silica particles, while cobalt particles loaded on the UPS sample were mostly found inside the silica matrix. This result is in good agreement with the results of XRD and SEM.

The influence of bimodal pores on the reduction behavior of the cobalt oxide-supported catalysts was studied by dynamic thermal gravimetric analysis. Figure 5 shows the derivative weight loss (DTG) profiles of both catalysts at different heating rates (5, 10, 15, and 20 °C/min). As observed, all the DTG profiles show two major peaks. The first peak at temperature between 260 and

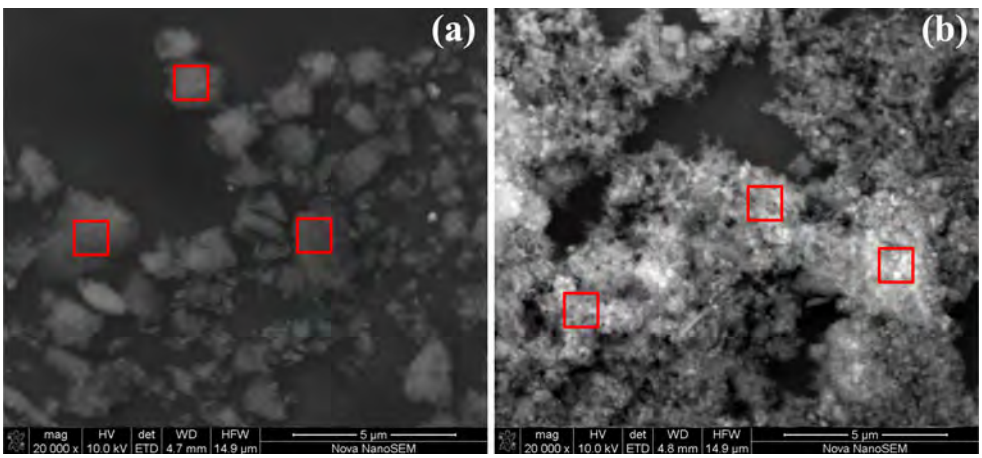

Fig. 3 SEM images of Co/UPS catalyst (**a**) and Co/BPS catalyst (**b**)

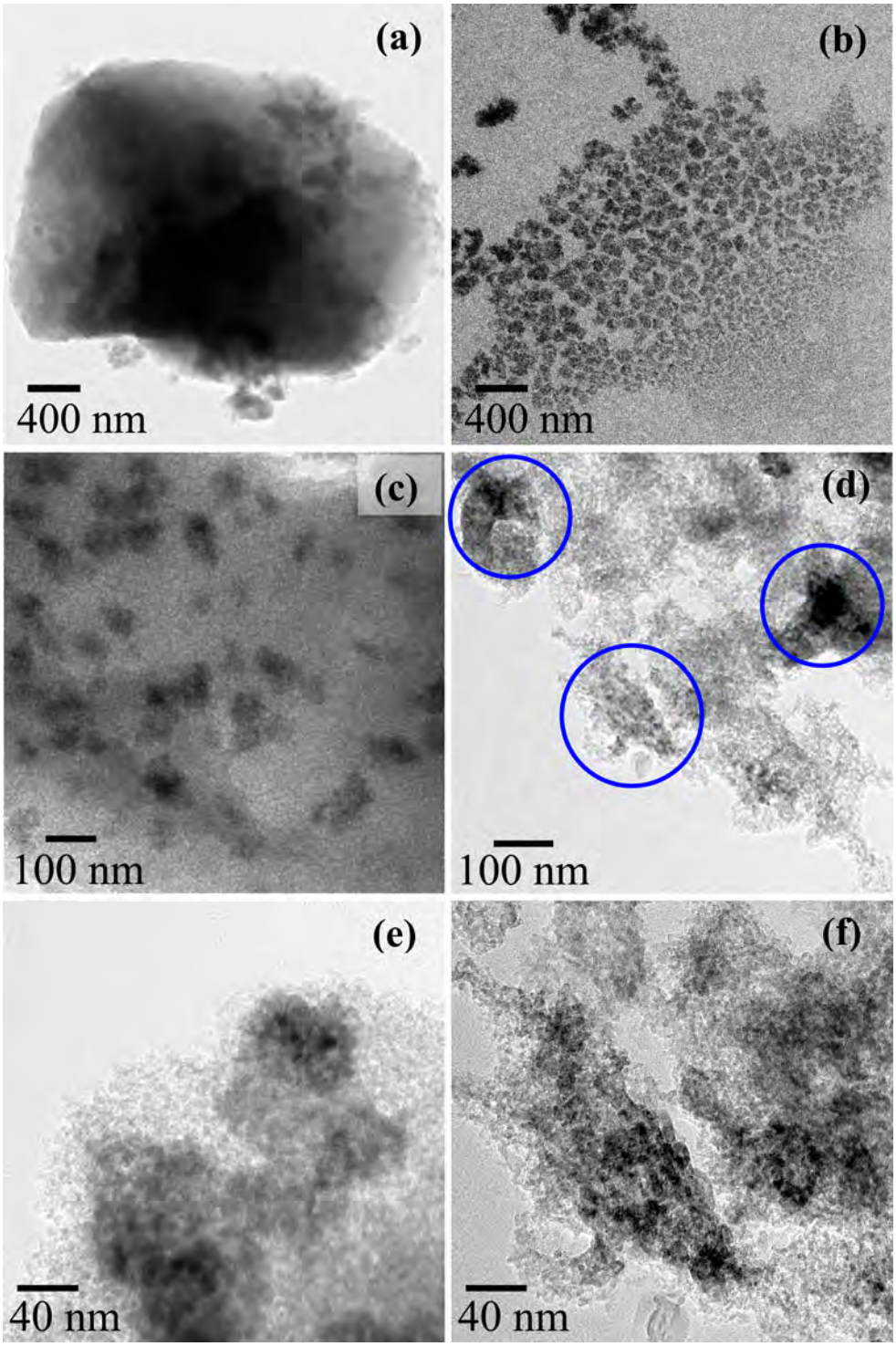

Fig. 4 TEM images of UPS sample (**a**), BPS sample (**b**), Co/UPS catalyst (**c**, **e**) and Co/BPS catalyst (**d**, **f**)

270 °C can be attributed to the reduction of Co_3O_4 to CoO [5–7]. The second peak located in the temperature ranges 350–510 °C corresponds to the reduction of CoO phase to Co^0 [5–7]. It can be seen that the reduction temperature at both stages of the Co/BPS catalyst was lower than that of the Co/UPS catalyst at all heating rates.

The activation energy of the reduction of cobalt oxides to metallic cobalt was determined by the Kissinger method [9–12]. Kissinger's equation (2) assumes that the reaction rate reaches its maximum at the temperature (T_p) of the DTG peak and that the degree of conversion (α) at T_p is constant, although that does not apply in every case.

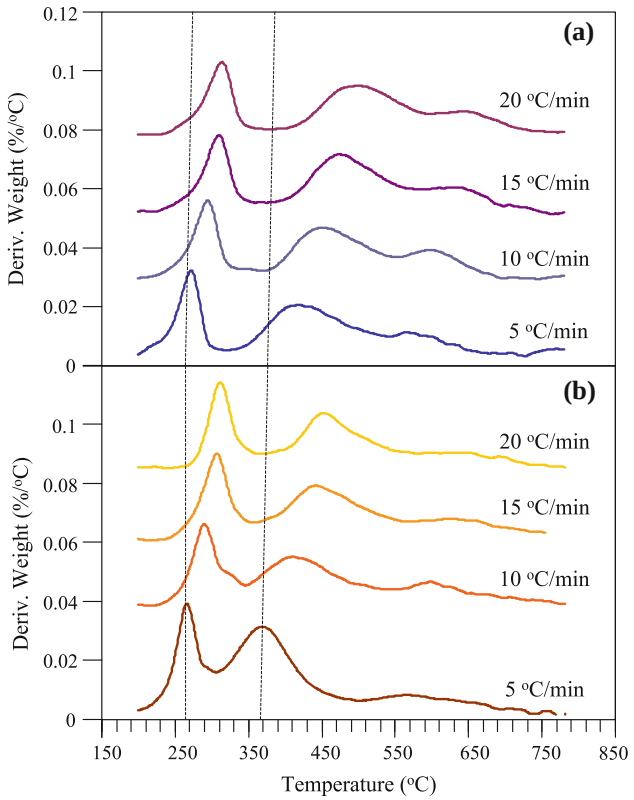

Fig. 5 DTG curves of all catalysts under hydrogen at different heating rates: **a** Co/UPS catalyst and **b** Co/BPS catalyst

$$\ln\left(\frac{\beta}{T_p^2}\right) = \ln\left(\frac{AR}{E}\right) - \frac{E}{R}\frac{1}{T_p} \tag{2}$$

In Eq. (2), β is the heating rate, E is the activation energy, R is the universal gas constant and A is the pre-exponential factor. The activation energies of the transformations of Co_3O_4 to CoO and CoO to Co^0 were calculated from the slope in the plots of ln (β/T_p^2) vs $1/T_p$ (Fig. 6), and the results are shown in Fig. 7. The activation energies for both reduction stages of the Co/BPS catalyst were evidently found to be lower than those of the Co/UPS catalyst. There are two possible reasons to explain this result: one is the difference in size of cobalt oxide particles, and the other is the difference in structure of the supports. It is known that the reduction of larger-size cobalt oxide crystallites is easier than small ones because the larger cobalt oxide crystallites provide a weak interaction between the cobalt oxide and the support. However, the cobalt oxide crystallite sizes of both catalysts were found to be not much different (10.6 nm for the Co/BPS catalyst and 9.8 nm for the Co/UPS catalyst). Therefore, the difference of the reduction behavior for both catalysts should not be affected by the size of the cobalt particles. It can be seen in SEM and TEM images that the cobalt oxide particles loaded on the UPS sample were trapped within the large

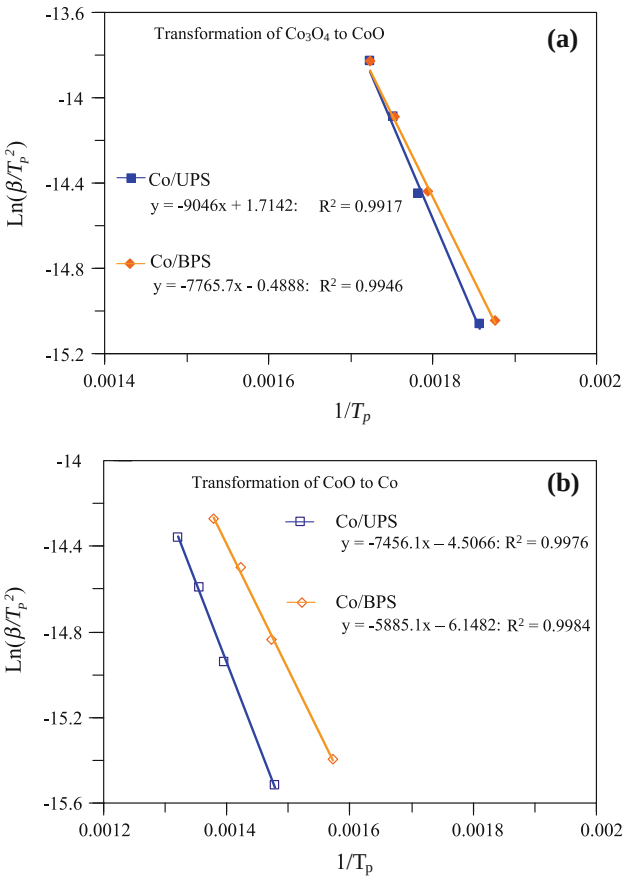

Fig. 6 Plots of ln (β^2/T_p) vs ($1/T_p$): **a** reduction of Co_3O_4 to CoO and **b** reduction of CoO to Co

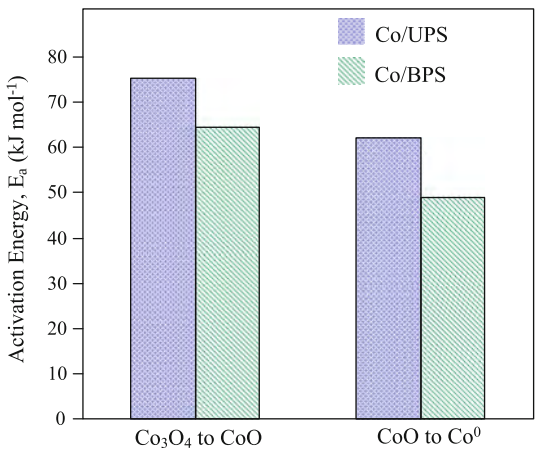

Fig. 7 Activation energy of reduction of Co_3O_4 to CoO and CoO to Co^0 for both catalysts

silica domains. Thus the hydrogen takes long time to diffuse inside the small pores in order to react with cobalt oxide. However, the BPS sample contains small pores and large pores at the same time. The diffusion of hydrogen in small pores apparently occurred in small domains segregated as a result of the macropores being randomly

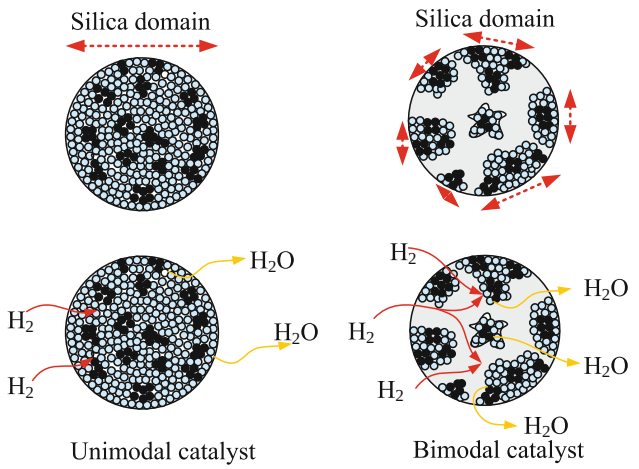

Fig. 8 Schematic diagram representing the silica domain of the unimodal porous silica and the bimodal porous silica and the effect of their structures on gas diffusion

dispersed inside the BPS sample. In other words, the silica domains of the BPS sample were considerably smaller than those of the UPS sample. The distances for hydrogen diffusion in the silica domains of the bimodal porous silica were much shorter (Fig. 8). Therefore, the cobalt oxides loaded on the BPS sample were easily reducible when compared to those loaded on the UPS sample.

4 Conclusion

The purpose of this paper is to investigate the effect of BPS on particle size and reducibility of cobalt oxide. The BPS material was synthesized by using chitosan as template. An UPS material with identical mesopore size to the BPS material was prepared for comparison purposes, and the silica domains of the BPS sample were found to be considerably smaller than those of the UPS sample. Macroporosity of the BPS sample was a result of the inter-particle voids formed by an aggregation of the small size of the silica domains. The larger cobalt oxide crystallite size of the Co/BPS catalyst could be due to the deposition of cobalt oxide at two different locations. The BPS material could promote the transformations of Co_3O_4 to CoO and CoO to Co^0. It was demonstrated that the diffusion of gas molecules into and out of the mesopores of the BPS materials was faster than that of the UPS material due to the existence of macroporosity and the small size of the silica domains.

Acknowledgments This work was financially supported by the Research Grant for New Scholar (Grant No. MRG5480196) co-funded by the Thailand Research Fund (TRF); the commission on Higher Eduction, Thailand; and Kasetsart University, Thailand. The authors would like to thank the National Center of Excellence for Petroleum, Petrochemical and Advanced Materials (NCE-PPAM), Kasetsart University Research and Development Institute (KURDI), and the National Science and Technology Development Agency (NSTDA Chair Professor and NANOTEC Center of Excellence). Support from the National Research University Project of Thailand (NRU) is also acknowledged.

References

1. M.E. Dry, Catal. Today **71**, 227 (2002)
2. A.Y. Khodakov, W. Chu, P. Fongarland, Chem. Rev. **107**, 1692 (2007)
3. S. Storsæter, B. Tøtdal, J.C. Walmsley, B.S. Tanem, A. Holmen, J. Catal. **236**, 139 (2005)
4. A. Tavasoli, K. Sadagiani, F. Khorashe, A.A. Seifkordi, A.A. Rohani, A. Nakhaeipour, Fuel Process. Technol. **89**, 491 (2008)
5. A.M. Saib, M. Claeys, E. van Steen, Catal. Today **71**, 395 (2002)
6. A.Y. Khodakov, A. Griboval-Constant, R. Bechara, V.L. Zholobenko, J. Catal. **206**, 230 (2002)
7. D. Song, J. Li, J. Mol. Catal. A: Chem. **247**, 206 (2006)
8. N. Tsubaki, Y. Zhang, S. Sun, H. Mori, Y. Yoneyama, X. Li, K. Fujimoto, Catal. Commun. **2**, 311 (2001)
9. H.E. Kissinger, Anal. Chem. **29**, 1702 (1957)
10. Y.J. Wan, J.L. Li, D.H. Chen, J. Therm. Anal. Cal. **90**, 415 (2007)
11. H.-Y. Lin, Y.-W. Chen, Mater. Chem. Phys. **85**, 171 (2004)
12. M. Sprynskyy, J. Niedojadło, B. Buszewski, J. Phys. Chem. Solid. **72**, 1015 (2011)
13. T. Witoon, M. Chareonpanich, J. Limtrakul, J. Sol–Gel Sci. Technol. **56**, 270 (2010)
14. M. Kruk, M. Jaroniec, Chem. Mater. **13**, 3169 (2001)
15. S.J. Gregg, K.S.W. Sing, *Adsorption, Surface Area and Porosity*, 2nd edn. (Academic Press, London, 1982), pp. 111–190
16. D.H. Everett, in Characterization of Porous Solids, ed By S.J. Gregg, K.S.W. Sing (Society of Chemical Industry, London, 1979), p. 253

Materials Chemistry and Physics 137 (2012) 235–245

Contents lists available at SciVerse ScienceDirect

Materials Chemistry and Physics

journal homepage: www.elsevier.com/locate/matchemphys

Polyethyleneimine-loaded bimodal porous silica as low-cost and high-capacity sorbent for CO_2 capture

Thongthai Witoon [a,b,*]

[a] National Center of Excellence for Petroleum, Petrochemicals and Advance Material, Department of Chemical Engineering, Faculty of Engineering, Kasetsart University, Bangkok 10900, Thailand
[b] Center for Advanced Studies in Nanotechnology and Its Applications in Chemical Food and Agricultural Industries, Kasetsart University, Bangkok 10900, Thailand

HIGHLIGHTS

- PEI-impregnated bimodal porous silica as low-cost sorbent for CO_2 capture.
- Macropores enhances the accessibility of PEI inside the mesopores.
- PEI-loaded bimodal porous silica proved to provide higher effective amine density to adsorb CO_2.
- PEI-loaded bimodal porous silica exhibits a high CO_2 uptake with excellent regeneration efficiency.

GRAPHICAL ABSTRACT

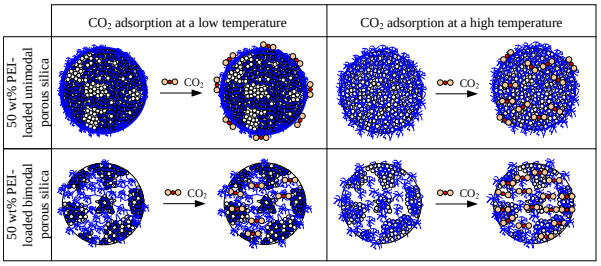

ARTICLE INFO

Article history:
Received 22 April 2012
Received in revised form
4 August 2012
Accepted 4 September 2012

Keywords:
Sol–gel growth
Nanostructures
Thermogravimetric analysis (TGA)
Adsorption

ABSTRACT

In this work, bimodal (meso-macro) porous silicas with different mesopore diameters synthesized by using rice husk ash as a low-cost silica source and chitosan as a natural template were used as a polyethyleneimine (PEI) support for CO_2 capture. Unimodal porous silica supports with equivalent mesopore diameters to bimodal porous silica supports have been prepared for purpose of comparison. Effects of different PEI contents (10, 20, 30, 40 and 50 wt%) on CO_2 sorption capacity have been systematically investigated. The porous silica supports and the PEI-loaded porous silica supports were characterized by N_2-sorption analysis, scanning electron microscopy, Fourier transform infrared spectroscopy and thermal gravimetric analysis. CO_2 sorption measurements of all PEI-loaded porous silica supports were performed at different adsorption temperatures (60, 75, 85, 90, 95 and 105 °C). At low PEI contents (10–20 wt%), the CO_2 sorption of all adsorbents was found to decrease as a function of adsorption temperature, which was a characteristic of a thermodynamically-controlled regime. A transition from the thermodynamically-controlled regime to a kinetically-controlled regime was found when the PEI content was increased up to 30 wt% for PEI-loaded unimodal porous silicas and 40 wt% for PEI-loaded bimodal porous silicas. At high PEI contents (40–50 wt%), the CO_2 capturing efficiency of the PEI-loaded bimodal porous silicas was found to be considerably greater than that of the PEI-loaded unimodal porous silicas, indicating that most of the amine groups of PEI molecules loaded on the unimodal porous silica supports was useless, and thus the appeared macroporosity of the bimodal porous silica supports could provide a higher effective amine density to adsorb CO_2.

1. Introduction

The global warming caused by greenhouse gases emission has raised serious concerns. Carbon dioxide (CO_2) is considered to be one of the major greenhouse gases directly influencing global climate change and human health, as more than 30 billion tons of

* Department of Chemical Engineering, Faculty of Engineering, Kasetsart University, Bangkok 10900, Thailand. Tel.: +66 2579 2083; fax: +66 2561 4621.
E-mail address: fengttwi@ku.ac.th.

0254-0584/$ – see front matter © 2012 Elsevier B.V. All rights reserved.
http://dx.doi.org/10.1016/j.matchemphys.2012.09.014

anthropogenic CO_2 is annually added to the atmosphere [1]. The drastic rise of CO_2 emission has been attributed to an increasing dependence on the combustion of fossil fuels (coal, petroleum, and natural gas) which account for 86% of anthropogenic greenhouse gas emission [2,3]. A reduction of CO_2 emission can potentially occur as a result of increased energy efficiency [4,5], substitution of non-carbon fuels [6] or by the capture and storage of CO_2 [4,7–10]. With the United Nations' prediction of growth in world population to reach 8.2 billion by 2030, the demand for energy is undoubtedly expected to increase substantially [11], which is certainly to erase any reductions in CO_2 emissions associated with improved energy efficiency. Fossil fuels will continue to be major source of energy for the next few decades due to the scarcity and cost of non-carbon energy sources. Thus, the capture and storage of CO_2 will be called for to allow the utilization of fossil fuels absent of augmentation of CO_2 emission.

The current commercial capture of CO_2, which has been recognized as the most developed process, employs a chemical absorption method with monoethanol amine (MEA) as the sorbent [12]. The chemical interaction between the MEA and the CO_2 molecules is strong and this offers a fast and effective removal of the CO_2 in a single stage of absorption. However, the strong interaction between the MEA and the CO_2 molecules requires significant amounts of energy to regenerate the MEA solution. As the MEA is highly corrosive, costly absorber packing and column materials are used. Finally, the impurities and minor components in the flue gas which comprise SO_2, NO_2, O_2, etc. have to be removed prior to absorption of the gas in order to prevent the degradation of the MEA solution. This requires several pretreatment processes and therefore leads to high capture costs estimated at approximately 59.1$/tonnes of CO_2 avoided [12].

Another advanced technology for CO_2 capture concept is the use of selective membranes which have several advantages over absorption process, e.g., no regeneration energy required, no waste streams. However, membranes cannot always achieve high degrees of separation, which makes multiple stage or recycling necessary [5,13]. Moreover, membranes are susceptible to sulphur compounds and other trace elements [5]. The challenging tasks for membrane technology are to generate driving force without using large compression or vacuum power, provide high CO_2 permeance for large membrane area and maintain effectiveness and lifetime [14].

An adsorption process using porous solids such as activated carbon and zeolites are good candidates for capturing CO_2 from flue gas. However, the low CO_2/N_2 selectivity provides carbon-based materials practical only for CO_2-rich flue gas [15]. Zeolites can offer higher CO_2/N_2 selectivity than those of carbonaceous materials. However, their CO_2 capacities degrade dramatically when water vapor is present in the flue gas [16].

The immobilization of polymer containing amines groups into porous solids, used as a CO_2 capture sorbent, has been an increasingly active area of research because of several significant advantages inclusive potential elimination of corrosion problems and lower energy cost for regeneration. The interaction of CO_2 with amine groups under anhydrous conditions gives rise to the formation of ammonium carbamates through the following reactions [17]:

$$CO_2 + 2RNH_2 \rightarrow RNHCOO^- + RNH_3^+ \quad (1)$$

$$CO_2 + 2R_2NH \rightarrow R_2NCOO^- + R_2NH_2^+ \quad (2)$$

Recently, polyethyleneimine (PEI)-loaded ordered-mesoporous silicas such as MCM-48 [18,19], SBA-15 [18,20–25], SBA-16 [18,26], SBA-12 [20,27], and KIT-6 [18,28] exhibit a high CO_2 capacity in a range of 1.5–3.5 mol kg^{-1} sorbent. These mesoporous silicas can be synthesized by using tetraethyl orthosilicate (TEOS) as a silica source and synthetic polymers as a template. However, these raw materials are fairly expensive and toxic to environment in some extent. Wang et al. [29] describes the cost estimation in utilization of mesoporous silicas, e.g., MCM-41 and SBA-15 as PEI support. They reported that the cost of the support materials accounts for >90% of the total adsorbent preparation cost. Therefore, the use of low-cost raw materials can significantly reduce the cost of the adsorbent preparation.

Rice husk, an abundantly available waste in all rice producing countries, has been recently proven to be potential silica source for the synthesis of porous silica materials [19,21,30–33]. Therefore, the utilization of rice husk as silica source instead of organic silicate compounds can be an efficient eco-friendly route in near future due to the demand from conscientious consumers and strict environmental regulations. Chitosan, the second most abundant biopolymer in nature after cellulose, has attracted great attention to use as a natural template in the synthesis of porous silica material instead of synthetic polymers due to its low cost and non-toxicity. In contrast to synthetic polymers, chitosan cannot form a micelle to act as template for the production of ordered-mesoporous silica materials. However, it plays an important role on the formation of extra-large voids in a range of macropore which provides porous silica materials having two different pore sizes at the same time: a smaller pore formed by an aggregation of silica nanoparticles and a larger pore caused by a removal of chitosan [34,35]. In recent years, bimodal porous silica materials have attracted much attention for use in industrial application such as catalysis and adsorption since the small pore can provide high active surface area while the large pore can improve diffusion efficiency. Ahn et al. [36] have shown recently that the main factors to achieve a high CO_2 sorption capacity are the pore volume and pore size of the support material, not high structural order. Therefore bimodal porous silica might be a good support for the multilayer impregnation of amine and might enhance diffusion of CO_2 in the silica matrix.

In the present study, the bimodal (meso–macro) porous silica materials with different mesopore sizes were prepared and employed as the supports for PEI impregnation. In addition, PEI-loaded unimodal porous silica materials (silica xerogel and SBA-15) with the identical mesopore diameters to bimodal porous silica materials were prepared for purpose of comparison. The properties of the silica supports and PEI-loaded silica supports were characterized by means of N_2-sorption, scanning electron microscopy (SEM), Fourier transform infrared spectroscopy (FT-IR), and thermal gravimetric and derivative thermal gravimetric analysis (TG-DTG). The effects of PEI content and adsorption temperature on the performance of the adsorbents for CO_2 capture were investigated. Moreover, durability test of the selected adsorbent was also conducted with several cycles of adsorption–desorption of CO_2.

2. Experiment

2.1. Porous silica materials preparation

Rice husk ash derived sodium silicate ($Na_2Si_3O_7$: 30 wt.% SiO_2; 4 wt.% NaOH) was prepared by dissolving rice husk ash (99.7 wt.% SiO_2) in NaOH solution. The detail of preparation procedures was presented elsewhere [37]. Bimodal porous silicas were prepared using sodium silicate and chitosan as a natural template. In a typical synthesis, 0.4 g chitosan was dissolved in 100 ml of 1% v/v acetic acid in deionized water at room temperature. Then, 5.5 g of sodium silicate solution (30 wt.% SiO_2) was primarily diluted with 10 ml deionized water and slowly added to the chitosan solution with

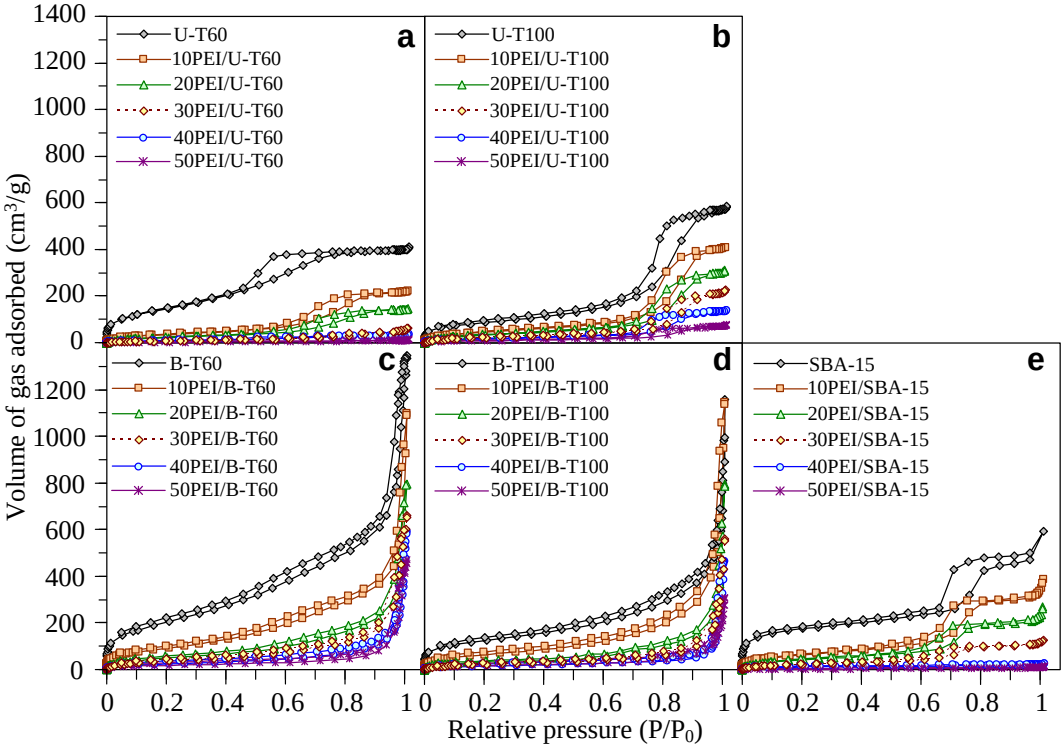

Fig. 1. N_2-sorption isotherms of porous silica supports and PEI-loaded porous silica materials: (a) *Y*PEI/U-T60, (b) *Y*PEI/U-T100, (c) *Y*PEI/B-T60, (d) *Y*PEI/B-T100 and (e) *Y*PEI/SBA-15.

vigorous stirring. The pH of mixture was adjusted to 6. After that, the hydrolysis–condensation reaction was carried out at 40 °C for 3 h, and then the resultant solution was aged in the Teflon-lined autoclave at different temperatures (60 or 100 °C) for 24 h. The solid product was filtered and washed several times with distilled water until the conductivity of the supernatant was below 2.0 μS cm^{-1}. Subsequently, the solid product was dried at 120 °C for 12 h and then calcined at 600 °C for 4 h at a heating rate of 1 °C min^{-1}. The obtained samples are denoted as B-T*x* (*x* = synthesis temperature in °C).

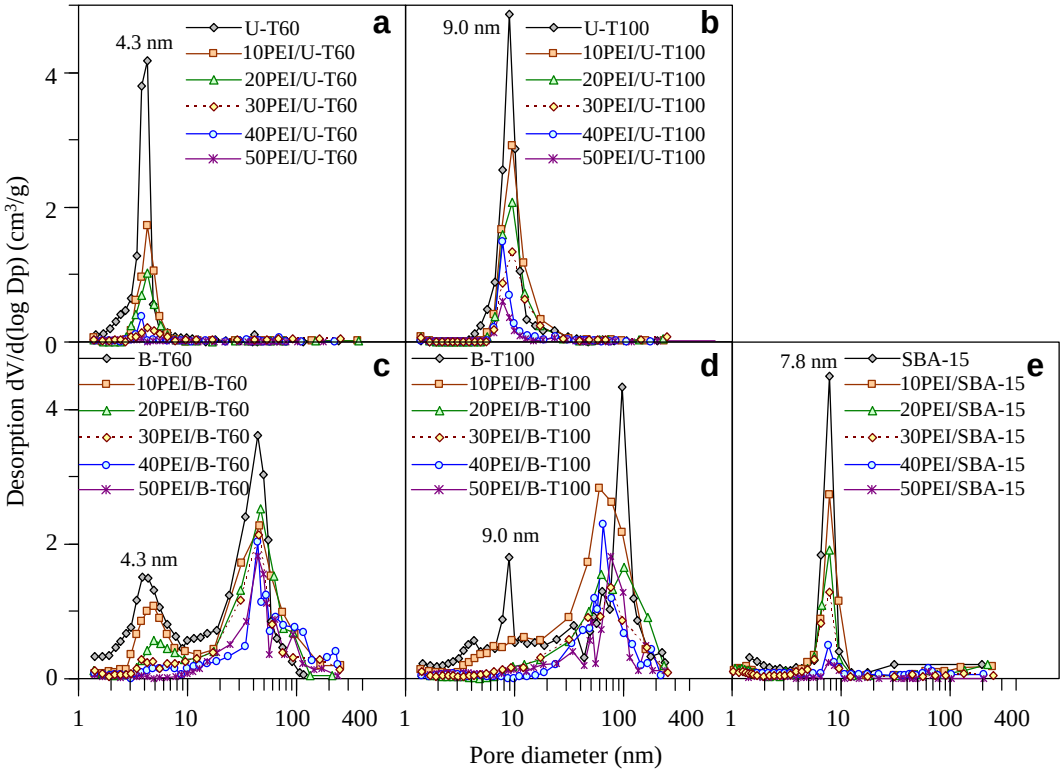

Fig. 2. Pore size distribution of porous silica supports and PEI-loaded porous silica materials: (a) *Y*PEI/U-T60, (b) *Y*PEI/U-T100, (c) *Y*PEI/B-T60, (d) *Y*PEI/B-T100 and (e) *Y*PEI/SBA-15.

Unimodal porous silicas were synthesized using the similar condition for the synthesis of the bimodal porous silicas but without the addition of chitosan. The obtained samples are denoted as U-T*x* (*x* = synthesis temperature in °C).

SBA-15 was synthesized based on the published procedure from Chareonpanich et al. [33,38]. In a typical synthesis, the molar ratio of SiO_2: Pluronic P123: HCl: H_2O of 1: 0.0875: 4: 200 was used because this ratio could provide a highly ordered hexagonal mesoporous silica which was evidently confirmed by small angle X-ray scattering [38] and transmission electron microscopy [33]. In the first step of the procedure, 0.845 g of Pluronic P123 was dissolved in water. Subsequently, rice husk ash derived sodium silicate was slowly added to the Pluronic P123-water solution that was being stirred at 40 °C. HCl was then rapidly added into the solution in order to initiate the hydrolysis–condensation reaction for 24 h. The obtained gel was transferred to a Teflon-lined autoclave in which the hydrothermal aging was taken place at 100 °C for 24 h. The solid product was filtered and washed several times with distilled water until the conductivity of the supernatant was below 2.0 μS cm^{-1}. Subsequently, the solid product was dried at 140 °C for 3 h and then calcined at 550 °C for 6 h.

2.2. PEI impregnation on porous silica materials

PEI-loaded porous silica materials were prepared by impregnation method [39]. First, the desired amount of PEI (Aldrich, $M_w = 600$, b.p. of 250 °C) was dissolved in 6 mL of methanol under stirring for 15 min, and then 0.5 g porous silica support was added to the above solution. The resultant slurry was continuously stirred at room temperature for 3 h to ensure that PEI molecules completely penetrated into pores of the porous silica. Subsequently, the product was then dried at 80 °C for 8 h under reduced pressure (700 mm Hg) to remove the remaining solvent. The obtained products were designated as *Y*PEI/U-T*x*, *Y*PEI/B-T*x* and *Y*PEI/SBA-15, *Y* being the quantity of PEI introduced in weight percentage.

2.3. Characterization

2.3.1. N_2-sorption analysis

The specific surface area, mean pore diameter and pore volume of porous silica materials and PEI-loaded porous silica materials were determined by N_2-sorption analysis with a Quantachrome Autosorb-1C instrument at −196 °C. Prior to each measurement, the porous silica materials and PEI-loaded porous silica materials were degassed at 200 °C and 80 °C (to prevent the decomposition of PEI), respectively for 12 h. The specific surface areas were estimated by using BET method. The pore size distribution of the samples was calculated in accordance with the BJH method. The total pore volume was determined at a relative pressure of 0.99.

2.3.2. Scanning electron microscopy

The morphology of porous silica materials and PEI-loaded porous silica materials was assessed with the application of a scanning electron microscope (SEM; Philips XL30). The SEM was operated at 14.0 kV of an accelerating voltage. The samples were sputter-coated with gold prior to analysis.

2.3.3. Fourier transform infrared spectroscopy

The functional groups on the surface of porous silica materials and PEI-loaded porous silica materials were characterized by means of Fourier transform infrared spectroscopy (FT-IR). FT-IR spectra were obtained with a spectrophotometer (Bruker Tensor 27) in the range of 400–4000 cm^{-1} with a resolution of 4 cm^{-1} without any pretreatment. The sample preparation incorporated the amalgamation of fine powder of each sample with KBr powder.

2.3.4. Thermal gravimetric analysis

The amount of PEI loaded into porous silica materials was investigated with a SDT2960 simultaneous DTA–TGA Universal 2000 in a flow of air, in the temperature range of room temperature to 800 °C at the heating rate of 10 °C min^{-1}. The sample loading was typically 15–20 mg.

2.4. CO_2 adsorption–desorption measurement

CO_2 adsorption–desorption measurements were performed for all PEI-loaded porous silica materials with a SDT2960 simultaneous DTA–TGA Universal 2000. A 15–20 mg sample was loaded into an alumina sample pan. Prior to any CO_2 adsorption–desorption experiment and to remove pre-adsorbed CO_2 and H_2O, the sample was first activated by heating it from room temperature in a flow of pure Ar (100 mL min^{-1}) at a rate of 10 °C min^{-1} until 110 °C was achieved and kept constant for 30 min, then the sample was cooled to a given temperature (60, 75, 85, 90, 95 and 105 °C). Once the adsorption temperature was reached and stabilized, pure CO_2 (99.999%) with a flow rate of 100 mL min^{-1} was introduced into the system while the change in the sample weight was being recorded. In some case, 14% CO_2 (N_2 as balance gas) was carried out instead of pure CO_2. After the adsorption for 40 min, the CO_2 flow was disconnected and the Ar flow was subsequently introduced. The sample were heated to 110 °C at a rate of 10 °C min^{-1} and kept constant for 100 min to desorb CO_2. The identical experiment was repeated twenty-fold in order to investigate the reversible and stable CO_2 adsorption–desorption.

Table 1
Textural properties of porous silica materials and PEI-loaded porous silica materials.

Samples	BET surface area (m^2 g^{-1})	BJH mean pore diameter (nm)	Mesopore volume[a] (cm^3 g^{-1})	Macropore volume[b] (cm^3 g^{-1})
U-T60	552	4.3	0.63	0.01
10PEI/U-T60	136	4.3	0.34	0.01
20PEI/U-T60	91	4.3	0.23	0.01
30PEI/U-T60	42	3.8	0.10	0.01
40PEI/U-T60	32	3.8	0.05	0.01
50PEI/U-T60	8	3.8	0.02	0.01
U-T100	314	9.0	0.87	0.03
10PEI/U-T100	177	9.0	0.62	0.02
20PEI/U-T100	132	9.0	0.40	0.02
30PEI/U-T100	86	9.0	0.33	0.02
40PEI/U-T100	67	7.8	0.21	0.02
50PEI/U-T100	36	7.8	0.11	0.02
SBA-15	570	7.8	0.73	0.19
10PEI/SBA-15	235	7.8	0.54	0.06
20PEI/SBA-15	170	7.8	0.38	0.04
30PEI/SBA-15	125	7.8	0.35	0.04
40PEI/SBA-15	42	7.6	0.13	0.03
50PEI/SBA-15	12	7.6	0.02	0.02
B-T60	746	4.3 and 43.9	0.88	1.00
10PEI/B-T60	352	4.3 and 45.8	0.75	0.95
20PEI/B-T60	190	4.3 and 46.6	0.40	0.90
30PEI/B-T60	144	45.1	0.18	0.88
40PEI/B-T60	93	44.4	0.10	0.85
50PEI/B-T60	66	44.0	0.02	0.70
B-T100	437	9.0 and 97.8	1.08	0.79
10PEI/B-T100	242	9.0 and 65.0	0.88	0.70
20PEI/B-T100	153	64.8	0.56	0.68
30PEI/B-T100	83	62.0	0.28	0.60
40PEI/B-T100	70	64.2	0.12	0.58
50PEI/B-T100	58	65.1	0.06	0.47

[a] Mesopore volume measured by N_2-sorption at pores smaller than 50 nm in diameter.
[b] Macropore volume measured by N_2-sorption at pores larger than 50 nm in diameter.

3. Results and discussion

3.1. Characterization of porous silica and PEI-loaded porous silica materials

As the characteristics of the pore structure of adsorbents strongly influences the diffusion and reaction of CO_2. The effects of PEI content on the pore structure of adsorbents need to be therefore thoroughly investigated. The isotherms and pore characteristics of all samples measured by N_2-physisorption are shown in Figs. 1 and 2. The physical properties inclusive the BET surface area, BJH mean pore diameter, mesopore volume and macropore volume are given in Table 1. As shown in Fig. 1, the isotherm of unimodal porous silica materials (Fig. 1a and b) was type IV with H2 hysteresis loop

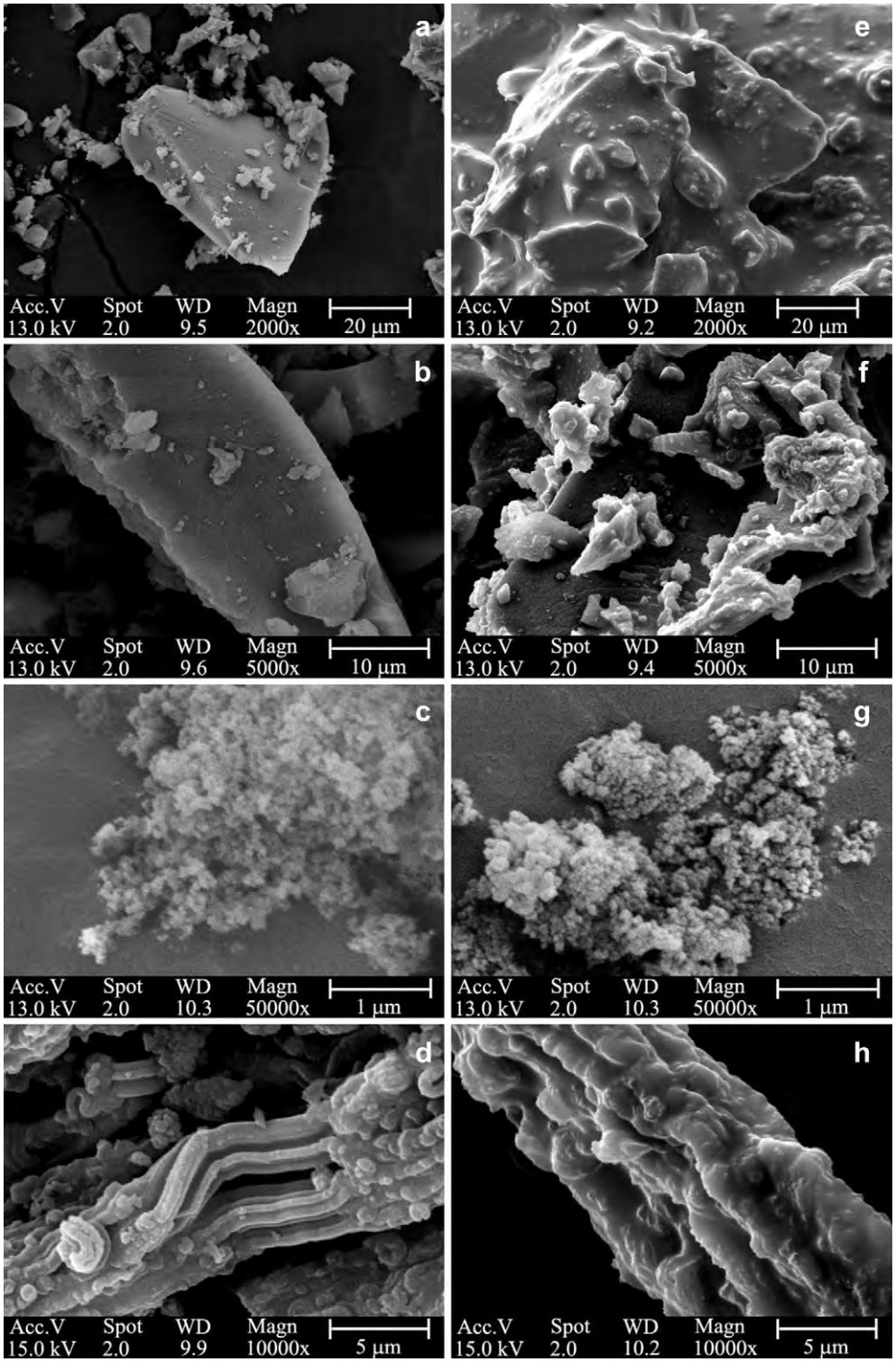

Fig. 3. SEM images of representative porous silica materials: (a) U-T60, (b) U-T100, (c) B-T100 and (d) SBA-15; and PEI-loaded porous silica materials (e) 50PEI/U-T60, (f) 50PEI/U-T100, (g) 50PEI/B-T100 and (h) 50PEI/SBA-15.

which was a characteristic of mesoporous material with ink-bottle structure. It can be seen that the hysteresis loop shifted to higher relative pressures when increasing reaction temperature from 60 °C to 100 °C, implying the increase in the mean pore size of porous silica materials. With chitosan template (Fig. 1c and d) the isotherms (B-T60 and B-T100) exhibited two adsorption steps. The first adsorption step ($P/P_0 < 0.9$) was a characteristic of type IV isotherm, representing the existence of the capillary condensation of nitrogen gas inside the inter-particle mesopores. Similar to the products synthesized without the template, the hysteresis loop also shifted to a higher relative pressure when increasing the reaction temperature. The second adsorption step at a high relative pressure ($P/P_0 > 0.9$) was a characteristic of type II isotherm, corresponding to the adsorption of liquid nitrogen on the large inter-particle voids or macropores. The isotherm of SBA-15 sample (Fig. 1e) displayed a type IV isotherm with H1 hysteresis, an indication of mesopore with cylindrical structure.

The amount of gas adsorbed of each sample was found to be decreased with increasing the amount of PEI content, an indication of monolayer to multilayer deposition of PEI. At 40 wt% PEI content, the isotherm of the PEI-loaded unimodal porous silica materials (40PEI/U-T60 and 40PEI/SBA-15) was found to be almost parallel to the *x*-axis, which revealed an absence of multilayer gas adsorption. Although the pore structure of the 40PEI/U-T100 was identical to that of the 40PEI/U-T60, some voids were found to be present within the structure of the 40PEI/U-T100 as confirmed by multilayer gas adsorption at a high relative pressure. This observation is an indication for the PEI loading capacity of each porous silica material only to depend on pore volume absent of a significant contribution of the presence of ordered pore structure (SBA-15). The amount of gas adsorbed of the PEI-loaded bimodal porous silica materials (Fig. 1c and d) was determined to be decreased with increasing PEI content at a relative pressure lower than 0.9, which was similar to that of the PEI-loaded unimodal porous silica materials. However, at high PEI content (40–50 wt%), the large amount of gas adsorbed of the PEI-loaded bimodal porous silica materials was observed at a relative pressure higher than 0.9, which suggests the existence of numerous macropores.

The pore size distributions of all samples calculated with the BJH method are shown in Fig. 2. The pore size distribution of the U-T60, U-T100 and SBA-15 was found to be of unimodal size, with denotes pore diameters of 4.3 nm, 9.0 nm and 7.8 nm, respectively. Subsequent to PEI impregnation at higher 30 wt%, the mean pore size of the U-T60 and U-T100 was established to have shifted to smaller pore sizes with the volume of those pores significantly decreased. The pore size distribution of the B-T60 and B-T100 displayed the bimodal pore size distribution in the range of mesopore and macropore regions. The mesopores were formed by the aggregates of silica nanoparticles which were similar to those of the unimodal porous silica material, whereas the macropores were obtained by the aggregates of the silica domain [35]. Although the mesopore volume of the bimodal porous silica supports was larger than that of the unimodal porous silica supports (Table 1), the mesopores of all PEI-loaded bimodal porous silica supports was found to be completely disappeared. This observation is indication for the inaccessibility of nitrogen gas into the mesopores due to the pore blockage caused by PEI agglomeration on the external surface of silica domain. The aforementioned observations are consistent with the results in Table 1. It can be seen that, at 50 wt% PEI loading, the macropore volume of 50PEI/B-T60 and 50PEI/B-T100 was found to be decreased 30% and 40%, respectively compared to that of the pristine silica. However, the macropore volume of the 50PEI/B-T60 was found to be 35 times larger than that of the 50PEI/U-T60.

Fig. 3 shows the SEM images of representative porous silica materials (Fig. 3a–d) and PEI-loaded porous silica materials (Fig. 3e–h). The morphology of unimodal porous silica materials (Fig. 3a and b) showed the dense aggregation of fine silica nanoparticles while that of bimodal porous silica (Fig. 3c) exhibited loosely packed aggregates of silica domains with the inter-particle voids (macroporosity). The morphology of SBA-15 (Fig. 3d) consisted ca. 5 μm of long rod-shaped particles aggregated into bundles. After PEI loading, the agglomeration of PEI on the external surface was observed for 50PEI/U-T60 (Fig. 3e), 50PEI/U-T100 (Fig. 3f) and 50PEI/SBA-15 (Fig. 3h) samples. In addition, the external surface of 50PEI/U-T60 was found to be fully coated with PEI while that of 50PEI/U-T100 and 50PEI/SBA-15 was coated partially. This should be because the loading amount of PEI was in excess of the maximum uptake capacity of the supports with small pore volume (U-T60; Table 1). In contrast, SEM image of 50PEI/B-T100 sample (Fig. 3g) showed many large external voids (macropores) between the silica domains.

The FT-IR spectroscopy is employed to provide direct identification of chemical groups in porous silica materials and PEI-loaded porous silica materials. The FT-IR spectra of representative porous silica materials and PEI-loaded porous silica materials are shown in Fig. 4. The strong band around 1100 cm^{-1} and small bands around 800 and 462 cm^{-1} represented the characteristics of Si–O–Si groups. The shoulder at 966 cm^{-1} indicated the existence of residual silanol groups, resulting from a stretching motion of oxygen atoms not bridging to two Si atoms, attributing to Si–O– and Si–OH vibrations. The broad transmission band at approximately 3430 cm^{-1} could be attributed to the OH stretching vibration from residual water. The band appeared at 1624 cm^{-1} was attributed to adsorbed water. The FT-TR spectra of unimodal and bimodal porous silica materials appeared at the identical wave numbers, an indication for the nearly identical chemical nature of both silica materials. However, the intensity of the band (966 cm^{-1}) related to the existence of silanol content of the bimodal porous silica material was shaper than that of the unimodal porous silica material, indicating that a higher number of silanol groups existed on the surface of bimodal porous silica.

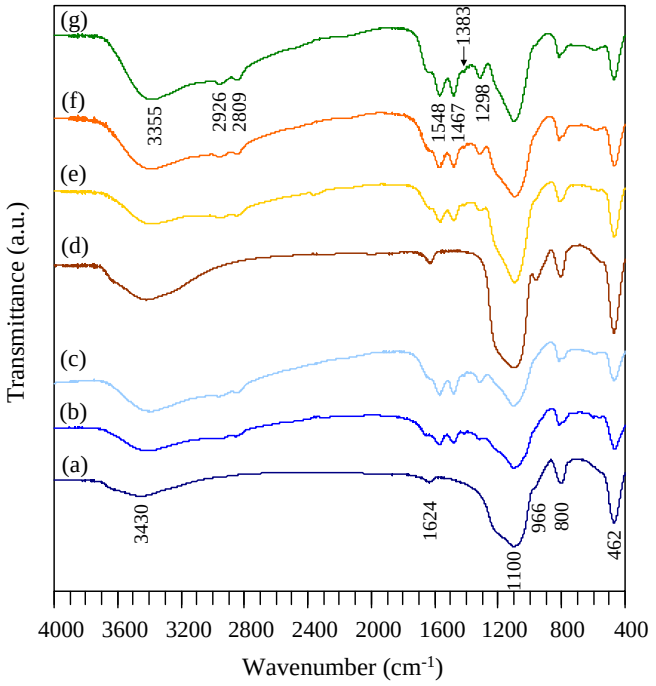

Fig. 4. FT-IR spectra of porous silica materials and PEI-loaded bimodal porous silica materials: (a) U-T100, (b) 40PEI/U-T100, (c) 50PEI/U-T100, (d) B-T100, (e) 40PEI/B-T100, (f) 50PEI/B-T100 and (g) 60PEI/B-T100.

PEI-modification of porous silica materials was confirmed by a new band at around 1548 cm^{-1} and 1467 cm^{-1}, representing the asymmetric and symmetric bending of NH_2 groups, respectively. Two bands appeared at 2809 and 2926 cm^{-1}, which could be characteristics of CH_2 stretching modes of the PEI chains. The broad band around 3355 cm^{-1} could be attributed to the amine N–H stretching vibrations. In addition, the bands corresponding to the silanol content (966 cm^{-1}) and OH stretching vibration (3430 cm^{-1}) were not observed in the IR spectra of the PEI-loaded bimodal porous silica materials, indicating that the residual silanol group of bimodal porous silica could possibly react with the amine group of PEI.

The characteristics of pristine PEI decomposition were analyzed by means of TG and DTG as shown in Fig. 5a and b, respectively. It can be seen that the pristine PEI lost ca. 2% at temperature lower than 100 °C, which can be ascribed to the desorption of CO_2 and moisture [39]. The PEI began to melt around 175 °C, evidenced by the endothermic peak from differential thermal analysis (not

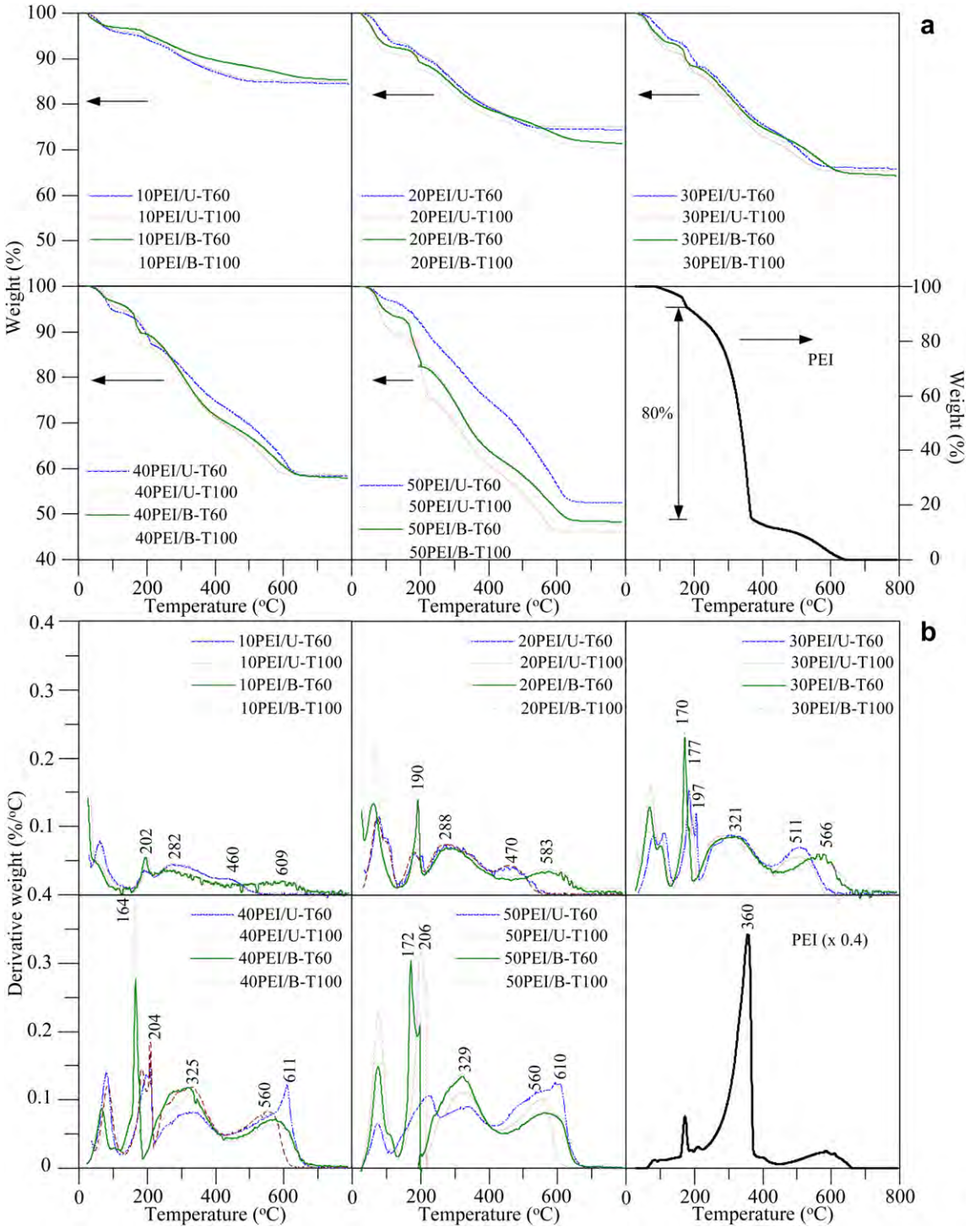

Fig. 5. TG (a) and DTG profiles (b) of all sorbents and pristine PEI.

shown here). A sharp weight loss ca. 80% appeared from 200 to 400 °C and the maximum rate of weight loss was found at 360 °C. At above 400 °C, the residue carbon was continuously decomposed and was removed completely at temperature around 600 °C.

The TG and DTG patterns of the adsorbents prepared at different amounts of PEI content are also included in Fig. 5a and b, respectively. There were four steps of weight losses. The first steps at a temperature below 100 °C could be due to the desorption of CO_2 and moisture which was similar to that of the pristine PEI. The PEI molecules deposited at different positions of the porous silica materials could be decomposed at different temperature ranges due to the influence of heat and mass transfer. Consequently, the distribution of the PEI molecules at the macropores or the outermost surface of the silica particles and into the pores (mesopores) could be decomposed at 160–210 °C and 210–400 °C, respectively. The last step at the range of 400–600 °C could be attributed to the decomposition of PEI reacted with silanol groups of the porous silica materials.

At low PEI content (10 wt%), the intensity for the second peak of 10PEI/B-T60 and 10PEI/B-T100 was found to be higher than that of 10PEI/U-T60 and 10PEI/U-T100. This indicated that the PEI-loaded bimodal porous silicas were possibly distributed both on mesopores and macropores, even though very low amount of PEI was applied. This peak position of PEI-loaded bimodal porous silicas was established to have shifted toward lower temperature when the PEI content was increased from 10% to 40%. This observation could be explained by the fact that the monolayer deposition of PEI occur at low PEI content, resulting in a strong interaction between the PEI molecules and the surface of the supports. With a yet higher PEI content, the monolayer deposition no longer occurred and instead a multilayer deposition of PEI was formed which was decomposed easier than the monolayer deposition of PEI. However, at 50 wt% PEI content, this peak slightly shifted toward higher temperature from 164 to 172 °C which indicated that the increase of multilayer to a certain number caused the formation of PEI clusters behaved like the pristine PEI. The similar trends were also observed for PEI-loaded unimodal porous silica. However, the deposition of PEI clusters could be found by using only 30 wt% PEI content.

In contrast to the position for the second peak, the position for the third peak of all adsorbents was established to have shifted toward higher temperature when the PEI content was increased from 10% to 50%. This could be explained by the fact that the PEI clusters cannot be formed since they were limited by the size of mesopores (4.3–10 nm), and therefore the decomposition of PEI within the mesopores was only affected by heat and mass transfer. Note that the temperature for PEI decomposition at the last step of 10PEI/B-T60 and 10PEI/B-T100 was found to be higher than that of 10PEI/U-T60 and 10PEI/U-T100. This might be attributed to the larger amount of silanol group of pristine bimodal porous silica materials as confirmed by FTIR. A schematic diagram presented the effect of the unimodal and bimodal porous silica supports on PEI deposition is shown in Fig. 6.

The total weight losses of 10PEI/U-T60, 10PEI/U-T100, 10PEI/B-T60 and 10PEI/B-T100 were found to be 15.5%, 15.1%, 14.7% and 14.7%, respectively. If the weight losses due to the desorption of CO_2 and moisture were subtracted from the total weight, the loading amount of PEI on all samples could be calculated to be approximately 10 wt%. This result confirmed that virtually identical amounts of PEI were loaded into the porous silica materials and apparently no PEI loss during the impregnation process. The similar trends were also observed at the other percentages of PEI.

3.2. CO_2 sorption performance

Fig. 7 shows the effects of adsorption temperature and loading amount of PEI on CO_2 capture capacity all adsorbents in units of mg CO_2/g sorbent (Fig. 7a) and mg CO_2/g PEI (Fig. 7b). At low PEI content (10–20 wt%), the CO_2 capturing capacity of the adsorbents with the unimodal pore size was found to be decreased with the increase of adsorption temperature since the CO_2 adsorption is an exothermic process (Van't Hoff behavior), favored at low adsorption temperature. When the PEI content was increased to 30 wt%, the CO_2 adsorption capacity of the adsorbents with small mesopores size (30PEI/U-T60 and 30PEI/SBA-15) first increased and then decreased with increasing temperature, which was indicative for a transition between a kinetically controlled regime (60–90 °C) and a thermodynamically controlled regime (90–105 °C). With a yet higher PEI content (40 wt%), the thermodynamically controlled regime was no longer observed and the kinetically controlled regime was found instead, which is an indication of a strong diffusion limitation on CO_2 adsorption, resulting in a non-intuitive functional dependence of the CO_2 adsorption with the temperature (inverse Van't Hoff behavior). At 50 wt% PEI content, the CO_2 sorption capacity dramatically decreased at all adsorption temperature when compared to that of 40 wt% PEI content. Based on the results of SEM images (Fig. 3), PEI molecules were coated on

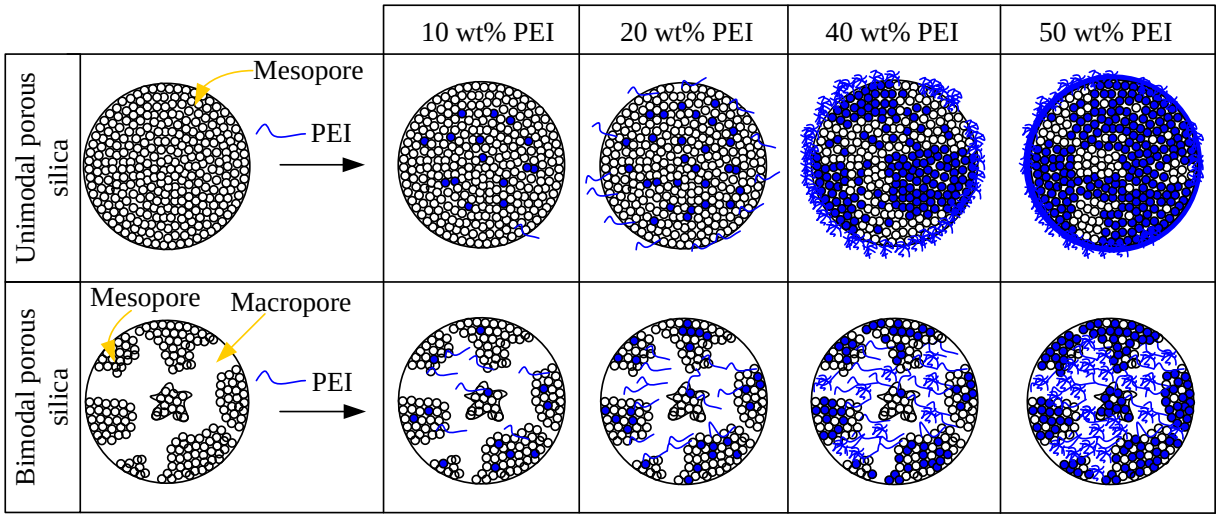

Fig. 6. Schematic diagram presented the effect of supports on PEI deposition.

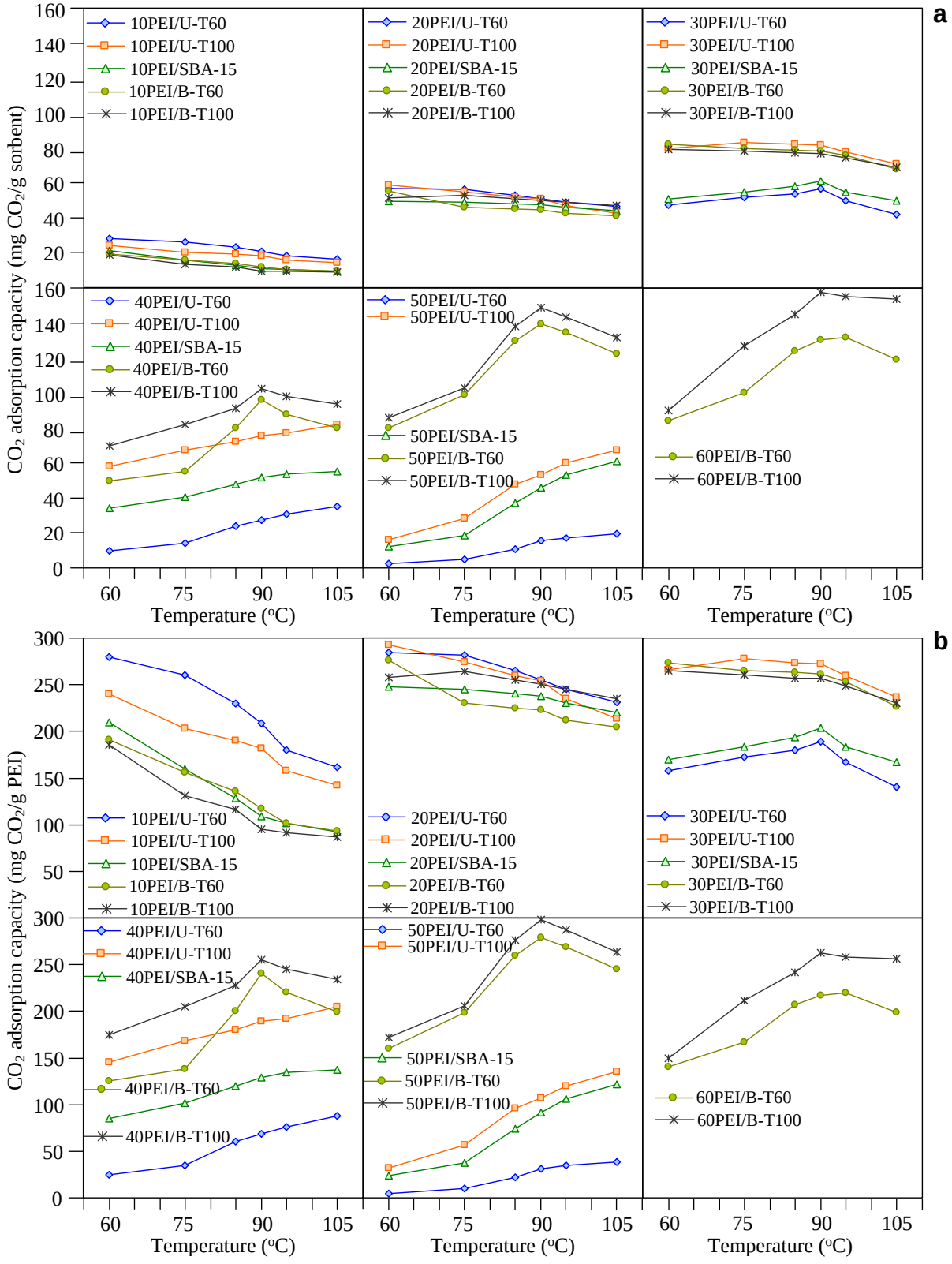

Fig. 7. CO_2 sorption performance of all sorbents in unit of (a) mg CO_2/g sorbent and (b) mg CO_2/g PEI.

the outer surface of the unimodal porous silica material. Therefore only PEI on the external surface could potentially adsorb CO_2. With increasing adsorption temperature, the PEI molecules became flexible which provide the available pore space for CO_2 to expose amino groups of PEI in the pores [40]. The increasing PEI loading up to 50 wt% leaded to a formation of thicker polymer film fully coated on the silica particles. The result indicated that the sorption of CO_2 over PEI-loaded unimodal porous silica was strongly dominated by

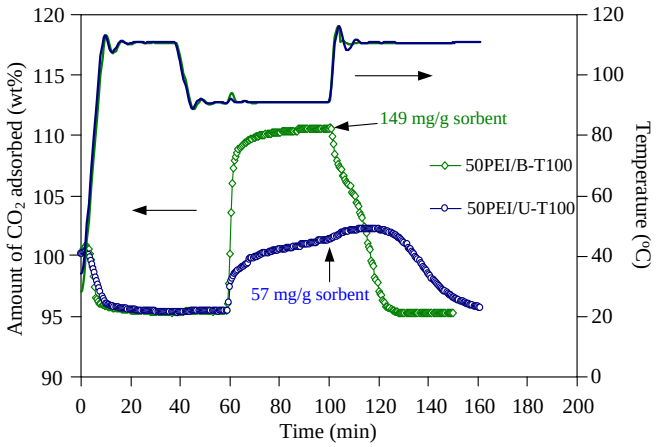

Fig. 8. CO_2 adsorption–desorption behavior of 50PEI/U-T100 and 50PEI/B-T100.

the kinetic diffusion rather than the thermodynamic factor. It is also demonstrated that the supports with small pore volume and very long rod-shaped particles such as U-T60 and SBA-15 were not suitable for PEI loading since only small amount of PEI could effectively load into the pore. Once the pore blockage occurred, CO_2 was hard to diffuse into the pores, resulting in the useless of PEI impregnated in the pores.

The CO_2 sorption capacity of bimodal adsorbent prepared at 10 wt% PEI was found to be slightly lower than that of unimodal adsorbent at identical PEI content (Fig. 7a.), and their capacities in term of mg CO_2/g PEI (Fig. 7b) revealed that the PEI molecules deposited into the unimodal porous silica materials were more efficient for CO_2 capture. However, the opposite results were found when the amount of PEI content was increased (40–50 wt%). The maximum capturing efficiency (298 mg CO_2/g EPI) of 20PEI/U-T100 was found to be identical to that of 50PEI/B-T100. However, the maximum CO_2 sorption capacity per grams of 50PEI/B-T100 (149 mg g^{-1} sorbent) was found to be considerably greater than that of 20PEI/U-T100 (59 mg g^{-1} sorbent). The question is that which one is better to be used as the adsorbent. If the PEI-loaded unimodal porous silica is selected based on the capturing efficiency, the larger size of reactor is required to obtain the identical adsorption capacity. It seems to be that one of criteria for adsorbent selection should be based on the CO_2 adsorption capacity not the capturing efficiency. However, in comparison to the CO_2 adsorption capacity and capturing efficiency of 50PEI/B-T100 and 60 PEI/B-T100, the CO_2 adsorption capacity of 50PEI/B-T100 (149 mg g^{-1} sorbent) was found to be slightly lower than that of 60PEI/B-T100 (154 mg g^{-1} sorbent) whereas the CO_2 capturing efficiency of 50PEI/B-T100 was significantly larger (298 mg g^{-1} PEI) than that of 60PEI/B-T100 (257 mg g^{-1} PEI). In this case, 50PEI/B-T100 should be selected as the adsorbent. Therefore, both terms (mg CO_2/g sorbent and mg CO_2/g PEI) should be considered together to obtain the optimum condition.

Fig. 8 shows the changes in mass during the adsorption and desorption of CO_2 over 50PEI/U-T100 and 50PEI/B-T100 at 90 °C and 1 atm. The equilibrium CO_2 adsorption capacity of 50PEI/B-T100 was found to be 149 mg g^{-1} sorbent, which was established to be 261% more effective than that of 50PEI/U-T100. It is also shown that the CO_2 adsorption over 50PEI/B-T100 was much faster than that over 50PEI/U-T100. The CO_2 adsorption capacity of 50PEI/B-T100 reached ca. 95% of its equilibrium capacity within first 25 min of CO_2 exposure while took 35 min for 50PEI/U-T100. Regarding the desorption process (100 min), the CO_2 is desorbed at 110 °C with purging Ar gas. It can be seen that the mass of 50PEI/B-T100 is immediately decreased while that of 50PEI/U-T100 is first increased, and then gradually decreased. The regeneration time of CO_2 adsorbed on 50PEI/B-T100 was two times faster than that adsorbed on 50PEI/U-T100. The schematic diagram presented the effect of pore structure on PEI loading and CO_2 adsorption has been proposed (Fig. 9). The existence of macropore not only enhances the PEI loading inside the mesopores but also promotes the diffusion of CO_2. Since the silica domain of the bimodal porous silica is much smaller than that of the unimodal porous silica, the CO_2 can diffuse thoroughly the silica domain of the bimodal porous silica. Therefore, PEI impregnated into mesopores of the bimodal porous silica can effectively react with CO_2.

The adsorption–desorption performance of PEI-loaded bimodal porous silica (50PEI/B-T100) is the most important criterion to determine whether bimodal porous silica can be a suitable support material for PEI loading. In order to assess a real practical implementation of this material, the CO_2 adsorption–desorption using 14% CO_2 in a gas mixture of CO_2 and N_2 was also conducted (Fig. 10). The CO_2 adsorption capacity at low CO_2 partial pressure was found to be smaller than that using 100% CO_2 due to a smaller driving

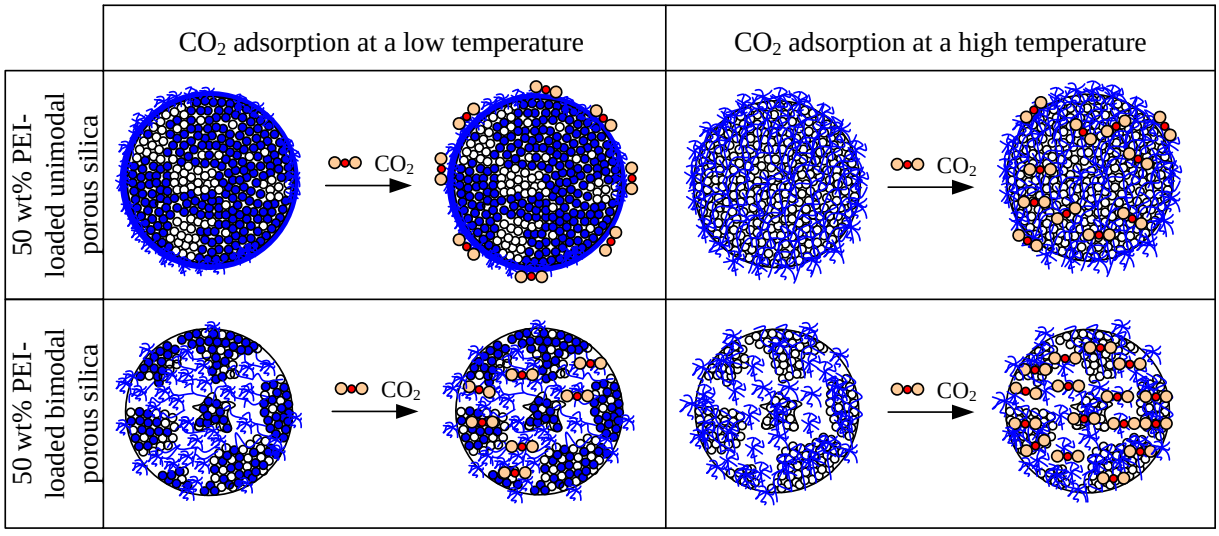

Fig. 9. Schematic diagram presented the effect of pore structure on PEI loading and CO_2 adsorption.

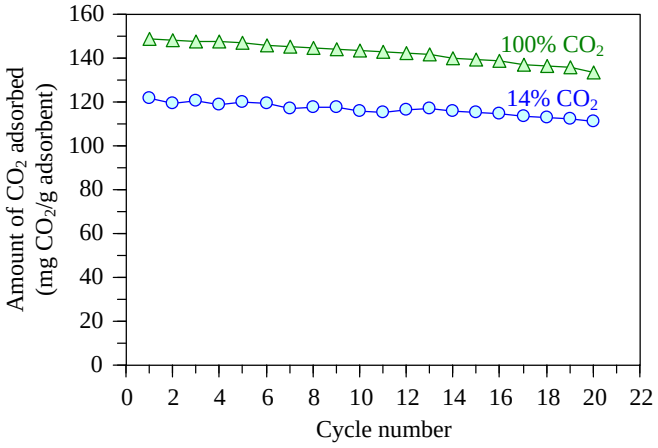

Fig. 10. Recycle runs of CO_2 adsorbed on 50PEI/B-T100 using 100% CO_2 and 14% CO_2.

force [41]. However, during twenty repeated adsorption–desorption cycles, the 50PEI/B-T100 exhibited a stable cyclic adsorption–desorption performance with only a minor drop in its capturing capacity for both 100% CO_2 and 14% CO_2 systems. This result confirmed that most of the amine groups of PEI molecules, which was deposited into the bimodal porous silica, can be recovered completely.

4. Conclusion

The purpose of this paper is to investigate the effects of the bimodal porous silica supports and PEI contents on CO_2 sorption capacity at different adsorption temperatures.

At low PEI content (10–20 wt%), the CO_2 sorption capacity of PEI-loaded unimodal porous silicas is found to be slightly higher than that of PEI-loaded bimodal porous silicas. However, when the diffusion is the rate-determining step (30–50 wt% PEI), the PEI-loaded bimodal porous silicas have proven to provide higher effective amine density to adsorb CO_2. This is because the existence of macropores and the smaller size of silica domain of the bimodal porous silica supports enhances the accessibility of PEI inside the mesopores and also promotes the diffusion of CO_2. This finding indicates that the PEI-loaded bimodal porous silica materials constitutes a feasible option as a CO_2 sorbent due to its potentially low costs, environmentally benign nature and elevated CO_2 capture capacity.

Acknowledgements

This work was financially supported by the Research, Development and Engineering (RD&E) fund through The National Nanotechnology Center (NANOTEC), The National Science and Technology Development Agency (NSTDA), Thailand (P-12-01200) to Kasetsart University. The author would like to thank the partial support from the National Center of Excellence for Petroleum, Petrochemical and Advanced Materials (NCE-PPAM), the Thailand Research Fund (Grant No. MRG5480196), and the "National Research University Project of Thailand (NRU)". Support from the Kasetsart University Research and Development Institute (KURDI) is also acknowledged.

References

[1] P. Friedlingstein, R.A. Houghton, G. Marland, J. Hackler, T.A. Boden, T.J. Conway, J.G. Canadell, M.R. Raupach, P. Ciais, C.L. Quéré, Nat. Geosci. 3 (2010) 811–812.
[2] B. Metz, O. Davidson, H. de Coninck, M. Loos, L. Meyer, Intergovernmental Panel on Climate Change. Special Report on Carbon Dioixde Capture and Storage, Cambridge University Press, Cambridge, 2005, http://www.ipcc.ch/.
[3] D.M. D'Alessandro, B. Smit, J. Long, Angew. Chem. Int. Ed. 49 (2010) 6058–6082.
[4] J.A. Moya, N. Pardo, A. Mercier, J. Clean. Prod. 19 (2011) 1207–1215.
[5] A.A. Olajire, Energy 35 (2010) 2610–2628.
[6] M.D. Lorenzo, K. Scott, T.P. Curtis, I.M. Head, Chem. Eng. J. 156 (2010) 40–48.
[7] L. Peters, A. Hussain, M. Follmann, T. Melin, M.-B. Hägg, Chem. Eng. J. 172 (2011) 952–960.
[8] X. Yan, Y. Zhang, K. Qiao, X. Li, Z. Zhang, Z. Yan, S. Lomarneni, J. Hazard. Mater. 192 (2011) 1505–1508.
[9] C.C. Dean, J. Blamey, N.H. Florin, M.J. Al-Jeboori, P.S. Fennell, Chem. Eng. Res. Des. 89 (2011) 836–855.
[10] T. Witoon, Ceram. Int. 37 (2011) 3291–3298.
[11] World Nuclear Association (WNA). Available at: www.world-nuclear.org/info/inf16.html, 2011 (accessed 07.05.11).
[12] A.B. Rao, E.S. Rubin, Environ. Sci. Technol. 36 (2002) 4467–4475.
[13] E. Favre, Chem. Eng. J. 171 (2011) 782–793.
[14] T. Merkel, X. Wei, Z. He, K. Amo, B. Firat, S. White, R. Baker, S. Pande, J. Kaschemekat, Pilot test of an efficient membrane process for post-combustion CO2 capture, NETL CO2 capture technology meeting. Available at: <www.netl.doe.gov/publications/proceedings/11/co2capture/presentations/1-Monday/22Aug11-Merkel-MTR-Efficient%20Membrane%20Pilot%20Test.pdf>, 2011 (accessed 24.07.12).
[15] M. Radosz, X.D. Hu, K. Krutkramelis, Y.Q. Shen, Ind. Eng. Chem. Res. 47 (2008) 3783–3794.
[16] S. Choi, J.H. Drese, C.W. Jones, Chem. Sustain. Chem. 2 (2009) 796–854.
[17] F.-Y. Chang, K.-J. Chao, H.-H. Cheng, C.-S. Tan, Sep. Pur. Technol. 70 (2009) 87–95.
[18] W.-J. Son, J.-S. Choi, W.-S. Ahn, Micropor. Mesopor. Mater. 113 (2008) 31–40.
[19] H.T. Jang, Y.K. Park, Y.S. Ko, J.Y. Lee, B. Margandan, Int. J. Greenhouse Gas Control 3 (2009) 545–549.
[20] V. Zeleňák, M. Badaničová, D. Halamová, J. Čejka, A. Zukal, N. Murafa, G. Goerigk, Chem. Eng. J. 144 (2008) 336–342.
[21] M. Bhagiyalakshmi, R. Anuradha, S.D. Park, H.T. Jang, Micropor. Mesopor. Mater. 131 (2010) 265–273.
[22] A. Heydari-Gorji, Y. Yang, A. Sayari, Energy Fuels 25 (2011) 4206–4210.
[23] S. Hao, H. Chang, Q. Xiao, Y. Zhong, W. Zhu, J. Phys. Chem. C 115 (2011) 12873–12882.
[24] G. Calleja, R. Sanz, A. Arencibia, E.S. Sanz-Pérez, Top. Catal. 54 (2011) 135–145.
[25] R. Sanz, G. Calleja, A. Arencibia, E.S. Sanz-Pérez, Appl. Surf. Sci. 256 (2010) 5323–5328.
[26] J. Wei, J. Shi, H. Pan, W. Zhao, Q. Ye, Y. Shi, Micropor. Mesopor. Mater. 116 (2008) 394–399.
[27] V. Zelenak, D. Halamova, L. Gaberova, E. Bloch, P. Llewellyn, Micropor. Mesopor. Mater. 116 (2008) 358–364.
[28] Y. Liu, J. Shi, J. Chen, Q. Ye, H. Pan, Z. Shao, Y. Shi, Micropor. Mesopor. Mater. 134 (2010) 16–21.
[29] D. Wang, C. Sentorum-Shalaby, X. Ma, C. Song, Energy Fuels 25 (2011) 456–458.
[30] M. Bhagiyalakshmi, L.J. Yun, R. Anuradha, H.T. Jang, J. Hazard. Mater. 175 (2010) 928–938.
[31] Y. Liu, Y. Guo, Y. Zhu, D. An, W. Gao, Z. Wang, Y. Ma, Z. Wang, J. Hazard. Mater. 186 (2011) 1314–1319.
[32] T. Witoon, M. Chareonpanich, J. Limtrakul, Mater. Lett. 62 (2008) 1476–1479.
[33] M. Chareonpanich, A. Nanta-ngern, J. Limtrakul, Mater. Lett. 61 (2007) 5153–5156.
[34] T. Witoon, M. Chareonpanich, J. Limtrakul, J. Sol–Gel Sci. Technol. 51 (2009) 146–152.
[35] T. Witoon, M. Chareonpanich, J. Limtrakul, J. Sol–Gel Sci. Technol. 56 (2010) 270–277.
[36] C. Chen, K.-S. You, J.-W. Ahn, W.-S. Ahn, Korean J. Chem. Eng. 27 (2010) 1010–1014.
[37] M. Chareonpanich, T. Namto, P. Kongkachuichay, J. Limtrakul, Fuel Process. Technol. 85 (2004) 1623–1634.
[38] O. Jullaphan, T. Witoon, M. Chareonpanich, Mater. Lett. 63 (2009) 1303–1306.
[39] X. Xu, C. Song, J.M. Andrésen, B.G. Miller, A.W. Scaroni, Micropor. Mesopor. Mater. 62 (2003) 29–45.
[40] C. Chao, W.-S. Ahn, Chem. Eng. J. 166 (2011) 646–651.
[41] A. Heydari-Gorji, A. Sayari, Chem. Eng. J. 173 (2011) 72–79.

Available online at www.sciencedirect.com

SciVerse ScienceDirect

Ceramics International 38 (2012) 5999–6007

CERAMICS INTERNATIONAL

www.elsevier.com/locate/ceramint

Interaction of chitosan with tetraethyl orthosilicate on the formation of silica nanoparticles: Effect of pH and chitosan concentration

Thongthai Witoon [a,b,*], Metta Chareonpanich [a,b]

[a] National Center of Excellence for Petroleum, Petrochemicals and Advance Material, Department of Chemical Engineering, Faculty of Engineering, Kasetsart University, Bangkok 10900, Thailand

[b] Center for Advanced Studies in Nanotechnology and Its Applications in Chemical Food and Agricultural Industries, Kasetsart University, Bangkok 10900, Thailand

Received 5 March 2012; received in revised form 5 April 2012; accepted 18 April 2012
Available online 26 April 2012

Abstract

In this paper, we report the interaction of chitosan with tetraethyl orthosilicate on the formation of silica nanoparticles under different conditions of pH (5–9) and chitosan concentration (0–0.001379 mM). The silica nanoparticles were characterized by means of N_2-sorption, scanning electron microscopy and transmission electron microscopy. It was found that chitosan played two different roles on the formation of silica nanoparticles, depending on the pH values. At a low chitosan concentration, chitosan promoted the formation of larger silica nanoparticles in the pH range of 5–6, while it reduced the size of silica nanoparticles when the pH value was increased to the range of 6.5–8.5. However, based on the results of N_2-sorption analysis, two different sizes of silica nanoparticles caused by the growth of silica at different phases were observed. At high chitosan concentration, the size of silica nanoparticles continuously increased in the pH range of 5–6, while only smaller size of silica nanoparticles was obtained in the pH range of 6.5–8.5. At pH 9, chitosan molecules were found to have no significant effect on the formation of silica nanoparticles even though a large amount of chitosan was employed.

Keywords: A. Powder: chemical preparation; B. Porosity; D. SiO_2; Chitosan

1. Introduction

Silica materials have attracted much attention from researchers because of their commercial applications as catalyst supports, in controlled drug release, and as sorbents [1–3]. Over the past two decades, there has been an increasing interest in the synthesis of various porous silicas by using organic materials as additives in order to fully control the entire pore system as it ranges from micropores to macropores. Recently, several kinds of biopolymer containing amine functionalities have attracted much interest for the synthesis of silica materials because they enable the formation of silica nanoparticles under environmentally friendly conditions, and moreover, silica can possibly mimic their morphology [4]. Patwardhan et al. [4] pointed out that there are three main roles of amine-based polymers in the synthesis of silica materials: (1) catalysis, (2) aggregation, and (3) structure direction (template/scaffold) or a combination thereof. Indeed, silicatein extracted from the sponge *Tethya aurantia* was found to enhance the hydrolysis and condensation of silicic acid at neutral pH [5]. Cationic peptides, including poly-L-lysine and poly-L-arginine were found to dramatically promote the aggregation of silica due to electrostatic or chemical interactions [6]. In addition, poly-L-lysine was found to direct the formation of spherical, petal-like and sheet-like hexagonal silica [7]. Due to the fact that synthetic amine-based polymers from natural biosilica sources cannot be readily obtained restricting their industrial applications. Therefore, the invention on bioinspired silica synthesis should not be limited to understanding their roles in the formation of silica products, but should also extend to the use of biomaterials that are cheaper and readily available in nature.

Recently, it has been demonstrated that chitosan, which is produced from partial *N*-deacetylation of chitins, easily obtained from a commercial source, is effective for bioinspired

* Corresponding author at: National Center of Excellence for Petroleum, Petrochemicals and Advance Material, Department of Chemical Engineering, Faculty of Engineering, Kasetsart University, Bangkok 10900, Thailand. Tel.: +66 2579 2083; fax: +66 2561 4621.
E-mail address: fengttwi@ku.ac.th (T. Witoon).

0272-8842/$36.00
http://dx.doi.org/10.1016/j.ceramint.2012.04.056

silica synthesis at ambient temperature and neutral pH. However, to the best of our knowledge, the effect of chitosan on the formation of silica nanoparticles has not yet been understood. Moreover, different roles of chitosan molecules on the formation of silica nanoparticles have been reported. For example, Chang et al. [8] found that chitosan could catalyze the aggregation of colloidal silica nanoparticles in weakly acidic solution (pH values of 4–5.6) without a significant increase in the rate of silica polycondensation. Demadis et al. [9] revealed that phosphonated chitosan was able to inhibit silicic acid condensation at neutral pH *via* a combination of electrostatic and hydrogen-bonding interactions. Our previous work reported the effect of chitosan on the formation of silica particles using sodium silicate derived from rice husk ash as a silica source [10–12]. We found that chitosan played an important role as a scaffold for the biosilica deposition, leading to the formation of the bimodal porous silicas after chitosan removal. The different roles of chitosan molecules might result from the different investigated conditions such as pH value, temperature, concentration and type of precursors.

In this study, we report the effects of pH and chitosan concentration on silica synthesis using tetraethyl orthosilicate (TEOS) as a silica source (instead of sodium silicate). N_2-sorption was used to determine the pore size and the size of the silica nanoparticles, while scanning electron microscopy (SEM) and transmission electron microscopy (TEM) were used to investigate the morphology and size of silica nanoparticles. Based on the results of our analyses we found that chitosan molecules could control the size of silica nanoparticles; to better understand the process, a model for this bioinspired silica synthesis was proposed. These results provide essential information for further development of a simple, low-cost, environmentally friendly route to synthesize silica with novel structures and tailored properties.

2. Experimental

2.1. Chemicals and reagents

Chitosan with 80% deacetylation was purchased from Eland Corporation. The molecular weight of the chitosan, determined by Gel Permeation Chromatography (GPC, Waters 600E) using 0.5 M acetic acid and 0.5 M sodium acetate as the eluent was found to be approximately 290 kDa. Tetraethyl orthosilicate (TEOS), acetic acid and ammonium hydroxide were purchased from Sigma–Aldrich. All chemicals and reagents are of analytical grade and used without any further purification.

2.2. Preparation of silica nanoparticles

In a typical synthesis process, chitosan was dissolved overnight in 60 mL of 2% (v/v) acetic acid in deionized water at room temperature, agitated with a magnetic stirrer overnight. Subsequently, TEOS was added into the chitosan solution. It should be noted that, measured with a pH meter (model CG-842, Schott), the pH value after mixing was approximately 4. Then the pH value of the mixture was quickly adjusted to 5, 6, 6.5, 7, 8.5, and 9 by the addition of 5 M NH_4OH. The resulting mixtures, containing SiO_2 (0.015625 M) and chitosan (0, 0.000345, and 0.001379 mM), were stirred at 40 °C for 6 h. Subsequently, the obtained mixtures were transferred into a glass bottle and aged in an oven at 60 °C for 24 h. The resulting products were obtained by washing with deionized water, followed by three centrifugation/redispersion cycles at 10,000 rpm for 10 min. The silica–chitosan composites were dried at 120 °C for 24 h and calcined in air at 600 °C for 4 h at a heating rate of 2 °C/min. The obtained products are designated as S-*X*-*Y* where *X* is the pH value and *Y* is the chitosan concentration.

2.3. Characterization of porous silica products

Nitrogen sorption isotherms of silica products were measured at −196 °C with a Quantachrome Autosorb-1C instrument. Prior to sorption measurements, the products were degassed at 200 °C for 12 h. The pore size distribution was calculated by using the Barrett–Joyner–Halenda (BJH) methods. The specific pore volumes were measured at a relative pressure P/P_0 of 0.995. The total surface area (S_{BET}) of the silica products was derived by using the BET (Brunauer–Emmert–Teller) analysis in the relative pressure range between $P/P_0 = 0.05$ and 0.3. In order to determine the envelope surface area of only the backbone particles, the so-called specific external surface area S_{ext} was estimated as the difference between S_{BET} and S_{micro}, where S_{micro} was the micropore surface area determined by a modified *t*-plot method (MP-method). The mean particle size *d* was related to the specific external surface area and the particle density by Alexander and Iler [13]

$$d = \frac{6}{S_{ext} \cdot \rho_{silica\ particle}} \quad (1)$$

where the density of a silica nanoparticles was assumed to be 2200 kg/m^3 [13].

The surface morphology of the silica products was analyzed with a field emission scanning electron microscopy (FE-SEM: JEOL JSM-6301F with Au-coating, operated at 20 keV). The nanostructures of the products were revealed with the application of transmission electron microscopy (TEM: JEOL JEM-2010 microscope with an acceleration voltage of 200 kV). In order to prepare a sample for TEM analysis, the porous silica products were suspended in ethanol and dried at room temperature on a copper grid coated with a carbon film.

3. Results and discussion

Fig. 1 shows the N_2-sorption isotherm of the calcined silica products prepared at different pH values and chitosan concentrations. Without the use of chitosan, the isotherm of silica products synthesized at pH 5 shows a typical type IV shape with H2 hysteresis loop (Fig. 1a), indicating an ink-bottle pore structure. When the pH of the mixture was increased from 5 to 6.5, the isotherms shifted toward higher relative pressure

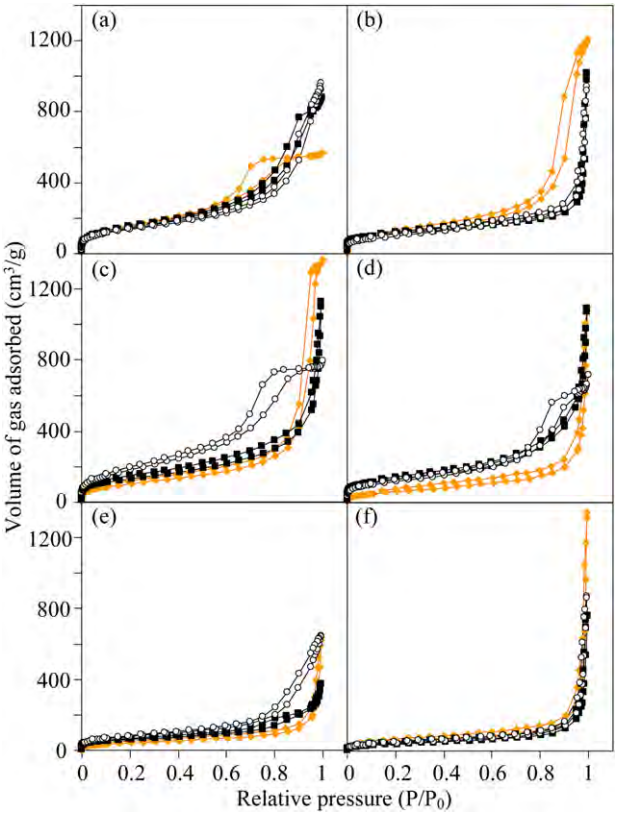

Fig. 1. N_2 sorption isotherms of silica products prepared at different pH values and chitosan concentrations: (a) pH 5, (b) pH 6, (c) pH 6.5, (d) pH 7, (e) pH 8.5 and (f) pH 9. The symbols orange diamond, black rectangular and white cycle represent the products without chitosan, with 0.000345 mM chitosan, and with 0.001379 mM chitosan, respectively. (For interpretation of the references to color in this figure legend, the reader is referred to the web version of the article.)

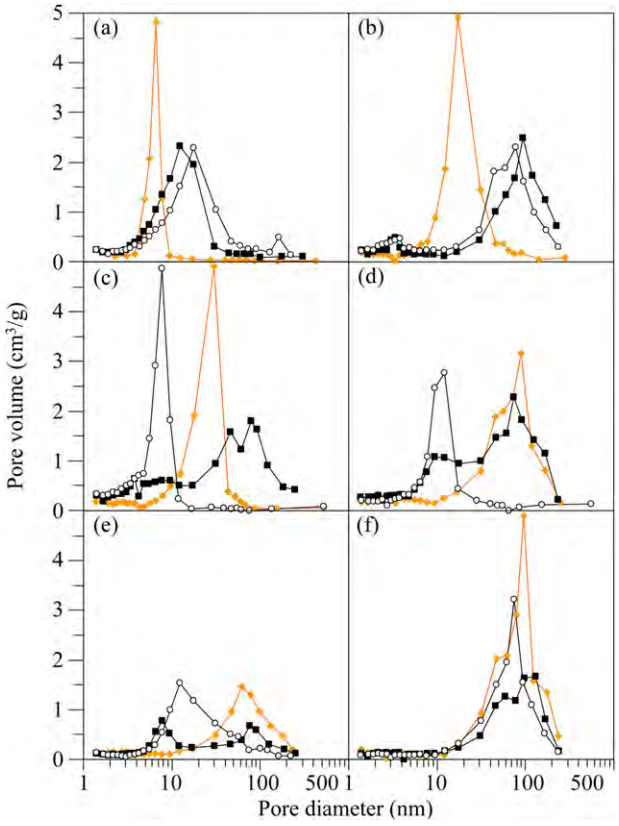

Fig. 2. Pore size distribution of silica products prepared at different pH values and chitosan concentrations: (a) pH 5, (b) pH 6, (c) pH 6.5, (d) pH 7, (e) pH 8.5, and (f) pH 9. The symbols orange diamond, black rectangular and white cycle represent the products without chitosan, with 0.000345 mM chitosan, and with 0.001379 mM chitosan, respectively. (For interpretation of the references to color in this figure legend, the reader is referred to the web version of the article.)

and the type of hysteresis loop was changed to H1, indicating the existence of pores in the form of interstices between closed-packed and equal-sized spherical particles. With yet higher pH values, the type IV isotherm was no longer obtained and instead a type II isotherm was observed, an indication of the presence of macropores. Once chitosan was applied, the isotherm types and hysteresis loops were significantly changed depending on both the pH of mixture and the chitosan concentration. The isotherms were however not clear enough to reveal the effect of the pH of mixture and chitosan concentration on the size of silica particle. As a result, the pore size distribution, SEM, and TEM images of silica products are employed instead.

The pore size distributions of the silica products synthesized at various conditions are shown in Fig. 2. It was found that the effect of chitosan addition at different pH values of the mixture can be classified into three categories: (1) increased pore size ($5 \leq pH \leq 6$), (2) decreased pore size ($6.5 \leq pH \leq 8.5$), and (3) no effect on the pore size (pH 9). For the first category, the pore size is affected by the different levels of chitosan concentration. For the second category, the silica products prepared at low chitosan concentration exhibited a bimodal pore size distribution, whereas only smaller pore sizes existed in the silica products prepared at a higher chitosan concentration. The physical properties of all silica products are given in Table 1. The average particle size of the silica products (Fig. 3) was evidently found to correspond to their pore sizes. However, the average particle size of the silica products prepared at pH 6.5 and low chitosan concentration was larger than that prepared at same pH but without the chitosan addition. This can be explained by the fact that two different silica particle sizes of silica products were obtained with mainly large silica nanoparticles.

The surface morphologies of the silica products were investigated by SEM and representative images are shown in Fig. 4. At pH 5, the silica product prepared without chitosan

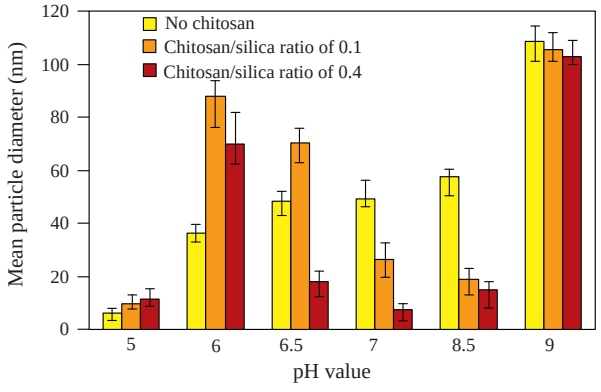

Fig. 3. Average size of silica particles determined by N_2-sorption.

Table 1
Physical properties of the products synthesized under various conditions.

Sample ID[a]	BET surface area (m^2/g)	Micropore surface area (m^2/g)	External surface area (m^2/g)	Average silica particle size (nm)	Total pore volume (cm^3/g)
S-5-0	574	117	457	6.0	0.88
S-5-0.000345	535	247	288	9.5	1.37
S-5-0.001379	483	247	236	11.5	1.49
S-6-0	426	345	81	33.6	1.67
S-6-0.000345	370	339	31	88.0	1.87
S-6-0.001379	351	312	39	70.1	1.66
S-6.5-0	410	353	57	48.3	2.26
S-6.5-0.000345	497	458	39	70.3	1.66
S-6.5-0.001379	730	578	152	18.0	1.56
S-7-0	230	175	55	49.2	1.70
S-7-0.000345	445	342	103	26.5	2.04
S-7-0.001379	420	56	364	7.5	1.32
S-8.5-0	150	102	48	57.4	0.98
S-8.5-0.000345	277	133	144	18.9	0.78
S-8.5-0.001379	207	26	181	15.0	1.00
S-9-0	195	170	25	108.7	2.08
S-9-0.000345	146	120	26	105.3	1.55
S-9-0.001379	160	133	27	103.0	1.68

[a] The silica products are designated as S-*X*-*Y* where *X* is the pH value and *Y* is the chitosan concentration.

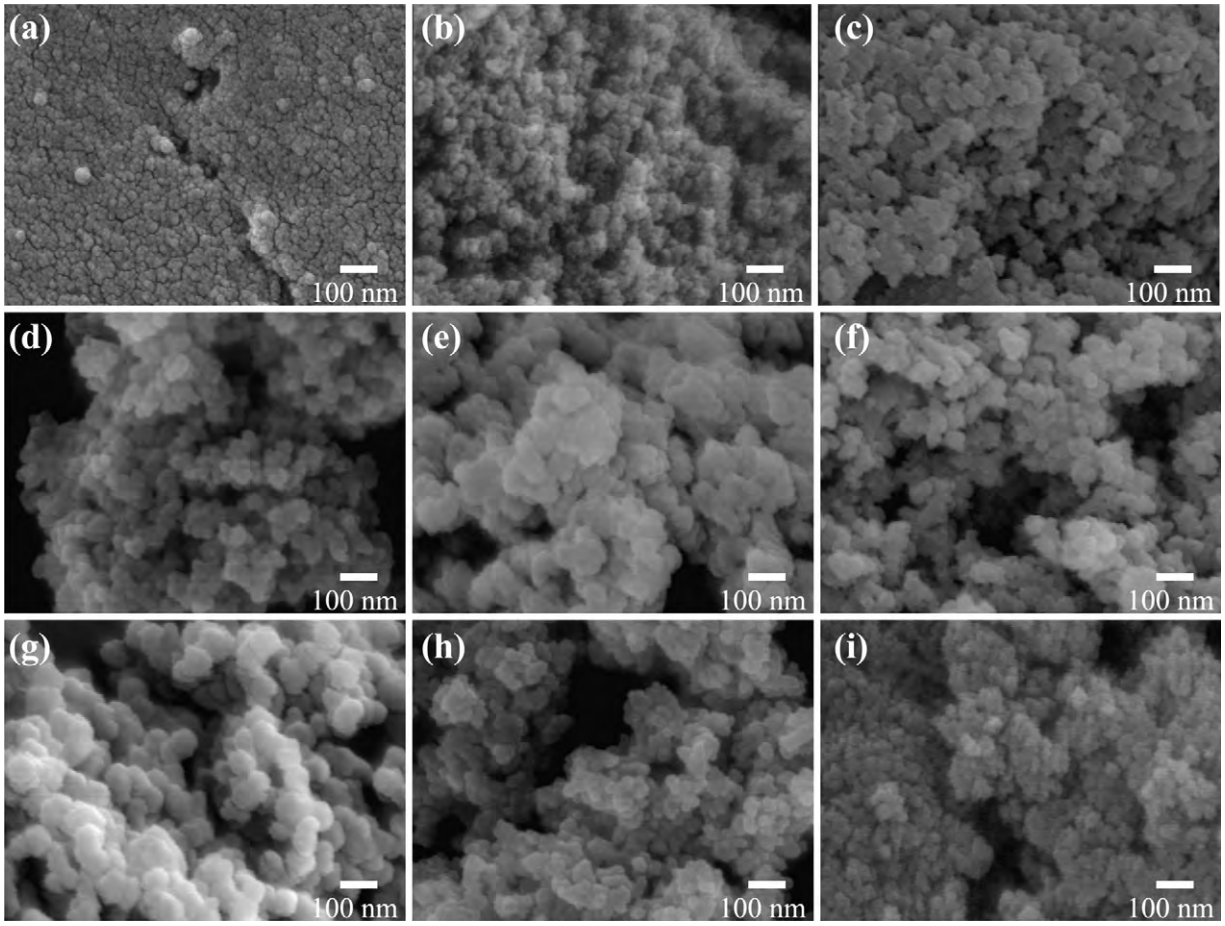

Fig. 4. SEM images of silica products prepared at different pH values and chitosan concentrations: (a) pH 5 and w/o chitosan, (b) pH 5 and 0.000345 mM chitosan, (c) pH 5 and 0.001379 mM chitosan, (d) pH 6.5 and w/o chitosan, (e) pH 6.5 and 0.000345 mM chitosan, (f) pH 6.5 and 0.001379 mM chitosan, (g) pH 7 and w/o chitosan, (h) pH 7 and 0.000345 mM chitosan, and (i) pH 7 and 0.001379 mM chitosan.

(Fig. 4a) showed a dense and continuous gel with an aggregate size of approximately 20 nm. With increasing chitosan concentration (Fig. 4b and c), the surface morphology changed to a loose aggregate of silica nanoparticles (30–50 nm). At pH 6.5 (Fig. 4d–f) the silica product prepared without chitosan (Fig. 4d) showed a loose aggregate of silica nanoparticles with an average size of approximately 50 nm. Moreover, the size of silica nanoparticle first increases and then decreases when the chitosan concentration is increased from 0.000345 to 0.001379 mM. The surface morphology of silica products prepared at pH 7 (Fig. 4g–i) showed the opposite trend of the morphology of silica products prepared at pH 6.

TEM was performed to reveal the size of silica nanoparticles; representative images of silica products prepared at pH 5 and 7 are shown in Figs. 5 and 6, respectively. At pH 5 and no chitosan addition (Fig. 5a and b), the size of silica nanoparticles was approximately 5–7 nm. The size of silica nanoparticles was increased from 10–12 nm (Fig. 5c and d) to 14–18 nm (Fig. 5e and f) with increasing chitosan concentration. At pH 7, the size of silica nanoparticles prepared without the chitosan was approximately 20–36 nm (Fig. 6a and b). At low chitosan concentration (Fig. 6c and d), the silica product consisted of two different domains, the aggregate of large and small sizes of silica nanoparticles. At high chitosan concentration (Fig. 6e and

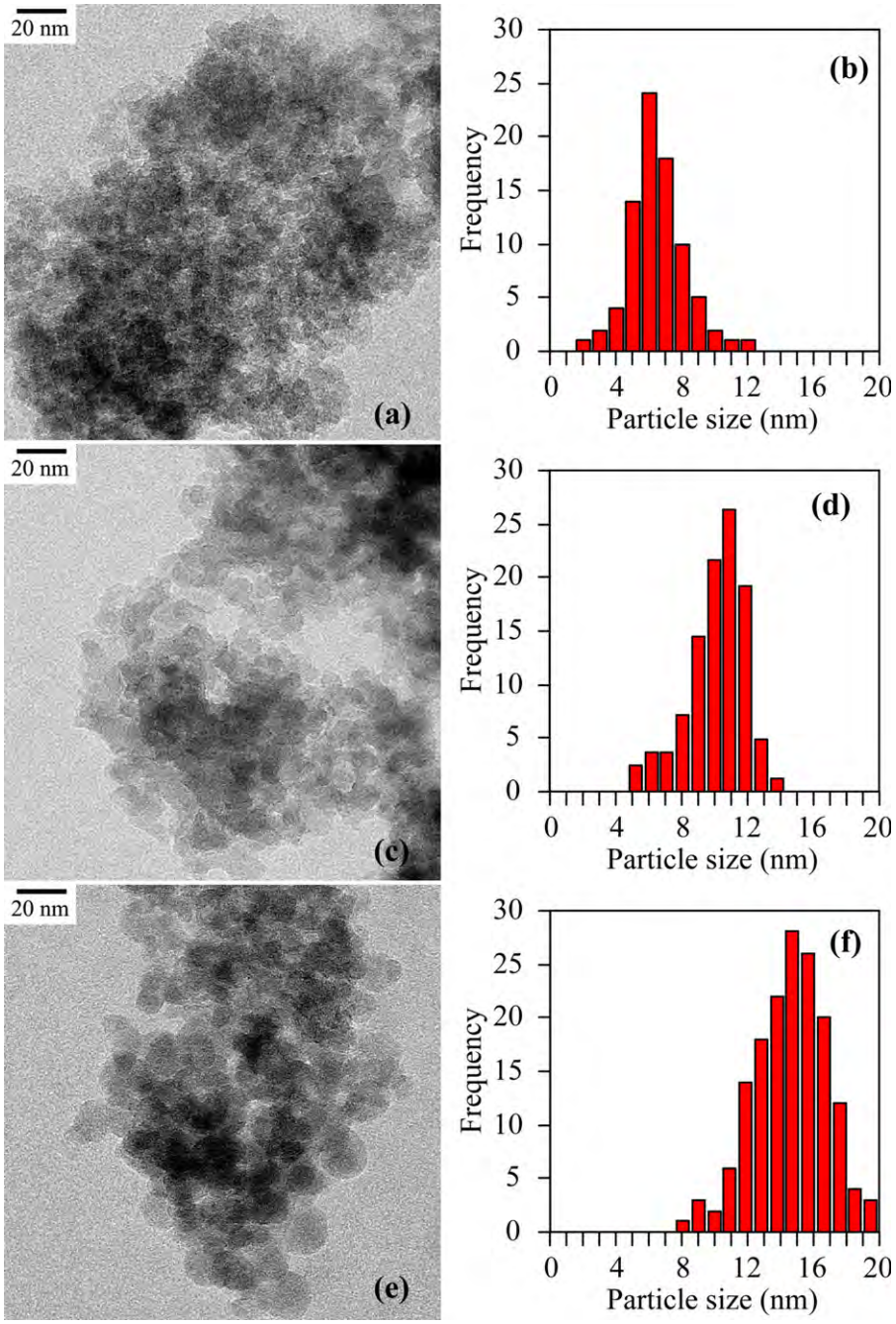

Fig. 5. TEM images and histogram analysis of silica products prepared at pH 5 and different chitosan concentrations: (a) and (b) w/o chitosan, (c) and (d) 0.000345 mM chitosan, (e) and (f) 0.001379 mM chitosan.

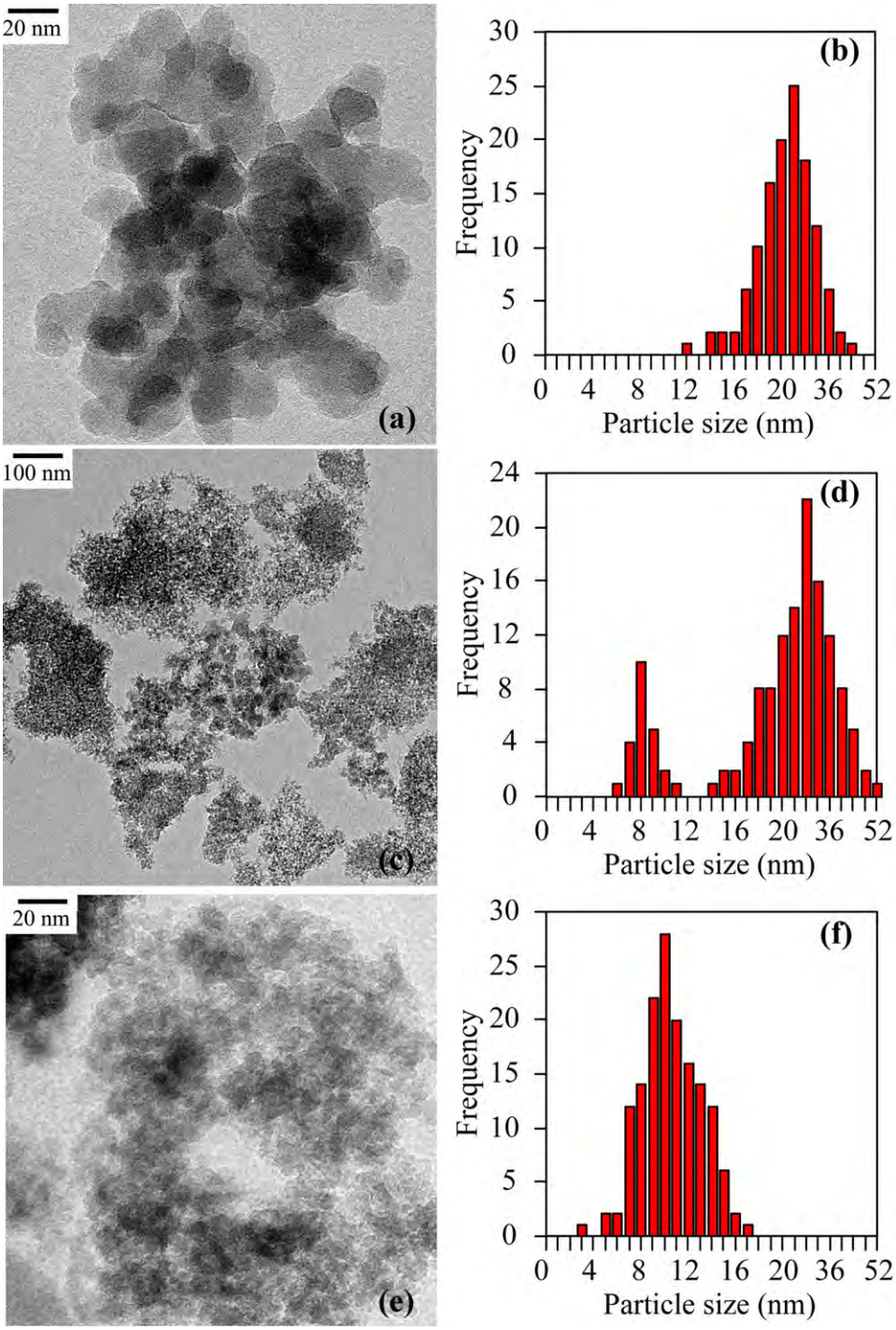

Fig. 6. TEM images and histogram analysis of silica products prepared at pH 7 and different chitosan concentrations: (a) and (b) w/o chitosan, (c) and (d) 0.000345 mM chitosan, (e) and (f) 0.001379 mM chitosan.

f), the aggregation of large-sized silica particles was no longer observed and instead the aggregation of small-sized silica particles was found. The results from TEM analysis are in good agreement with the results of N_2-sorption.

The formation mechanisms of silica products prepared at different pH values and chitosan concentrations are proposed as shown in Fig. 7. Based on the results mentioned above, it was found that chitosan plays two different roles in the growth of silica particles depending on the range of pH values: (1) at pH 5–6, chitosan promotes the increase of silica particle size and (2) at pH 6.5–8.5, chitosan decreases the size of silica particle. Many works have reported that the amino groups along the backbone chains of polymers can act as an acid–base catalyst that facilitates the rate of silica condensation [5,14]. The increase of silica condensation rate results in a highly branched structure; this in turn prevents the shrinkage of silica at an earlier state of drying due to the stiffness of the impinging clusters, resulting in larger pores

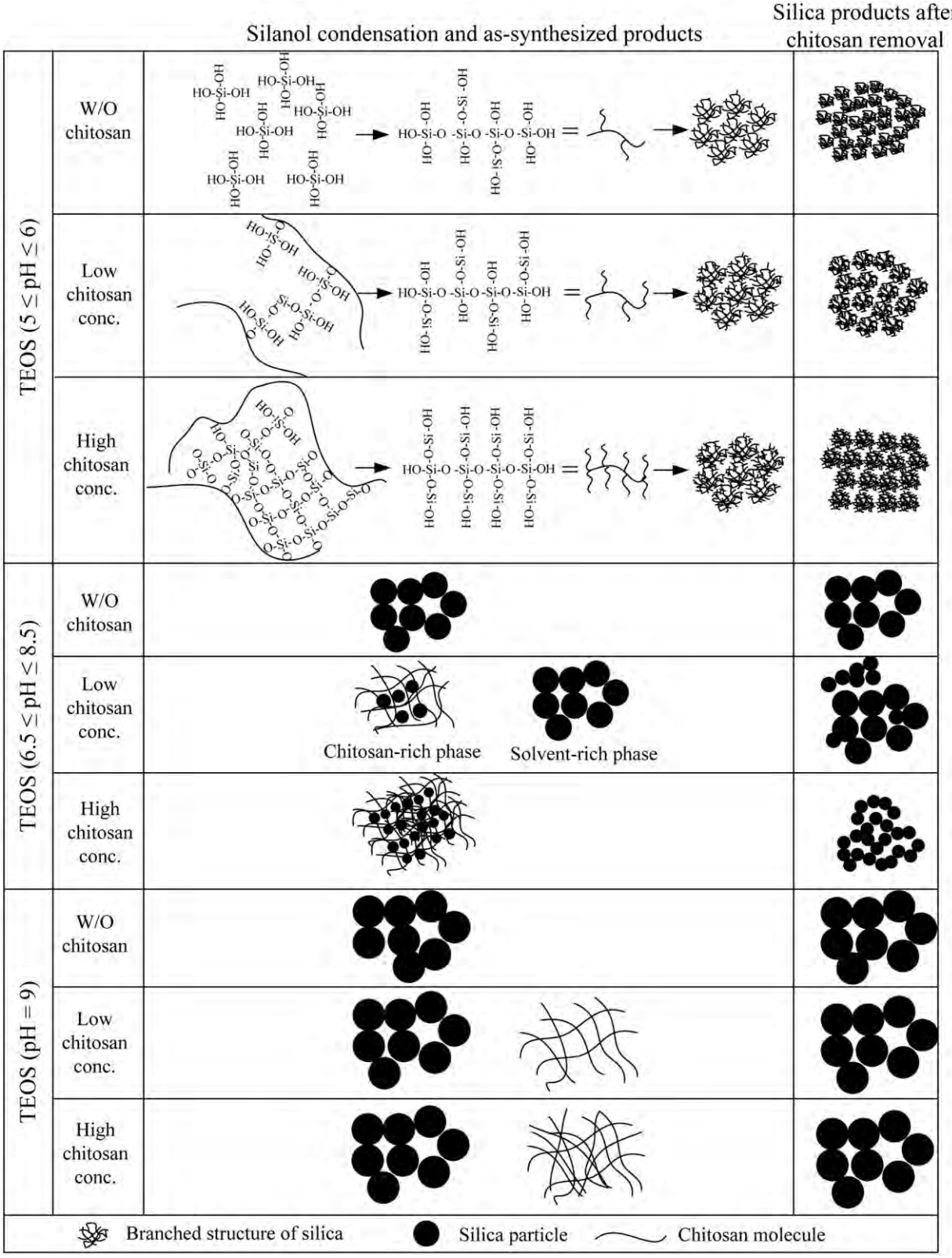

Fig. 7. Schematic presentation of the roles of chitosan on the silica formation at different pH values and chitosan concentrations.

[15]. This provides a reasonable explanation for the effect of chitosan molecules on the growth of the silica nanoparticles at pH $\leq$ 6. However, it fails to explain why the size of the silica nanoparticle tends to decrease when the pH of the mixture is varied in the range of 6.5 and 8.5. Moreover, the results of pore size distribution (Fig. 2) and TEM image (Fig. 6c and d) indicated that there are two different sizes of silica nanoparticle occurring at a low chitosan concentration.

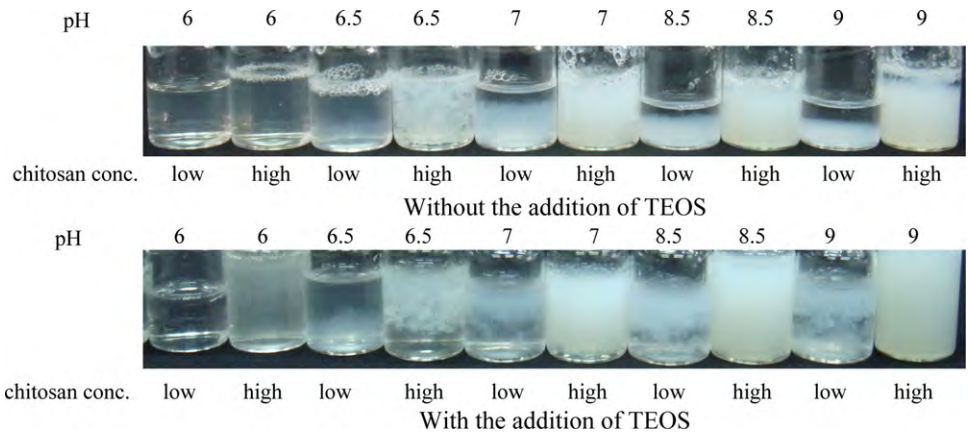

Fig. 8. Visual observations of the chitosan solution and TEOS–chitosan solution at different pH values and chitosan concentrations.

This was possibly attributed to the dissimilarity of the growth of silica nanoparticles.

Visual inspection of the chitosan precipitates at different pH values and chitosan concentrations gives valuable information and is useful to explain the effects of chitosan on the formation of silica nanoparticles at $6.5 \leq \text{pH} \leq 8.5$ (Fig. 8). It can be seen that the initial chitosan in a 1% (v/v) acetic acid solution had a very clear appearance (pH value of approximately 4). The pH value of the chitosan solution was adjusted by using 5 M NH_4OH. At pH 5 and 6, the solution remained clear at all chitosan concentrations. Once the pH value was adjusted to 6.5, the chitosan immediately precipitated and the amount of precipitate increased with increasing chitosan concentrations. A similar trend was also found in the pH range of 6.5–9. This observation could be explained by the fact that the chitosan has a pK_a value of ~6.5, and therefore it could be dissolved in the acidic solution due to the protonation of amino groups. The increase in pH value caused a decrease in the number of these positively charged amino groups, resulting in the aggregation and precipitation of chitosan molecules (phase separation).

Adding TEOS into the chitosan solution and adjusting the pH of the mixture gave a similar result to the original chitosan solution (Fig. 8). When TEOS was hydrolyzed to silicic acid in a low chitosan concentration system, it could distribute into a solvent-rich phase and a chitosan-rich phase. The silica growth in the solvent-rich phase was therefore similar to the silica synthesized without the addition of chitosan (see Fig. 2c–e). Based on the results of the pore size distribution of silica products synthesized without the chitosan, the size of silica nanoparticles in the solvent-rich phase was larger than that in the chitosan-rich phase. One possible explanation is that chitosan molecules can react with silicic acid through residual protonation of amino groups or through hydrogen-bonding with hydroxyl groups [8,16], which not only reduce the quantity of available silicic acid but also prevent further silica condensation reactions. Additionally, the size of silica nanoparticles might be limited by the size of the chitosan network, resulting in the occurrence of smaller silica nanoparticles. As results, the silica products synthesized at low chitosan concentration have two different sizes. At a higher chitosan concentration, almost all of the silicic acid reacted with chitosan molecules, and therefore, only small silica nanoparticles could be formed.

4. Conclusion

In summary, the interaction of biopolymer chitosan with tetraethyl orthosilicate on the formation of silica nanoparticles was explored at various pH values of the mixture and at various chitosan concentrations. For $5 \leq \text{pH} \leq 6$ and low chitosan concentration, the size of silica nanoparticles significantly increased due to the enhancement of the rate of silica condensation. The size of the silica nanoparticles had significant dependence on chitosan concentration. For $6.5 \leq \text{pH} \leq 8.5$ and low chitosan concentration, a bimodal pore size distribution was obtained since silica grew in two distinct phases. When chitosan concentration was increased yet further, only small silica particle sizes were observed. However, at pH 9, chitosan did not show any significant effect on the formation of silica products. The results presented here contribute to understanding of how chitosan molecules control silica synthesis, as well as the novel development methods of materials with tailored properties.

Acknowledgements

This work is financially supported by the Research Grant for New Scholar (Grant No. MRG5480196) co-funded by the Thailand Research Fund (TRF); the Commission on Higher Education, Thailand; and Kasetsart University, Thailand. Support from the ‘‘National Research University Project of Thailand (NRU)’’ is also acknowledged.

References

[1] T. Witoon, M. Chareonpanich, J. Limtrakul, Effect of hierarchical meso–macroporous silica supports on Fischer–Tropsch synthesis using cobalt catalyst, Fuel Processing Technology 92 (2011) 1498–1505.
[2] F. Chen, Y. Zhu, Chitosan enclosed mesoporous silica nanoparticles as drug nano-carriers: sensitive response to the narrow pH range, Microporous and Mesoporous Materials 150 (2012) 83–89.
[3] T. Witoon, N. Tatan, P. Rattanavichian, M. Chareonpanich, Preparation of silica xerogel with high silanol content from sodium silicate and

its application as CO_2 adsorbent, Ceramics International 37 (2011) 2297–2303.
[4] S.V. Patwardhan, S.J. Clarson, C.C. Perry, On the role(s) of additives in bioinspired silicification, Chemical Communications (2005) 1113–1121.
[5] Y. Zhou, K. Shimizu, J.N. Cha, G.D. Stucky, D.E. Morse, Efficient catalysis of polysiloxane synthesis by silicatein α requires specific hydroxyl and imidazole functionalities, Angewandte Chemie-International Edition 38 (1999) 779–782.
[6] T. Coradin, O. Durupthy, J. Livage, Interactions of amino-containing peptides with sodium silicate and colloidal silica: a biomimetic approach of silicification, Langmuir 18 (2002) 2331–2336.
[7] S.V. Patwardhan, N. Mukherjee, M. Steinitz-Kannan, S.J. Clarson, Bioinspired synthesis of new silica structures, Chemical Communications (2003) 1122–1123.
[8] J.S. Chang, Z.W. Kong, D.F. Hwang, K.L.B. Chang, Chitosan-catalyzed aggregation during the biomimetic synthesis of silica nanoparticles, Chemistry of Materials 18 (2006) 702–707.
[9] K.D. Demadis, A. Ketsetzi, K. Pachis, V.M. Ramos, Inhibitory effects of multicomponent, phosphonate-grafted zwitterionic chitosan biomacromolecules on silicic acid condensation, Biomacromolecules 9 (2008) 3288–3293.
[10] T. Witoon, M. Chareonpanich, J. Limtrakul, Effect of acidity on the formation of silica–chitosan hybrid materials and thermal conductive property, Journal of Sol–Gel Science and Technology 51 (2009) 146–152.
[11] T. Witoon, M. Chareonpanich, J. Limtrakul, Size control of nanostructured silica using chitosan template and fractal geometry: effect of chitosan/silica ratio and aging temperature, Journal of Sol–Gel Science and Technology 56 (2010) 270–277.
[12] T. Witoon, S. Tepsarn, P. Kittipokin, B. Embley, M. Chareonpanich, Effect of pH and chitosan concentration on precipitation and morphology of hierarchical porous silica, Journal of Non-Crystalline Solids 357 (2011) 3513–3519.
[13] G.B. Alexander, R.K. Iler, Determination of particle sizes in colloidal silica, Journal of Physical Chemistry 57 (1953) 932–934.
[14] R.K. Iler, Chemistry of Silica, John Wiley & Sons, New York, 1979.
[15] C.J. Brinker, G.W. Scherer, Sol–Gel Science: The Physics and Chemistry of Sol–Gel Processing, Academic Press, London, 1990.
[16] K.D. Demadis, K. Pachis, A. Ketsetzi, A. Stathoulopoulou, Bioinspired control of colloidal silica *in vitro* by dual polymeric assemblies of zwitterionic phosphomethylated chitosan and polycations or polyanions, Advances in Colloid and Interface Science 151 (2009) 33–48.

Available online at www.sciencedirect.com
ScienceDirect
Ceramics International 37 (2011) 3291–3298
CERAMICS INTERNATIONAL
www.elsevier.com/locate/ceramint

Characterization of calcium oxide derived from waste eggshell and its application as CO_2 sorbent

Thongthai Witoon [a,b,*]

[a] National Center of Excellence for Petroleum, Petrochemicals and Advance Material, Department of Chemical Engineering, Faculty of Engineering, Kasetsart University, Bangkok 10900, Thailand
[b] Center for Advanced Studies in Nanotechnology and Its Applications in Chemical Food and Agricultural Industries, Kasetsart University, Bangkok 10900, Thailand

Received 10 May 2011; accepted 24 May 2011
Available online 30 May 2011

Abstract

The carbonation–calcination looping cycle of calcium-based sorbents is considered as an attractive method for CO_2 capture from combustion gases because it can reduce the cost during the capture steps compared to conventional technologies, e.g., solvent scrubbing. In this study, waste eggshell was used as raw material for calcium oxide-based sorbent production. The commercially available calcium carbonate was employed for comparison purpose. Calcination behavior, crystal type and crystallinity, surface chemistry, qualitative and quantitative elemental information, specific surface area and pore size, morphology of the waste eggshell and the calcined waste eggshell were characterized by thermal gravimetric analysis (TGA), X-ray diffraction (XRD), Fourier transform infrared spectroscopy (FT-IR), X-ray fluorescence (XRF), N_2 sorption analysis and scanning electron microscopy (SEM), respectively. The carbonation–calcination cycles were carried out using a TGA unit with high purity CO_2 (99.999%). It was found that the carbonation conversion of the calcined eggshell was higher than that of the calcined commercially available calcium carbonate after several cycles at the same reaction conditions. This could be due to the fact that the calcined eggshell exhibited smaller particle size and appeared more macropore volume than the calcined commercially available calcium carbonate. As results, the calcined eggshell provided a higher exposed surface for the surface reaction of CO_2.

Keywords: A. Sintering; C. Chemical properties; Eggshell; Calcium oxide; CO_2 sorbent; CO_2 capture

1. Introduction

The problem of global warming caused by CO_2 emission has raised serious concerns since the CO_2 concentration in the atmosphere has increased rapidly due to the industrial revolution. The reduction of CO_2 emission can occur as a result of increased energy efficiency [1,2], substitution of non-carbon fuels [3] or by the capture and storage of CO_2 [4,5]. With the United Nations predicting world population growth from 6.6 billion in 2007 to 8.2 billion by 2030, demand for energy must increase substantially over that period [6] which no doubt erase gains associated with increased energy efficiency. Fossil fuels will continue to be major source of energy for the next few decades because the non-carbon energy sources still are more limited and more expensive. Thus, the capture and storage of CO_2 will be required in order to allow us to utilize fossil fuels without CO_2 emission.

The current commercial operation for CO_2 capture used a chemical absorption method with Monoethanol Amine (MEA) as the sorbent has been recognized as the most matured process [7]. The chemical interaction between the MEA and the CO_2 molecules is strong and this offers a fast and effective removal of the CO_2 in one stage of absorption. However, the strong interaction between the MEA and the CO_2 molecules requires important amounts of energy to regenerate the MEA solution. The MEA is highly corrosive leading to the use of costly absorber packing and column materials. Finally, the impurities and minor components in the flue gas including SO_2, NO_2, O_2, etc. have to be removed before the gas enters the absorber in order to prevent the degradation of the MEA solution. This

* Correspondence address: National Center of Excellence for Petroleum, Petrochemicals and Advance Material, Department of Chemical Engineering, Faculty of Engineering, Kasetsart University, Bangkok 10900, Thailand. Tel.: +66 2579 2083; fax: +66 2561 4621.
E-mail address: fengttwi@ku.ac.th.

0272-8842/$36.00
doi:10.1016/j.ceramint.2011.05.125

requires several pretreatment processes and therefore leads to high capture costs estimated at around 59.1$/tonnes of CO_2 avoided [7]. Many researchers have focused on the development of new absorbents to increase in the CO_2 absorption rate. Rivera-Tinoco and Bouallou [8] demonstrated that the CO_2 absorption by ammonia was faster than that carried out by N-methyldiethanolamine (MDEA). Various strategies for minimizing the energy requirements from the chemical absorption method have been investigated and proposed. Harkin et al. [9] combined pinch analysis and linear programming optimization for the energy requirements of power plants. They found that the effective heat integration can reduce the energy requirements by up to 50%. Nevertheless, the CO_2 capture by means of amines may be not suitable since some of the amines escaping the recycling process will be emitted into the air and will also form other compounds such as nitrosamines and nitramines which can affect health and environment [10]. It is therefore essential to develop technologies that can reduce the cost of carbon capture with environment friendly.

The use of calcium oxide (CaO) for CO_2 looping cycle has attracted increasing attention due to a number of its potential advantages, including a wide range of potential operating temperatures, reduction of energy requirement, elimination of the generation of liquid wastes, and the relatively inert nature of solids wastes [11]. The application of CaO is basically through carbonation–calcination cycles with CO_2 based on the reversible reaction (Eq. (1)).

$$Cao_{(s)} + CO_{2(g)} \leftrightarrow CaCO_{3(s)}, \quad \Delta H^{\circ}{}_{600\,^{\circ}C} = -171.2\,\text{kJ mol}^{-1} \tag{1}$$

The major challenge of this cycle in practical applications is a sharp decay after few cycles of carbonation–calcination. The deactivation of CaO-based CO_2 sorbents is caused by the sintering process due to three majors factors: (1) the carbonation is highly exothermic; (2) there is a volumetric expansion from CaO to $CaCO_3$ (from 16.9 to 34.1 cm^3/mol), which significantly decreases the distance between particles in the carbonated state; (3) $CaCO_3$ has a Tammann temperature of 533 °C, lower than normal carbonation temperature [12]. Recently, several strategies have been studied to overcome those problems, including: (1) decreasing CaO particle size [13]; (2) synthesizing new CaO-based mesoporous silica [14]; (3) improving the porosity of CaO by hydration treatment [15]; (4) enhancement of reactivity using surfactant-modified CaO [16]; (5) addition of inert phase such as potassium, sodium, compounds of titanium, $KMnO_4$-doped CaO, MgO-doped CaO, La_2O_3-doped CaO [17–20]; (6) using other calcium-based natural minerals, such as dolomite and huntite [21]. Besides, there are several natural calcium sources from wastes, such as mussel shell, scallop shell, mollusk shell, and eggshell.

Eggs represent a major ingredient in a large variety of products such as cakes, salad dressings and fast foods, whose production results in several daily tons of waste eggshell and incur considerable disposal costs in Thailand. The disposal of the waste is a very important problem, which can cause risk to public health, contamination of water resources and polluting the environment. Based on the cleaner production concepts [22], the use of wastes to be the CO_2 sorbent not only provides the technology with competitive sorbent processing costs but also eliminate the wastes simultaneously. To the best of my knowledge, very few researches on the use of waste eggshell as the CO_2 sorbent have been reported [23]. In this work, CaO derived from waste eggshell were thoroughly investigated by using thermogravimetric analysis (TGA), X-ray diffraction, X-ray fluorescence, Fourier transform infrared (FTIR) spectroscopy, nitrogen sorption measurement, scanning electron microscopy (SEM). CO_2 adsorption capacity of the CaO derived from waste eggshell was measured by gravimetric method at different temperatures. Durability test of the CaO derived from waste eggshell was conducted. The similar experiments were repeated with the commercially available $CaCO_3$ for comparison purpose.

2. Materials and methods

2.1. Materials

Waste eggshell sample was collected from canteen, Kasetsart University, Bangkok, Thailand. The sample was washed several times with deionized water to remove additional residues from its surface, filtered with 0.45 μm membrane filter and then dried at 105 °C for 24 h. The commercially available calcium carbonate ($CaCO_3$) was purchased from Ajax Finechem for comparison. The samples were pulverized and sieved in the range of 250–425 μm. The obtained samples were calcined at 900 °C for 1 h under N_2 atmosphere.

2.2. Characterization

The weight change and the calcination temperature of dried eggshell were investigated by using DSC-TGA 2960 thermal analyzer in a flow of nitrogen atmosphere at a heating rate of 10 °C/min. The sample loading was typically 20–25 mg.

X-ray fluorescence (PANalytical Epsilon 5) was used for the qualitative and quantitative analysis of the inorganic compounds in the natural and the calcined eggshell.

X-ray diffraction (XRD) patterns of the dried eggshell, the calcined eggshell and the calcined $CaCO_3$ were done on a diffractometer (Bruker D8 Advance) using Cu-K_α radiation. The measurements were made at room temperature at a range of 15–70 °C on 2θ with a step size of 0.05°. The diffraction patterns were analyzed using the Joint Committee on Powder Diffraction Standards (JCPDS). CaO crystallite size was calculated using Scherrer equation from the most intense CaO peak at 2θ of 37.4° as shown below:

$$d = \frac{0.89\lambda}{B\cos\theta} \times \frac{180^{\circ}}{\pi} \tag{2}$$

where d is the mean crystallite diameter, λ is the X-ray wave length (1.54 Å), and B is the full width half maximum (FWHM) of the CaO diffraction peak.

Fourier transform infrared (FTIR) spectra were obtained by using spectrophotometer (Bruker Tensor 27) in the range of

400–4000 cm^{-1} with a resolution of 4 cm^{-1}. The sample preparation consisted of mixing fine powder of each sample dried eggshell, calcined eggshell and calcined $CaCO_3$ with KBr powder.

N_2 adsorption–desorption isotherms of the samples were measured at −196 °C using a Quantachrome Autosorb-1C instrument. Prior to measurements, the samples were degassed at 105 °C for 24 h. Pore size distributions of the samples were determined from the adsorption branch of the isotherms by the Barrett–Joyner–Hallenda (BJH) method. The specific BET (S_{BET}) was estimated for P/P_0 values between 0.05 and 0.30. The pore volume was reported as mesopore (2–50 nm) and macropore (>50 nm) volumes.

The morphologies and dimensions of the samples were observed by scanning electron microscope (SEM; Philips XL30). SEM was operated at 14.0 kV of an accelerating voltage. The samples were sputter-coated with gold prior to analysis.

2.3. CO_2 carbonation–calcination performance tests

CO_2 carbonation–calcination measurements were performed for all CaO products by using a SDT2960 simultaneous DTA–TGA Universal 2000. A 20–25 mg sample was loaded into an alumina sample pan. Prior to any CO_2 carbonation–calcination experiment and to remove pre-adsorbed CO_2 and H_2O, the sample was first activated by heating it from room temperature in a flow of pure N_2 (100 mL/min) at a rate of 20 °C/min until 900 °C was achieved and the sample was kept at 900 °C for 5 min; then the sample was cooled to a given temperature (650, 700 and 750 °C). Once the carbonation temperature was reached and stabilized, pure CO_2 (99.999%) with a flow rate of 80 mL/min was introduced into the system while the change in the sample weight was recorded. After the carbonation for 50 min, the CO_2 flow was disconnected and the N_2 flow was subsequently introduced. The sample was heated to 900 °C at a rate of 20 °C/min and kept at 900 °C for 5 min to complete conversion to CaO. After calcination process, the sample was cooled down to a given temperature again (650, 700 and 750 °C) for carbonation process. The same experiment was repeated 11 times in order to investigate the performance of the reversibility and stability of CO_2 carbonation–calcination. The carbonation conversion is calculated as follows:

$$X_n = \frac{m^n_{carb} - m^n_{cal}}{m_0 a} \times \frac{W_{CaO}}{W_{CO_2}} \quad (3)$$

where X_n is the carbonation conversion of the sorbent after n cycles, m_0 is the initial mass of the sorbent, a is the content of CaO in the initial sorbent, m^n_{carb} is the mass of the carbonated sorbent after n cycles, m^n_{cal} is the mass of the calcined sample after n cycles. W_{CaO} and W_{CO_2} are the molar masses of CaO and CO_2, respectively. The carbonation rate is defined as follows:

$$r_n = \frac{dX_n}{dt} \quad (4)$$

where r_n is the carbonation rate after n cycles and t is the carbonation time at each cycle.

3. Results and discussion

3.1. Characterization

The suitable calcination temperature of eggshell was analyzed by TGA/DTA. As shown in Fig. 1, the TGA pattern of dried eggshell showed two distinct stages of weight losses: one at temperature below 680 °C and one between 680 and 850 °C. The first stage can be attributed to adsorbed water molecules and loss of organic compounds. The second stage exhibited the major weight loss at 830 °C, corresponding to 42 wt.% was due to the change of $CaCO_3$ phase to CaO phase which could be confirmed by the XRD and the FTIR results (Figs. 2 and 3). As the sample weight remained constant after 850 °C, the temperature of 900 °C was then suitable for the use as the calcination temperature to ensure complete conversion to CaO.

X-ray diffraction pattern of dried eggshell (Fig. 2a) shows a major peak at $2\theta = 29.5°$, indicating that calcite ($CaCO_3$) is a major phase of the waste eggshell. CaO phase with 2θ values of 32.3°, 37.4°, 53.9°, 64.2° and 67.4° was found when the eggshell was calcined at 900 °C for 1 h (Fig. 2b). The major peak of calcite phase ($2\theta = 29.5°$) was not shown in XRD pattern of the calcined eggshell, implying that the $CaCO_3$ phase was completely transformed to CaO phase. XRD pattern of the

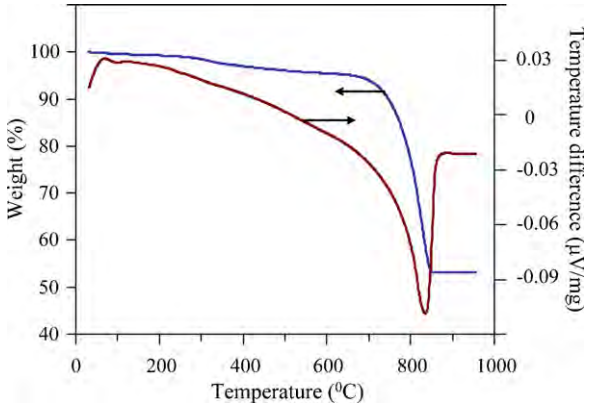

Fig. 1. TGA–DTA pattern of dried eggshell (DES).

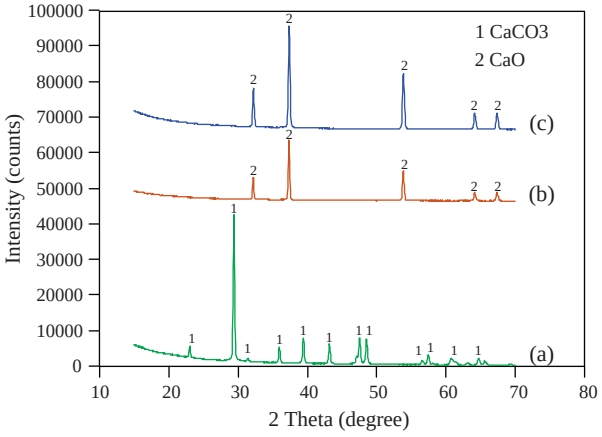

Fig. 2. XRD patterns of dried eggshell (a), calcined eggshell (b) and calcined commercially available $CaCO_3$ (c).

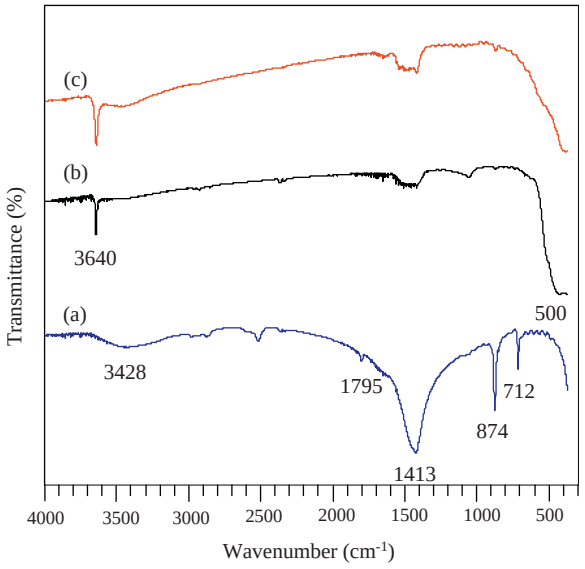

Fig. 3. FTIR spectra of dried eggshell (a), calcined eggshell (b) and calcined commercially available $CaCO_3$ (c).

calcined commercially available $CaCO_3$ (Fig. 2c) appeared at the same 2θ angles as that of the calcined eggshell. However, the peaks intensities of the calcined commercially available $CaCO_3$ were higher than those of the calcined eggshell, suggesting that the CaO crystalline size of the calcined commercially available $CaCO_3$ was larger than that of the calcined eggshell. The CaO crystallite size calculated by using Scherrer equation is listed in Table 1. It was found that the calcined eggshell generated the nanocrystalline CaO with a crystallite size of 44.3 nm, while the calcined commercially available $CaCO_3$ showed a very high degree of crystallinity with a crystallite size of more than 100 nm.

The usefulness of qualitative analysis from the characteristic frequencies provides information to identify chemical constituents in a compound. Fig. 3a shows the IR spectra of the dried eggshell. The broad transmission band at approximately 3428 cm^{-1} can be attributed to OH stretching vibration from residual waster. The weak band at 1795 cm^{-1} corresponds to C=O bonds from carbonate. Two well-defined infrared bands at 1413 and 873 cm^{-1} are characteristic of the C–O stretching and bending modes of calcium carbonate, respectively [24]. The sharp band at 712 cm^{-1} is related to Ca–O bonds [25]. Fig. 3b shows the spectrum of the calcined eggshell. The existence of peak at 3640 cm^{-1} is due to OH in $Ca(OH)_2$ formed during

Table 1
Physical properties and CaO crystallite size of different samples.

Sample[a]	BET surface area (m^2/g)	Mesopore volume (cm^3/g)	Macropore volume (cm^3/g)	CaO crystallite size (nm)
DES	0.05	0.001	0.007	–
CES	13.45	0.007	0.021	44.3
CCA	19.04	0.030	0.001	102.1

[a] Dried eggshell, calcined eggshell and calcined commercially available $CaCO_3$ are designated as DES, CES and CCA, respectively.

Table 2
Chemical composition of calcined eggshell (wt.%).

Sample	CaO	MgO	P_2O_5	SO_3	K_2O	SrO	Cl	Fe_2O_3	CuO
Calcined eggshell	97.42	1.63	0.52	0.26	0.08	0.05	0.02	0.01	0.01

adsorption of water by CaO. The wide and strong band at around 500 cm^{-1} corresponds to the Ca–O band. The IR spectrum of the calcined commercially available $CaCO_3$ (Fig. 3c) appeared at the same wavenumber of the calcined eggshell, indicating that the calcined eggshell and the calcined commercially available $CaCO_3$ have a very similar chemical nature.

The chemical composition of the calcined eggshell (Table 2) shows that the CaO is the most abundant component (97.4%). The high amount of calcium oxide is associate the presence of the calcium carbonate, which is the main component of the waste eggshell confirmed by the XRD and FTIR results. The calcined eggshell only contained small amounts of MgO, P_2O_5, SO_3, K_2O, SrO, Fe_2O_3, CuO. Thus, the waste eggshell can be

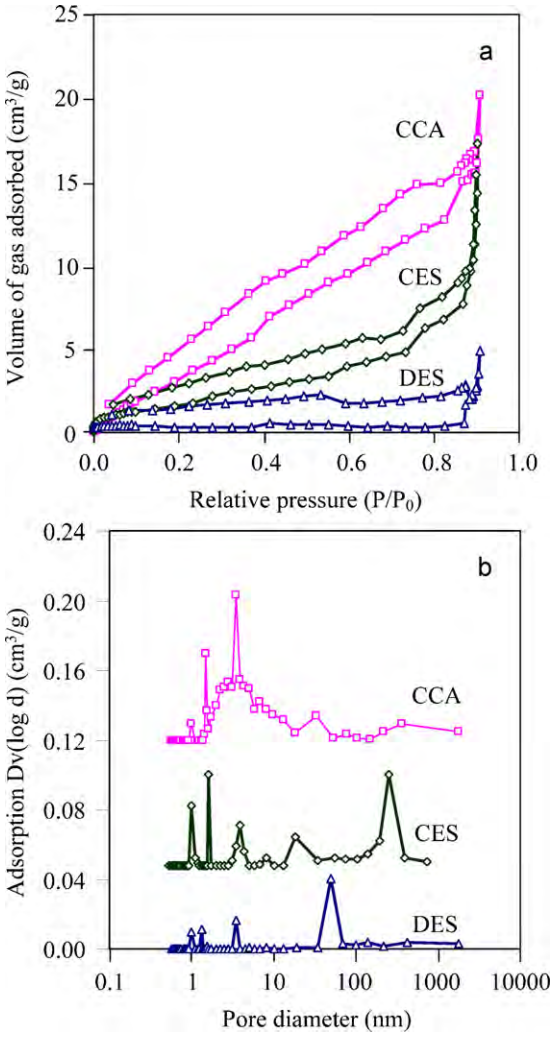

Fig. 4. N_2 sorption isotherms (a) and pore size distributions (b) of dried eggshell (DES), calcined eggshell (CES) and calcined commercially available $CaCO_3$ (CCA).

considered from a chemical viewpoint as a pure relatively natural carbonate-based material.

Due to the fact that the characteristics of the pore structure of CaO strongly influences on the diffusion and reaction of CO_2, therefore they must be thoroughly investigated and reported. The pore characteristics of all samples measured by N_2-physisorption are shown in Fig. 4. The physical properties including BET surface area, mesopore volume and macropore volume are given in Table 1. As shown in Fig. 4a, the isotherms of all samples exhibited type IV–II composite isotherms which is the characteristic of mesoporous–macroporous material. However, the amount of gas adsorbed of each sample was quite different. The isotherm of the dried eggshell was almost parallel to the *x*-axis, showing no multilayer gas adsorption. This observation indicated that the dried eggshell sample should contain only macropore without the significant contribution of mesopore volume. After calcination, the amount of gas adsorbed was increased, suggesting that numerous pores were created. Comparing between the calcined eggshell and the calcined commercially available $CaCO_3$ at relative pressure range of 0.2–0.8, the amount of gas adsorbed of the calcined eggshell was lower than that of the calcined commercially available $CaCO_3$, indicating that the calcined commercially available $CaCO_3$ had higher amount of mesopores and BET

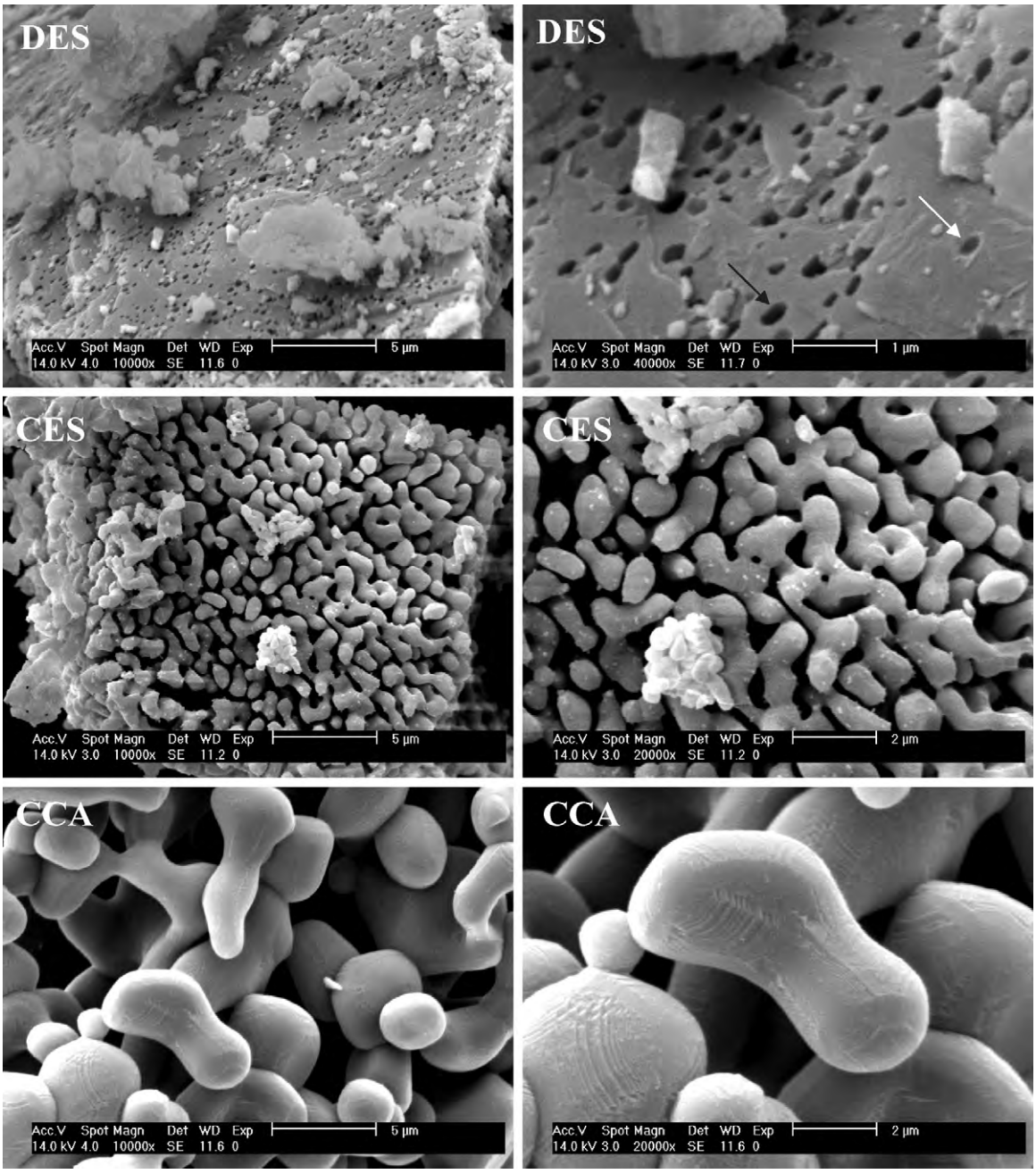

Fig. 5. SEM images of dried eggshell (DES), calcined eggshell (CES) and calcined commercially available $CaCO_3$ (CCA) at low (left) and high (right) magnifications.

surface area. However, the opposite trend was observed at relative pressure higher than 0.85, implying that the calcined eggshell had higher macropores.

The pore size distributions of all samples calculated by BJH adsorption method are shown in Fig. 4b. It was found that the pore size distribution of the dried eggshell sample is multi-modal size, with mean pore diameters of 1.0 nm, 1.3 nm and 50 nm. After calcination, some pore sizes are shifted to larger pore size and the volume of those pores are significantly increased. This is due to the fact that the removal of CO_2 during calcination process creates small pores, whereas the larger pores are obtained by the aggregates of the large grain size formed by the sintering of the smaller ones. Moreover, the small pores can possibly merge each other to form larger ones. The calcined commercially available $CaCO_3$ possess more porosity in the range of mesopore region (2–50 nm). The foregoing observations are consistent with the results in Table 1.

The apparent morphologies of the dried eggshell, the calcined eggshell and the calcined commercially available $CaCO_3$ examined by SEM are shown in Fig. 5. The dried eggshell was irregularly and very finely undulated. There were many pores and pits distributed over the entire eggshell surface. The size of the pores and the pits varied randomly from place to place. After calcination, the structure of the dried eggshell has been changed from the irregular crystal structure to inter-connected skeleton structure. The size of the skeletons was found to be approximately 1–3 μm. The voids between these skeletons were in excess of 500 nm, which eluded measurement with N_2-physisorption. It was clearly seen that the skeleton size and the voids of the calcined eggshell was smaller than those of the calcined commercially available $CaCO_3$. This was in good agreement with the CaO crystallite size obtained by the XRD results. However, it should be noted that the skeleton size observed by the SEM images was larger than the crystallite size obtained by the XRD results because the skeleton was formed by the aggregates of several nanocrystallites.

3.2. CO_2 capture performance

The carbonation conversions and carbonation rates of the calcined eggshell and the calcined commercially available $CaCO_3$ at different carbonation temperature are shown in Fig. 6. It is found that the carbonation of the two sorbents obviously occurs in two stages. The first stage rapidly occurs within 3 min due to the fast reaction of CO_2 on the outer surface of CaO particle to form the $CaCO_3$ layer covering the CaO core. The formation of $CaCO_3$ layer increases the diffusion resistance of CO_2 to react with the CaO core and thus reduces the reaction rate which is the second stage of the reaction. It can be clearly seen that the carbonation conversion of the sorbents is increased with increasing the carbonation temperature except that of CCA-750. Based on the reaction kinetics, both the reaction and solid-state diffusion rates are enhanced with the increase in the temperature. It should be noted, however, that the carbonation conversion of the CES sorbent at 750 °C is slightly higher than that at 700 °C and the difference of the carbonation conversions tends to be small with the increase of the carbonation time. Similar result is also observed for the CCA sorbent. The conversion of CCA sorbent at 750 °C is lower than that at 700 °C after 20 min of the carbonation time. This could be explained by the competition between the forward and reverse reactions (Eq. (1)), the particle size of the sorbents as well as the carbonation times.

It can be clearly seen that the carbonation conversion of the calcined eggshell is twice higher than that of the calcined commercially available $CaCO_3$ compared at the same carbonation temperature. The better carbonation performance of the calcined eggshell relative to that of the calcined commercially available $CaCO_3$ can be attributed to the smaller crystal grain size of the calcined eggshell, which provided a larger exposed surface area for the interaction between CaO and CO_2 and also produced a thinner layer of $CaCO_3$, resulting in the easier diffusion of CO_2.

In order to compare the durability performance of the calcined eggshell (CES) and the calcined commercially

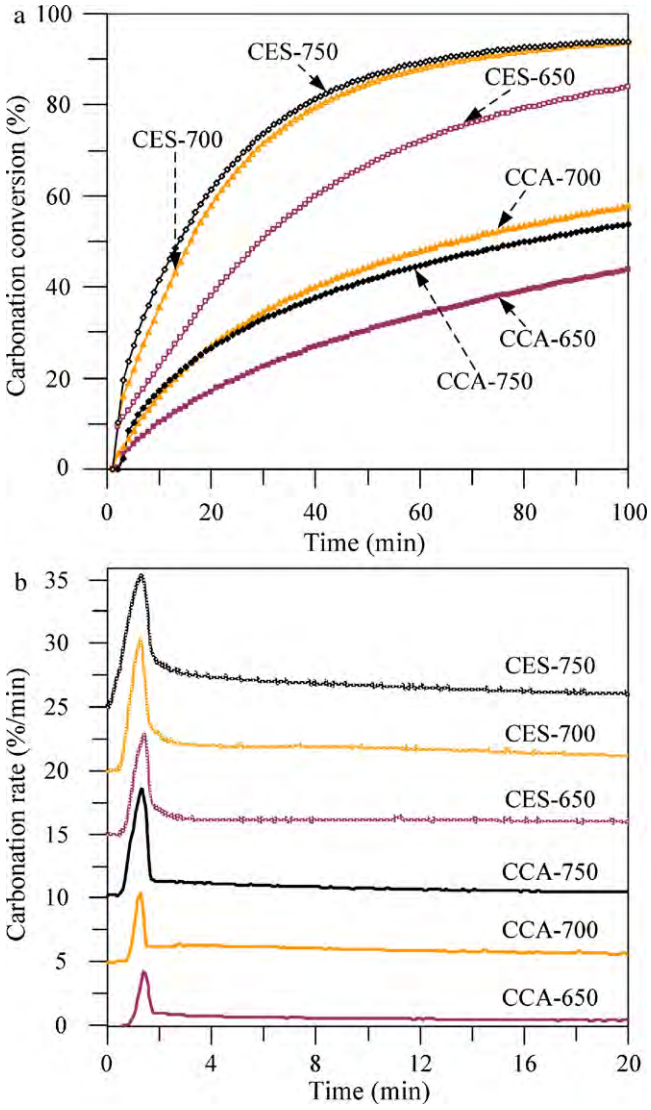

Fig. 6. Carbonation conversions (a) and carbonation rate (b) of calcined eggshell (CES) and calcined commercially available $CaCO_3$ (CCA) with different reaction temperatures after 1 cycle.

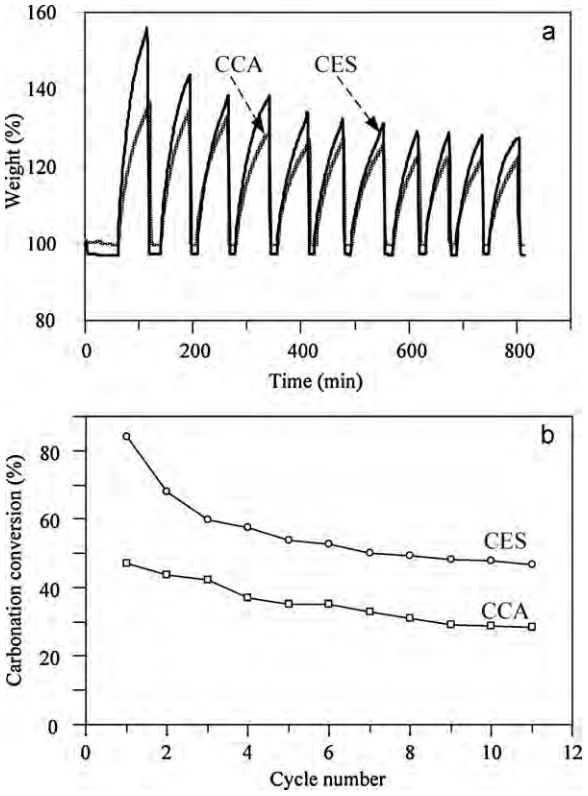

Fig. 7. Typical weight changes versus time from the TGA corresponding to carbonation–calcination through 11 cycles (a) and carbonation conversions with number of cycles (b) of calcined eggshell (CES) and calcined commercially available $CaCO_3$ (CCA).

available $CaCO_3$ (CCA), multiple carbonation cycles were performed and the results are presented in Fig. 7. Fig. 7a shows the typical data recorded in the computer in the form of weight changes over time in percentage of the CES and the CCA sorbents. It can be seen that the initial weight in percentage before the carbonation process of each sorbent is found to be different. This may be due to the presence of different amount of physically–chemically bound water. Therefore, the weight changes during carbonation–calcination steps were converted to the conversion with number of cycles based on Eq. (3) and the results are shown in Fig. 7b. It is obviously that the CO_2 capture capacity of the CES sorbent is higher than that of the CCA sorbent when compared at the same cycle. However, the CES sorbent displays a sharp decay in carbonation conversion from the first cycle to the third cycle. In contrast, the CCA sorbent showed a steady and much slower rate of decay. This observation can be explained by the fact that the smaller particle size of the CES sorbent is unstable and easier sintering during the carbonation–calcination steps which promote the formation of aggregated particles, resulting in the increase of particle size. The large particle size not only reduced an exposed surface area for the surface reaction of CO_2 but also increased the thickness of $CaCO_3$ layer for the CO_2 diffusion. Nevertheless, after 11 cycles, the carbonation conversion of the CES sorbent was 1.6 times as high as that of the CCA sorbent.

4. Conclusion

This work presents the characterization of the waste eggshell, the calcined eggshell (CES) and the calcined commercially available $CaCO_3$ (CCA) for the use as CO_2 sorbent. It is found that the CaO is the major component of the CES sorbent. The CaO crystallite size and the CaO particle size of the CES sorbent are smaller than those of the CCA sorbent. The effect of temperature on the reaction between sorbents and CO_2 was investigated. The results showed that the suitable temperature for carbonation reaction is 700 °C. The CO_2 capture capacity of the CES sorbent is higher than that of the CCA sorbent due to its smaller CaO particle size which provides a higher exposed surface for the surface reaction of CO_2. This finding indicates that the CaO derived from the waste eggshell is attractive for the use as CO_2 sorbent due to its potentially low cost, environmentally benign nature and high CO_2 capture capacity.

Acknowledgements

This work is financially supported by the Thailand Research Fund (TRF-MRG54) (for Dr. Thongthai Witoon), the Commission on Higher Education, Ministry of Education (the ''National Research University Project of Thailand (NRU)'' and the ''National Center of Excellence for Petroleum, Petrochemical and Advanced Materials (NCE-PPAM)''). Support from the Kasetsart University Research and Development Institute (KURDI) is also acknowledged.

References

[1] S. Siitonen, P. Ahtila, The influence of operational flexibility on the exploitation of CO_2 reduction potential in industrial energy production, J. Clean. Prod. 18 (2010) 867–874.
[2] J.A. Moya, N. Pardo, A. Mercier, The potential for improvements in energy efficiency and CO_2 emissions in the EU27 cement industry and the relationship with the capital budgeting decision criteria, J. Clean. Prod. 19 (2011) 1207–1215.
[3] H. Chen, K. Cheng, F. Ye, W. Weng, Preparation and characterization of graded SSC-SDC MIEC cathode for low-temperature solid oxide fuel cells, Ceram. Int. 37 (2011) 1209–1214.
[4] A.A. Olajire, CO_2 capture and separation technologies for end-of-pipe applications – a review, Energy 35 (2010) 2610–2628.
[5] T. Witoon, N. Tatan, P. Rattanavichian, M. Chareonpanich, Preparation of silica xerogel with high silanol content from sodium silicate and its application as CO_2 adsorbent, Ceram. Int. (2011), doi:10.1016/j.ceramint.2011.03.020.
[6] World Nuclear Association (WNA), 2011. Available at: http://www.world-nuclear.org/info/inf16.html (accessed 07.05.11).
[7] A.B. Rao, E.S. Rubin, A technical, economic, and environmental assessment of amine-based CO_2 capture technology for power plant greenhouse gas control, Environ. Sci. Technol. 36 (2002) 4467–4475.
[8] R. Rivera-Tinoco, C. Bouallou, Comparison of absorption rates and absorption capacity of ammonia solvents with MEA and MDEA aqueous blends for CO_2 capture, J. Clean. Prod. 18 (2010) 875–880.
[9] T. Harkin, A. Hoadley, B. Hooper, Reducing the energy penalty of CO_2 capture and compression using pinch analysis, J. Clean. Prod. 18 (2010) 857–866.
[10] Norwegian Institute of Public Heath, 2011. Available at: http://www.bios-ciencetechnology.com/News/Feeds/2011/04/industries-CO_2-capture-health-effects-of-amines-and-their-de/ (accessed 07.05.11).

[11] V. Manovic, E.D. Anthony, CaO-based pellets supported by calcium aluminate cements for high-temperature CO_2 capture, Environ. Sci. Technol. 43 (2009) 7117–7122.
[12] L. Li, D.L. King, Z. Nie, X.S. Li, C. Howard, $MgAl_2O_4$ spinel-stabilized calcium oxide adsorbents with improved durability for high-temperature CO_2 capture, Energy Fuel 24 (2010) 3698–3703.
[13] N.H. Florin, A.T. Harris, Reactivity of CaO derived from nano-sized $CaCO_3$ particles through multiple CO_2 capture-and-release cycles, Chem. Eng. Sci. 64 (2009) 187–191.
[14] C.H. Huang, K.P. Chang, C.-T. Yu, P.C. Chiang, C.F. Wang, Development of high-temperature CO_2 sorbents made of CaO-based mesoporous silica, Chem. Eng. J. 161 (2010) 129–135.
[15] V. Manovic, E.D. Anthony, Reactivation and remaking of calcium aluminate pellets for CO_2 capture, Fuel 90 (2011) 233–239.
[16] H. Chen, C. Zhao, L. Duan, C. Liang, D. Liu, X. Chen, Enhancement of reactivity in surfactant-modified sorbent for CO_2 capture in pressurized carbonation, Fuel Process. Technol. 92 (2011) 493–499.
[17] C. Luo, Y. Zheng, N. Ding, Q. Wu, G. Bian, C. Zheng, Development and performance of CaO/La_2O_3 sorbents during calcium looping cycles for CO_2 capture, Ind. Eng. Chem. Res. 49 (2010) 11778–11784.
[18] Y. Li, C. Zhao, H. Chen, L. Duan, X. Chen, Cyclic CO_2 capture behavior of $KMnO_4$-doped CaO-based sorbent, Fuel 89 (2010) 642–649.
[19] L. Li, D.L. King, Z. Nie, X.S. Li, C. Howard, $MgAl_2O_4$ spinel-stabilized calcium oxide adsorbents with improved durability for high-temperature CO_2 capture, Energy Fuel 24 (2009) 3698–3703.
[20] S.F. Wu, Y.Q. Zhu, Behavior of $CaTiO_3$/nano-CaO as a CO_2 reactive adsorbent, Ind. Eng. Chem. Res. 49 (2010) 2701–2706.
[21] A. Silaban, M. Narcida, D.P. Harrison, Characteristics of the reversible reaction between CO_2(g) and calcined dolomite, Chem. Eng. Commun. 146 (1996) 149–162.
[22] J.J. Klemeš, P.S. Varbanov, S. Pierucci, D. Huisingh, Minimising emissions and energy wastage by improved industrial processes and integration of renewable energy, J. Clean. Prod. 18 (2010) 843–847.
[23] M.V. Iyer, L.-S. Fan, High temperature CO_2 capture using engineered eggshells: a route to carbon management, Patent No. US 76,787,351 B2 (2010)
[24] A. Doostmohammadi, A. Monshi, M.H. Fathi, Z. Golniya, A.U. Daniels, Bioactive glass nanoparticles with negative zeta potential, Ceram. Int. (2011), doi:10.1016/j.ceramint.2011.03.026.
[25] G Gergely, F. Wéber, I. Lukács, A.L. Tóth, Z.E. Horváth, J. Mihály, C. Balázsi, Preparation and characterization of hydroxyapatite from eggshell, Ceram. Int. 36 (2010) 803–806.

Thongthai Witoon, D. Eng. is a lecturer at the Department of Chemical Engineering Kasetsart University, Thailand. He received the Scholarship from the Royal Golden Jubilee (RGJ) Program under the Thailand Research Fund (TRF) for doctoral degree study in Kasetsart University. His research focuses are mainly on the nanomaterials synthesis using renewable resources, the CO_2 capture at low and high temperature and the fine chemical production from CO_2 hydrogenation reaction. His works have been appeared in international journals including *Materials Letters*, *Journal of Sol–Gel Science Technology*, *Colloids and Surfaces A: Physicochemical and Engineering Aspects*, *Fuel Processing Technology and Ceramics International*.

Journal of Non-Crystalline Solids 357 (2011) 3513–3519

Contents lists available at ScienceDirect

Journal of Non-Crystalline Solids

journal homepage: www.elsevier.com/ locate/ jnoncrysol

Effect of pH and chitosan concentration on precipitation and morphology of hierarchical porous silica

Thongthai Witoon [a,b,*], Soponwit Tepsarn [a], Puscharapon Kittipokin [a], Ben Embley [a], Metta Chareonpanich [a,b]

[a] National Center of Excellence for Petroleum, Petrochemicals and Advance Material, Department of Chemical Engineering, Faculty of Engineering, Kasetsart University, Bangkok 10900, Thailand

[b] Center for Advanced Studies in Nanotechnology and Its Applications in Chemical Food and Agricultural Industries, Kasetsart University, Bangkok 10900, Thailand

ARTICLE INFO

Article history:
Received 24 March 2011
Received in revised form 20 June 2011
Available online 15 July 2011

Keyword:
Organic–inorganic hybrids;
Chitosan;
Sol–gel process;
Sodium silicate;
Precipitation

ABSTRACT

Understanding the interaction between chitosan molecules and sodium silicate is one of the principal objectives for the development of new environmentally benign strategies for the synthesis of low-cost porous silica with hierarchical structure. In this work, we have explored two essential factors simultaneously: chitosan/silica ratios (0.1, 0.4, 0.8 and 1.6) and pH values of the mixture (3, 5 and 6). The obtained silica–chitosan composite and the calcined products were investigated by using thermal gravimetric analysis, N_2-physisorption, scanning electron microscopy, and transmission electron microscopy. Rapid precipitation of silica–chitosan composite occurred because of the initial pH values of the chitosan and sodium silicate solutions. The amount of precipitating silica–chitosan composite was increased with increasing pH value of the mixture and chitosan/silica ratios but it did not change with the decrease of pH value of the mixture. The as-synthesized products prepared at pH 3 and 6 showed macroscopic two-solid phases (consisting of silica-rich phase and chitosan-rich phase), while those prepared at pH 5 displayed liquid and solid phases. At pH 3, a unimodal porous structure was found for the calcined products obtained from the silica-rich phase while a hierarchical structure was found for those obtained from the chitosan-rich phase; meanwhile, a hierarchical structure occurred for all calcined products prepared at pH 6. Different hierarchical structures of the silica products could be obtained by changing pH value of the mixture and chitosan/silica ratios.

1. Introduction

Silica materials have attracted much attention for many researchers because they can be used commercially as, for example, a catalyst support [1], a controlled drug release [2], and a sorbent [3]. Several Researchers have focused on the improvement of surface chemistry, molecular structure, morphology and porosities of silica materials in order to obtain the best performance for each application [3–5]. Traditional syntheses of silica-based materials require elevated temperature, high pressure, strongly acidic or alkaline media, and a long time for the synthesis process [6]. By comparison, biologically controlled silica materials production not only occurs under benign conditions but also produces silica materials with hierarchically ordered pore structures ranging from the nanometer to micrometer domain [7,8]. Such materials can provide a high specific surface area and more interaction sites via nanopores, while the presence of additional macropores can enhance mass transport and easier accessibility to the active sites. These features make such materials highly desirable and promising for applications in catalysis and separation technology [1,9]. The discovery and refinement of biologically controlled silica materials have inspired many researchers to obtain better control over the structure and morphology of chemically produced silica.

Recently, several kinds of biopolymer containing amine functionalities have been investigated for their roles in the hydrolysis–condensation process and structure of silica products [7,10,11]. It was found that individual amino acids could reduce or catalyze the early kinetics of condensation and precipitation of silica materials. It seems reasonable that current issues for biologically controlled silica materials production should not be limited to understanding their roles in the formation of silica products, but should also extend to the use of the biomaterials that are cheaper and readily available in nature.

In addition to amino acids, chitosan biopolymer, which is produced from partial *N*-deacetylation of chitin, is an interesting material to be used in the synthesis of silica materials, due to its low-cost, biodegradability, and non-toxic characteristic. Silica formation in the presence of chitosan was first reported by Pedroni et al. [12].

* Corresponding author at: National Center of Excellence for Petroleum, Petrochemicals and Advance Material, Department of Chemical Engineering, Faculty of Engineering, Kasetsart University, Bangkok 10900, Thailand. Tel.: +66 2579 2083; fax: +66 2561 4621.
E-mail address: fengttwi@ku.ac.th (T. Witoon).

0022-3093/$ – see front matter © 2011 Elsevier B.V. All rights reserved.
doi:10.1016/j.jnoncrysol.2011.06.029

They found that a fibrous material was formed by a spongelike siliceous network with pores having a radius of 0.57 μm. Ayers et al. [13] prepared chitosan/silica hybrid gels to improve the uniformity and dimensional stability of aerogels. Chang et al. [14] investigated the effect of chitosan on different stages of the silica polymerization. They found that the addition of chitosan not only increased the rate of turbidity change, but also increased the rate of size enlargement of silica nanoparticles. Wang et al. [15] reported that chitosan biopolymer could induce the fast gelation of glycol-modified tetraethoxysilane by changing the sol–gel transition mechanism from reaction-limited kinetics to diffusion-limited kinetics. The effect of pH values on the formation of silica/chitosan composites was studied by our group [16]. We found that the growth of silica domain was limited by the chitosan network when the pH of mixture was higher than 3. However, only one value of chitosan/silica ratio was employed.

Here to more fully assess the role of chitosan molecules on the precipitated silica–chitosan composite and the morphology of silica materials, we have looked at two key structural features: (*i*) chitosan/silica ratios and (*ii*) pH values of the mixture. Both factors were investigated simultaneously. Images of visual inspection of the silica–chitosan precipitates at different conditions and stages of silicate condensation were obtained. The physical properties and morphological structure of the final silica products were examined by N_2-sorption, Scanning Electron Microscopy (SEM) and Transmission Electron Microscopy (TEM). These results provided the essential information for further development of a simple, low-cost route to synthesize porous silica products with novel structures and tailored properties.

2. Experimental

2.1. Chemicals and reagents

All chemicals and reagents are of analytical grade and used without any further purification. Chitosan with 80% deacetylation was purchased from Eland Corporation. Sodium silicate ($Na_2Si_3O_7$: 27 wt.% SiO_2, 4 wt.% NaOH) was obtained from Thai Silicate Company. Acetic acid and sodium hydroxide were purchased from Sigma-Aldrich Company.

2.2. Preparation of porous silica

In a typical synthesis process, ×grams (0.1, 0.4, 0.8 and 1.6 g) of chitosan were dissolved overnight in 60 ml of 2% v/v acetic acid in deionized water at room temperature. Then, 3.7 g based on 1 g of sodium silicate solution was primarily diluted with 10 ml of deionized water and slowly added to the chitosan solution with vigorous stirring. The error in weighing is approximately ±0.0001 g. It should be noted that, measured with a pH meter (model CG-842, Schott), the initial pH values of chitosan solution and sodium silicate were 3.6 and 11.1, respectively, and the pH value after mixing was approximately 5. The error in pH measurement is approximately ±0.01. Afterwards, the pH value of the mixture was quickly adjusted to 3 or 6 by the addition of 2 M HCl or 2 M NaOH solution, respectively. The mixture was stirred at 40 °C for 24 h and after that it was poured into a glass bottle and aged in a Teflon-lined autoclave at 100 °C for 24 h. The synthesis conditions are listed in Table 1. In some cases, the products had separated into two phases: one at the top and one at the bottom of the bottle. The whole products at the top and at the bottom were carefully taken out by using a dropper. The product near the interface was left since its composition could be a mixture of phases. The obtained products were filtrated, washed several times with distilled water, dried at 120 °C for 24 h, and calcined at 600 °C for 4 h at a heating rate of 2 °C/min. The physical properties of the calcined products are shown in Table 2.

Table 1
Synthesis conditions of silica products.

Sample ID[a]	pH values of mixture	Chitosan (g)
P3-0.1	3 ± 0.01	0.1 ± 0.0001
P3-0.4	3 ± 0.01	0.4 ± 0.0001
P3-0.8	3 ± 0.01	0.8 ± 0.0001
P3-1.6	3 ± 0.01	1.6 ± 0.0001
P5-0.1	5 ± 0.01	0.1 ± 0.0001
P5-0.4	5 ± 0.01	0.4 ± 0.0001
P5-0.8	5 ± 0.01	0.8 ± 0.0001
P5-1.6	5 ± 0.01	1.6 ± 0.0001
P6-0.1	6 ± 0.01	0.1 ± 0.0001
P6-0.4	6 ± 0.01	0.4 ± 0.0001
P6-0.8	6 ± 0.01	0.8 ± 0.0001
P6-1.6	6 ± 0.01	1.6 ± 0.0001

[a] Distilled water of 70 mL and sodium silicate of 3.7 ± 0.0001 g based on 1 ± 0.0001 g of silica were used throughout this study. The silica products are designated as PX-Y where X is the pH value and Y is the mass ratio of chitosan to silica.

2.3. Characterization of porous silica products

2.3.1. Measurement of the amount of chitosan

The amount of chitosan incorporated into the as-synthesized products was investigated by using a simultaneous DTA-TGA analyzer (TA instrument, SDT2960 Simultaneous DTA-TGA Universal 2000) in air at a heating rate of 10 °C/min.

2.3.2. Measurement of N_2 sorption isotherms

Nitrogen sorption isotherms of bimodal porous silica products were measured at−196 °C using a Quantachrome Autosorb-1 C instrument. Prior to sorption measurements, the products were degassed at 200 °C for 12 h. The specific surface area and pore size distribution were calculated using the Brunauer–Emmett–Teller (BET) and the Barrett–Joyner–Halenda (BJH) methods, respectively. The total pore volumes were measured at a relative pressure P/P_0 of 0.995. Three measurements were taken with each sample. The statistical uncertainty has been stated with the data and is reported in the Table 2.

2.3.3. Measurement of surface morphology and nanostructure

Surface morphology of the porous silica products was analyzed by using field Emission Scanning Electron Microscopy (FE-SEM: JEOL JSM-6301 F, Au-coated, operated at 20 keV). The nanostructure of the products was analyzed by using Transmission Electron Microscopy

Table 2
Physical properties of the products synthesized under various conditions.

Sample ID[a]	BET surface area (m^2/g)	Total pore volume (cm^3/g)
P3-0.1	750 ± 2	0.51 ± 0.01
P3-0.4-T	763 ± 3	0.63 ± 0.02
P3-0.4-B	784 ± 2	1.11 ± 0.03
P3-0.8-T	742 ± 4	0.64 ± 0.02
P3-0.8-B	775 ± 7	1.20 ± 0.03
P3-1.6-T	760 ± 6	0.70 ± 0.02
P3-1.6-B	784 ± 8	1.31 ± 0.04
P5-0.1	420 ± 3	1.01 ± 0.02
P5-0.4	417 ± 5	1.23 ± 0.03
P5-0.8	430 ± 5	1.31 ± 0.03
P5-1.6	428 ± 6	1.90 ± 0.05
P6-0.1	369 ± 3	1.51 ± 0.02
P6-0.4	349 ± 4	1.82 ± 0.05
P6-0.8-T	322 ± 2	1.21 ± 0.03
P6-0.8-B	381 ± 3	1.66 ± 0.05
P6-1.6-T	320 ± 4	1.24 ± 0.02
P6-1.6-B	390 ± 6	1.93 ± 0.05

[a] T and B are designated as the silica products in the top and the bottom parts of the bottle, respectively.

(TEM: JEOL JEM-2010 microscope with an acceleration voltage of 200 kV). In order to prepare the sample for TEM analysis, the porous silica products were suspended in ethanol and dried at room temperature on a copper grid coated with a carbon film.

3. Results

Visual inspection of the silica–chitosan precipitates gives valuable information. Fig. 1 presents silica–chitosan precipitates at different stages: after pH adjustment, silicate condensation at 40 °C for 24 h, and silicate condensation at 100 °C for 24 h. For a relatively low chitosan content (Fig. 1a), precipitation was not observed for the samples prepared at pH 3 and pH 5, while the silica–chitosan instantly precipitated after the pH value was adjusted to 6. When heated to 40 °C with stirring for 24 h, the solutions prepared at pH 5 and 6 were transformed to white opaque homogenous solutions. After aging at 100 °C for 24 h, a translucent bulk gel was obtained from the solution prepared at pH 3, with no visible silica–chitosan precipitate.

When the sodium silicate was added at a chitosan/silica ratio of 0.4 (Fig. 1b), the silica–chitosan composite was precipitated immediately. The amount of silica–chitosan precipitate did not change after the pH of the mixture was adjusted to 3, while the increasing amount of the silica–chitosan precipitates at pH 6 was obtained. After aging at 40 °C for 24 h, the sample prepared at pH 3 had separated into two phases: one at the top and one at the bottom of the bottle. As the chitosan/silica ratio was increased yet further (Fig. 1c and d), a phase separation of the product prepared at pH 6 was also observed. The amount of chitosan molecules in the silica–chitosan precipitates at different phases was investigated by using thermal gravimetric analysis (TGA) technique.

TGA patterns of representative samples obtained from two different phases (P3-1.6-B, P3-1.6-T, P6-1.6-B, and P6-1.6-T) are shown in Fig. 2. All samples show four well-distinguished steps. The first and second steps occur in the temperature range 50–200 °C, corresponding to mass loss of 8–10 wt.%, are associated with the loss of physical and chemical adsorption of water molecules. The third step occurs in the temperature range 200–330 °C and corresponds to the degradation of the backbone chain of the chitosan molecules. The fourth step takes place at the temperature range 330–620 °C and is associated with the decomposition of the functional groups of the chitosan molecules. It is clearly seen that the amount of chitosan molecules incorporated into the silica–chitosan composites obtained from the bottom part of the bottle (chitosan-rich phase) is higher than that obtained from the top part of the bottle (silica-rich phase).

The aggregated characteristics and morphologies of the porous silica products were investigated by SEM and TEM, and representative images are shown in Figs. 3 and 4, respectively. Synergistic effects between chitosan/silica ratio and pH value of the mixture on the aggregated and morphological characteristics of the porous silica products are observed, meaning that the effects of these parameters should be discussed simultaneously.

At pH 3, the structure of silica products synthesized with a relatively small amount of chitosan was a continuous gel and appeared as a dense aggregation of silica nanoparticles (Figs. 3a and 4a). In the bottom part of the bottle (chitosan/silica = 0.4, Figs. 3b and 4b), spherical silica particles were obtained with a grain size of about

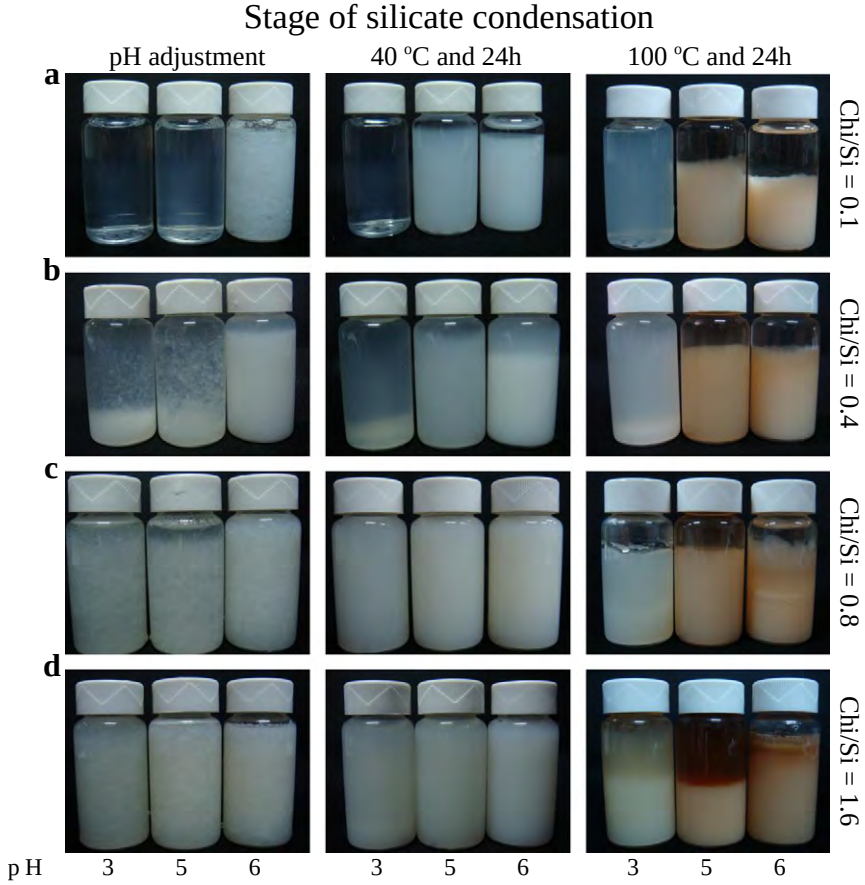

Fig. 1. Visual observations of the effect of pH and chitosan concentration on silica–chitosan precipitation at different stages. Chi/Si is the mass ratio of chitosan to silica in the preparation step.

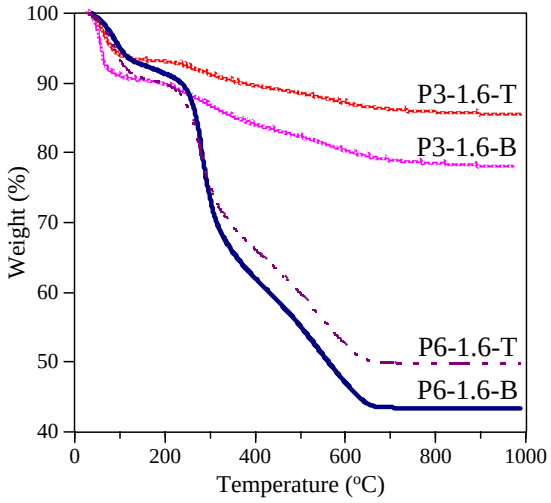

Fig. 2. TGA patterns of as-synthesized silica–chitosan composite prepared at pH 3 and 6 obtained at the top and the bottom of the bottle, designated as PX-Y-T or B, where X is the pH value used, Y is the mass ratio of chitosan to silica in the preparation step, T is the product at the top and B is the product at the bottom.

100–150 nm. The grains were more uniform when a larger amount of chitosan/silica ratio was applied (Fig. 3c). With a yet higher chitosan/silica ratio, grains with a spherical shape were no longer obtained and instead a rod-like structure was formed (Figs. 3d and 4c). In the top part of the bottle, the morphology of silica products prepared at chitosan/silica ratio of 0.4–0.8 (not shown here) was similar to that of silica products prepared with a relatively small amount of chitosan (Figs. 3a and 4a).

At pH 5, the structure of silica products synthesized with a relatively small amount of chitosan showed a dense aggregation of silica nanoparticles (Fig. 3e), similar to that of silica products prepared at pH 3 (Fig. 3a). A skeleton structure was formed and its size was decreased when the chitosan/silica ratio was increased (Figs. 3f to h and 4d to f).

At pH 6, the aggregation of irregular spherical shapes of silica particles was obtained even for a relatively small amount of chitosan (Fig. 3i). A self-agglomerate of interconnected porous silica with uniform grain size was observed at a chitosan/silica ratio of 0.4 (Figs. 3j and 4g). For higher chitosan/silica ratios (0.8, 1.6) at this pH value, the aggregation of spherical shapes of silica particles was again obtained (Figs. 3k to l and 4h to i), but the observed grain size was

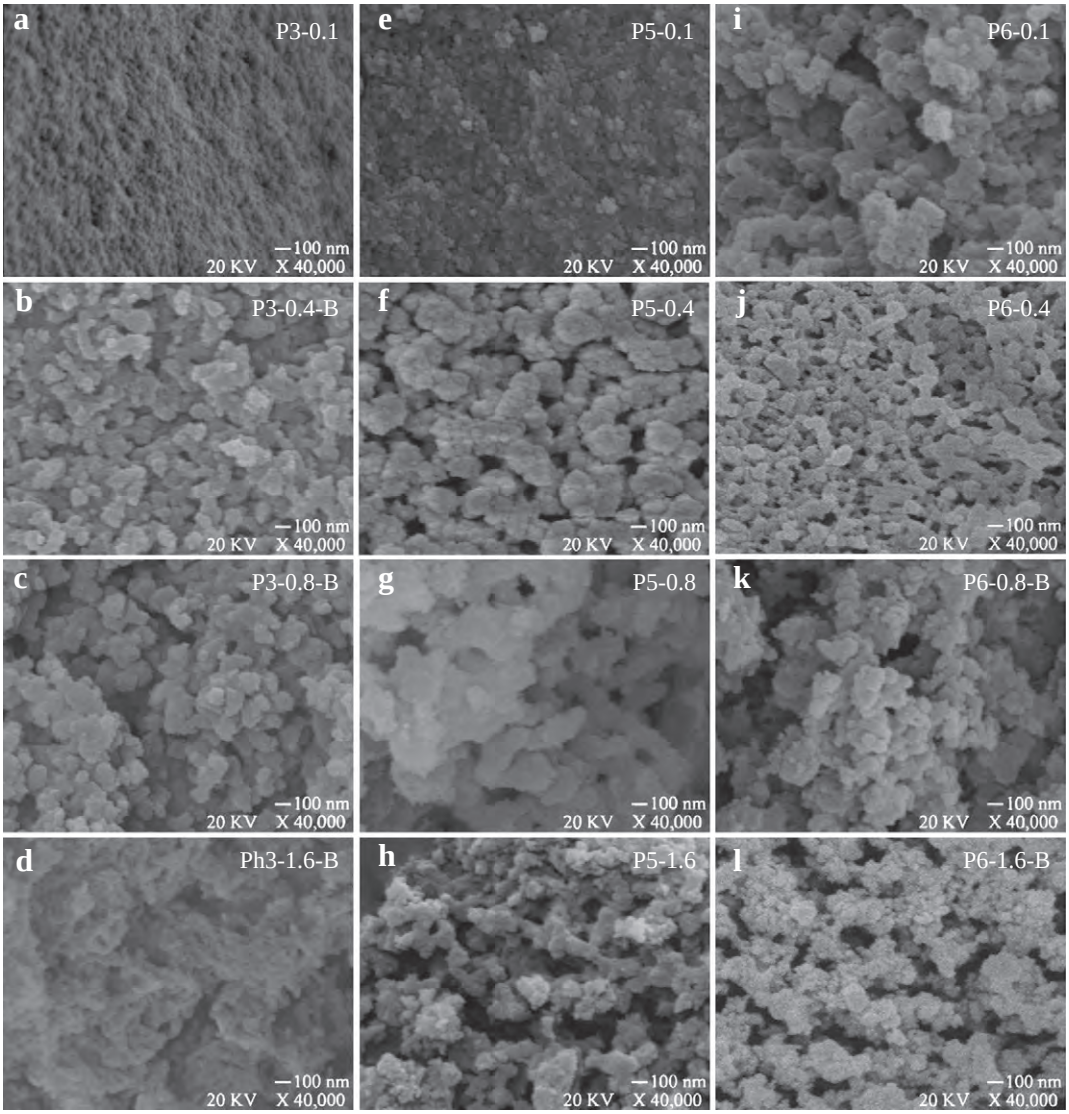

Fig. 3. SEM images of silica products prepared at different pH values and chitosan/silica ratios, designated as PX-Y-T or B, where X is the pH value used, Y is the mass ratio of chitosan to silica in the preparation step, T is the product at the top and B is the product at the bottom.

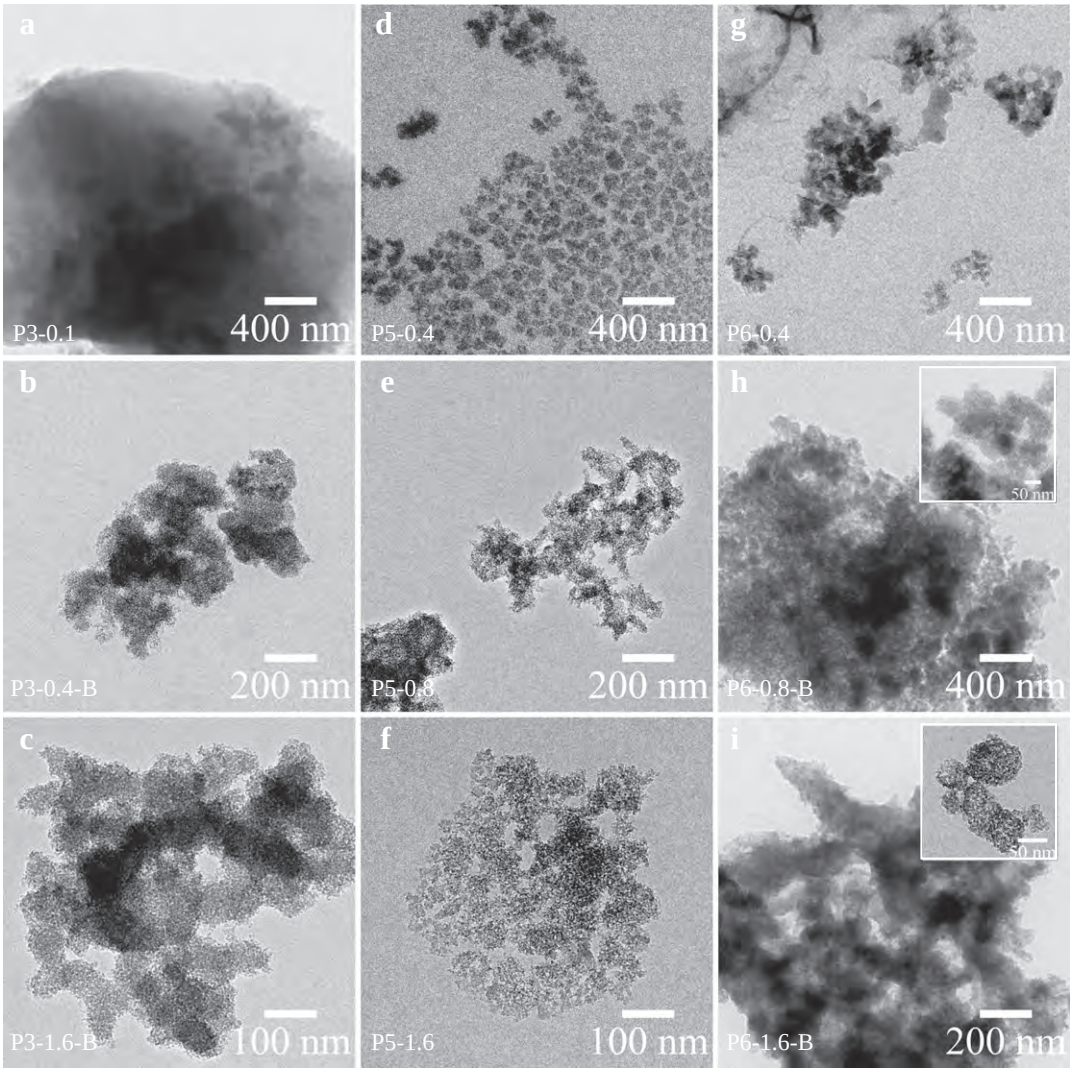

Fig. 4. TEM images of silica products prepared at different pH values and chitosan/silica ratios, designated as PX-Y-T or B, where X is the pH value used, Y is the mass ratio of chitosan to silica in the preparation step, T is the product at the top and B is the product at the bottom.

smaller than that of the silica product prepared with a relatively small amount of chitosan (Fig. 3i).

Adsorption/desorption isotherms for the silica product prepared at pH 3 and with a relatively small amount of chitosan (Fig. 5a) exhibited a type IV isotherm with H2 hysteresis loop, indicating that the product is composed of mesopores with an ink-bottle structure. At higher chitosan/silica ratios, the type II-IV composite isotherms, which are characteristic of meso-macroporous materials were obtained for silica products obtained from the bottom part of the bottle (Fig. 5b to d; opened symbols). For all samples obtained from the top part of the bottle (Fig. 5b to d; closed symbols), the isotherms could mainly be described as type IV; however, the gas sorption at high relative pressure ($P/P_0 > 0.85$) was found to gradually increase with an increasing chitosan/silica ratio, indicating the existence of large mesopores in the structure. At pH 5, the isotherm gradually transitioned from a type IV isotherm to a type II-IV composite isotherm (Fig. 5e to h) with increasing chitosan/silica ratio. All silica products synthesized at pH 6 showed the II–IV composite isotherms (Fig. 5i to l).

Fig. 6 shows the pore size distribution of porous silica products synthesized at various conditions. At pH 3, the pore size distribution of silica products prepared with a relatively small amount of chitosan was located in the mesopore diameter region, with mean pore diameter of about 3.8 nm (Fig. 6a). For higher chitosan/silica ratios, the silica products obtained from the bottom part of the bottle exhibited a pore size distribution at two different length scales—both mesopore and macropore diameters (Fig. 6b to d; opened symbols)—whereas the silica products obtained from the top part of the bottle (Fig. 6b to d; closed rectangular) showed a similar result to the silica products synthesized with a relatively small amount of chitosan (Fig. 6a). However, a broader pore size distribution (Fig. 6d) was obtained when the chitosan/silica ratio was increased sufficiently high (chitosan/silica = 1.6). At pH 5, the pore size distribution in the macropore range was broadened with increasing chitosan/silica ratio (Fig. 6e to h). At pH 6, a broad pore size distribution—in the range of both mesopores and macropores—was obtained in every case (Fig. 6i to l). The BET surface area and the total pore volume of all samples are given in Table 2.

4. Discussion

The silica–chitosan precipitate which is observed in this work can be explained by attractive electrostatic interactions between the positively charged amino groups of chitosan molecules and the negatively charged silicate species. At pH 3, the amino groups of chitosan molecules are highly protonated, while the charge of the

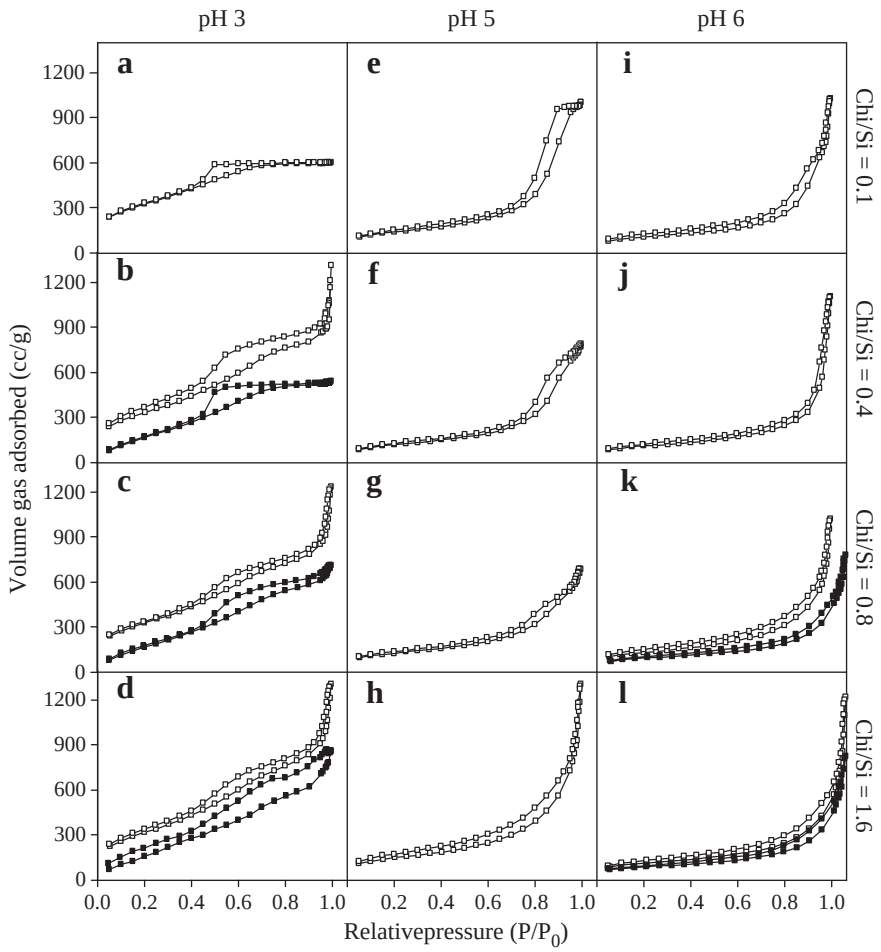

Fig. 5. N_2 sorption isotherms of silica products prepared at pH 3, 5, and 6 with chitosan/silica of 0.1, 0.4, 0.8, and 1.6.

silicate surface is very close to zero, resulting in minimal interaction between chitosan molecules and silicate species. Thus, silica–chitosan precipitates should not exist. However, in general, the initial pH values of sodium silicate and chitosan solution are about 11 and 3.6, respectively. After mixing, the pH of chitosan was increased whereas the pH of sodium silicate was decreased. The pH of the mixture is about 5. This condition leads to precipitation of silica and chitosan molecules at an early stage for systems with a chitosan/silica ratio greater than 0.1. It can be seen that the silica–chitosan precipitation is irreversible, because the amount of precipitate does not change after the final preparation step (silicate condensation at 100 °C for 24 h). The formation of silica products at the top part is due to the hydrolysis and condensation of sodium silicate itself, without any significant effect of the chitosan molecules and therefore the growth of the silica domain is not limited, as shown by the results of SEM and TEM images in Figs. 3a and 4a, respectively. For the silica products in the bottom part, the silica domain was limited by the chitosan network, resulting in a smaller silica domain size.

At pH 5, positively charged amino groups still exist on the backbone chains of the chitosan molecules, and the charge of the silicate species is more negative than at pH 3. This may result in interaction between chitosan molecules and silicate species through an ionic crosslinking interaction. In contrast, in a system adjusted at pH 3, the charge density and the free ammonium groups of the chitosan molecules are lower, resulting in a decrease in the size of the void of the chitosan networks. Accordingly, the chitosan molecules can play a significant role in controlling the size of the silica domain at pH 5.

At pH 6, the size of the void of the chitosan networks is even more decreased. As a result, the chitosan molecules can control the silica domain even if there is only a small amount of the chitosan present (chitosan/silica = 0.1). The silica domain is decreased as the chitosan/silica ratio is increased to 0.4; this is caused by the distribution of silica species in a highly dense chitosan network, which limits the growth of the silica domain. By increasing the chitosan/silica ratio yet further (chitosan/silica > 0.8), a phase separation occurs in the precipitated material and results in a silica-rich phase and a chitosan-rich phase (as confirmed by the TGA results). Such a phase separation is possible because the chitosan networks are more dense and compact, and thus the silicate species hardly penetrate within the voids of the chitosan network.

5. Conclusion

The purpose of this work is to delineate the effect of chitosan/silica ratios and pH values on silica–chitosan precipitates and on the morphology of silica products. The principal findings are summarized as follows: (1) The silica–chitosan precipitates depend on the initial pH values of the chitosan and the sodium silicate solutions. (2) Macroscopic two-solid phases (a silica-rich phase and a chitosan-rich phase) occur in the products prepared at pH 3 and pH 6. (3) At pH 3 and pH 5, the size of the silica domain was decreased with increasing chitosan/silica ratios. (4) At pH 6, the size of silica domain was decreased when increasing the chitosan/silica ratios from 0.1 to 0.4. At higher chitosan/silica ratios, the size of silica domain did not change significantly with further addition of chitosan. (5) The change of

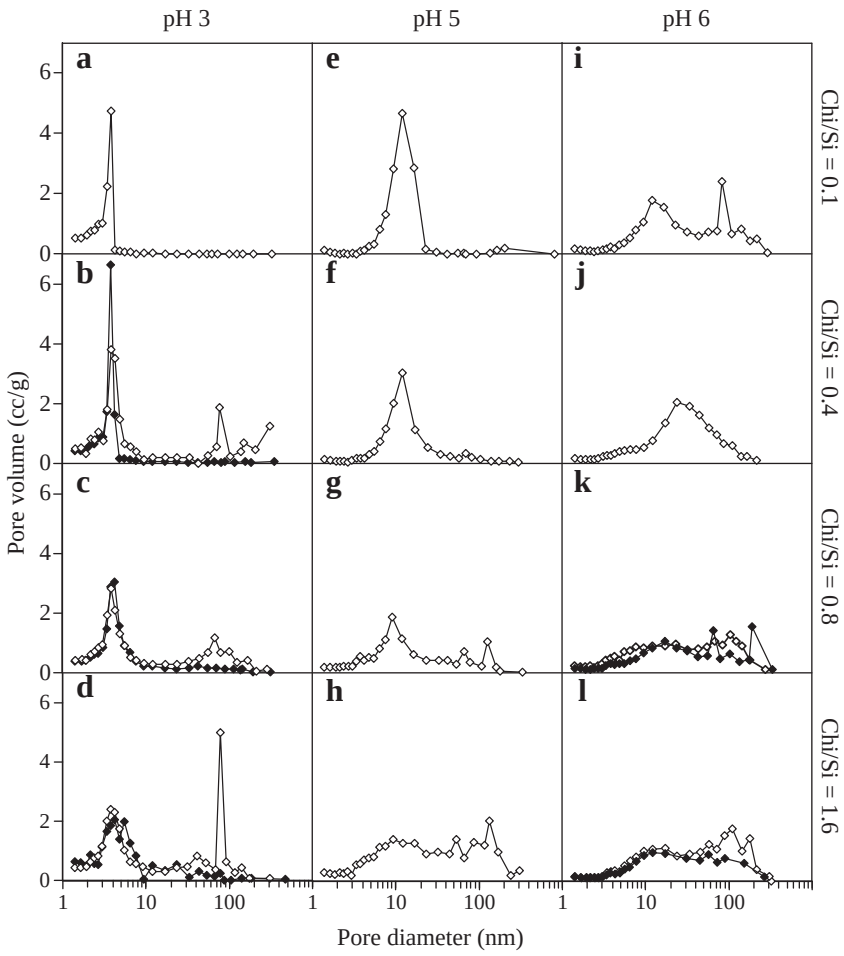

Fig. 6. Pore size distribution of silica products prepared at pH 3, 5, and 6 with chitosan/silica of 0.1, 0.4, 0.8, and 1.6.

morphological structure of the calcined products might be due to the change of conformation structure of the chitosan during the synthesis conditions that act as the template for the formation of hierarchical porous silica with different morphologies.

Acknowledgements

This work was financially supported by the Research Grant for New Scholar (Grant No. MRG5480196) co-funded by the Thailand Research Fund (TRF); the Commission on Higher Education, Thailand; and Kasetsart University, Thailand. The authors would like to thank the National Center of Excellence for Petroleum, Petrochemical and Advanced Materials (NCE-PPAM). Support from the "National Research University Project of Thailand (NRU) is also acknowledged.

References

[1] T. Witoon, M. Chareonpanich, J. Limtrakul, Fuel Process. Technol. 92 (2011) 1498–1505.
[2] J. Pang, Y. Luan, F. Li, X. Cai, Z. Li, Mater. Lett. 64 (2010) 2509–2512.
[3] T. Witoon, N. Tatan, P. Rattanavichian, M. Chareonpanich, Ceram. Int. 37 (2011) 2297–2303.
[4] T. Mehling, I. Smirnova, U. Guenther, R.H.H. Neubert, J. Non-Cryst. Solids 355 (2009) 2472–2479.
[5] Q. Chen, F. Fan, D. Long, X. Liu, X. Liang, W. Qiao, L. Ling, Ind. Eng. Chem. Res. 49 (2010) 11408–11414.
[6] C.J. Brinker, G.W. Scherer, Sol–gel Science: The Physics and Chemistry of Sol–gel Processing, Academic Press, New York, 1990.
[7] A. Bernecker, R. Wieneke, R. Riedel, M. Seibt, A. Geyer, C. Steinem, J. Am. Chem. Soc. 132 (2010) 1023–1031.
[8] C.Y. Khripin, D. Pristinski, D.R. Dunphy, C.J. Brinker, B. Kaehr, ACS Nano 5 (2011) 1401–1409.
[9] G.A. Seisenbaeva, M.P. Moloney, R. Tekoriute, A. Hardy-Dessources, J.-M. Nedelec, Y.K. Gun'ko, V.G. Kessler, Langmuir 26 (2010) 9809–9817.
[10] D.J. Belton, S.V. Patwardhan, V.V. Annenkov, E.N. Danilovtseva, C.C. Perry, Proc. Natl. Acad. Sci. U. S. A. 105 (2008) 5963–5968.
[11] E. Brunner, K. Lutz, M. Sumper, Phys. Chem. Chem. Phys. 6 (2004) 854–857.
[12] V. Pedroni, P.C. Schulz, M.E. Gschaider de Ferreira, M.A. Morini, Colloid Polym. Sci. 278 (2000) 964–971.
[13] M.R. Ayers, A.J. Hunt, J. Non-Cryst. Solids 285 (2001) 123–127.
[14] J.-S. Chang, Z.-L. Kong, D.-F. Hwang, K.L.B. Chang, Chem. Mater. 18 (2006) 702–707.
[15] G.-H. Wang, L.-M. Zhang, J. Phys. Chem. B 113 (2009) 2688–2694.
[16] T. Witoon, M. Chareonpanich, J. Limtrakul, J. Sol-Gel Sci. Technol. 51 (2009) 146–152.